University of Illinois at Urbana-Champaign

ACRC

Air Conditioning and Refrigeration Center   A National Science Foundation/University Cooperative Research Center

Experimental Analysis of a Minimum-TEWI Air Conditioner Prototype

S. L. Stott, C. W. Bullard and W. E. Dunn

ACRC CR-21   August 1999

Abstract

A 2.5 ton, minimum-TEWI split system air conditioner prototype was tested over an extensive range of operating conditions to validate the system simulation model that had been used to design the prototype. The experimental results were compared with system and component-only simulations to quantify performance. The overall measured system capacity was 13% less than the model predicted at dry coil conditions and 18% less for wet coil conditions. Analysis of individual component identified flow maldistribution in both the microchannel condenser and evaporator coils. The model simulations combined with experimental data provided guidelines for improving flow distribution and component performance. Finally, the experimental results from the prototype confirmed initial design recommendations for a minimum-TEWI residential air conditioner. Additional constraints on the design recommendations were developed to ensure optimal performance for all components in the system.

Table of contents

List of Figures

List of Tables

Nomenclature

A	area	ft^2
C_H	loss coefficient for 4-way valve	-
C_p	specific heat	Btu/lbm-R
D	diameter	ft, in
f	friction factor	-
F	ratio of frictional losses in superheated to two-phase region of the evaporator	-
G1	ratio of inlet header length to header diameter	-
G2	ratio of header diameter to inlet pipe diameter	-
h	enthalpy	Btu/lbm
L	length	ft
$\dot{P}$	power	W
p, P	absolute pressure	psia
?p, dP	heat exchanger or venturi pressure drop	psid
Re	Reynolds number	$\dfrac{4w}{\pi\mu D}$
$\dot{Q}$	capacity	Btu/hr
t or T	temperature	°F
V	velocity	ft/s
$\dot{V}$	air-side volumetric flow rate	cfm
$\dot{w}$	refrigerant mass flow rate	lbm/hr
$\dot{W}$	work	Btu/hr
x	refrigerant quality	-

Greek Symbols

ρ	density	lbm/ft^3
η	efficiency	-

Subscripts and Modifiers

air	air-side
avg, av	average
amb	ambient

C, cond	condenser	
disc	discharge-line venturi	
e	equivalent	
E, evap	evaporator	
eff	effective	
fan	fan	
h, ht	hydraulic	
header	condenser or evaporator header	
in	inlet	
inlet	inlet header	
lm	losses, minor	
lo	liquid only	
Moody	Moody friction factor	
outlet	outlet header	
r, ref	refrigerant-side	
sub	subcooling	
suct	suction line	
sup	superheat	
2ph	two-phase	
tubes	tubes of heat exchanger	
walls	walls on indoor test chamber	

Constants

g	gravitational constant	32.2 lbm-ft/(lbf-s^2)
π	pi	3.14159 rad

Chapter 1: Introduction

1.1 Background and motivation

Due to an increasing demand for more efficient and environmentally friendly air conditioning systems, this project focused on designing a minimum TEWI (Total Equivalent Warming Impact) residential air-conditioning system. TEWI is an index that measures the global warming impact of the unit during its lifetime due to both direct (refrigerant leakage) and indirect (CO_2 emissions) contributions. To minimize TEWI, new technologies that allowed for efficient use of alternative refrigerants were combined with charge minimization techniques.

This project was divided into two stages. The first stage began with the modification of the Room Air Conditioning Model (Mullen *et al.* 1998) to incorporate the geometry, pressure drop and heat transfer correlations relevant to microchannel split-systems. The resulting program was used to re-design a prototype R-22 microchannel split-system, minimizing TEWI, constrained by the types of tubes and fins available to make the prototype evaporator and condenser. This system was built, instrumented and installed in the ACRC testing facility and the first stage of this project was completed (Kirkwood and Bullard 1999). The second and final stage is the focus of this report.

1.2 Purpose

The primary purpose of this report is to present and interpret the large body of experimental data taken from the TEWI split-system. In the process, the accuracy of the model will be investigated. Bridges and Bullard (1995) and Jensen and Dunn (1996) validated the original version of the model but the success of the new air-side heat transfer correlation (Chang and Wang 1997) and the applicability of the two-phase pressure drop correlation to microchannel tubes (de Souza 1995) remains to be evaluated. Once validated, the model and experimental results could both be used as tools to define what a true minimum TEWI system would look like.

1.3 Scope of this report

Chapter 2 of this report uses experimental data to evaluate the accuracy of the model at the system and component level. Some unexpected results prevented many conclusions from being drawn concerning the model. Different hypotheses are presented, and tested in the following chapters.

Chapter 3 explores the cause and effects of maldistribution in the condenser coil. After it is verified that maldistribution is occurring, suggestions for future microchannel condenser designs are provided.

Chapter 4 describes in detail the maldistribution in the evaporator coil.

Chapter 5 provides the final design recommendations for a minimum TEWI split-system air-conditioner.

Chapter 6 is the final summary of the experimental results and conclusions.

Appendix A details the method used to calculate the condenser and evaporator capacity from the experimental data.

Appendix B validates the blower calibration and compressor map. While the compressor map had excellent agreement with the experimental data, the blower calibration proved to be unreliable for wet-coil test points. Therefore air flow rates were calculated from the air-side energy balance.

Appendix C compares the model's prediction with the experimentally measured water removal rate.

Appendix D describes the power measurement system used in the experimental facility along with its calibration procedure.

Appendix E provides a summary of the maldistribution data for the evaporator.

Finally, Appendix F is a summary of the more important experimental data and the model's predictions.

Chapter 2: System Performance Analysis

2.1 Introduction

The microchannel split-system described by Kirkwood and Bullard (1999) was extensively instrumented and tested in the ACRC calorimetry rooms. Experimental data was taken over a wide range of test conditions and fan speeds. The results were compared with simulation runs to quantify overall system performance and validate the accuracy of the model on a component-by-component basis. Large discrepancies between the model's predictions and the experimental results limited the conclusions that could drawn at the system level. More detailed investigations of the evaporator and condenser were therefore undertaken, and are presented in Chapters 3 and 4.

2.2 Experimental results

2.2.1 Test matrix

The test matrix was defined to test the limits of the model and to provide a data set rich in information about performance of each component. It included a broad range of mass flow rates, pressures and room conditions while varying both evaporator and condenser fan speeds. The final matrices are presented in Figures 2.1a and b. In total, 90 steady-state test points were taken over a period of one month. Four points were repeated after the matrix was completed to test for repeatability. A complete listing of the experimental results can be found in Appendix F. The data set presented by Kirkwood and Bullard (1999) cannot be compared to the data presented here due to differences in refrigerant charge totals and evaporator blower speeds.
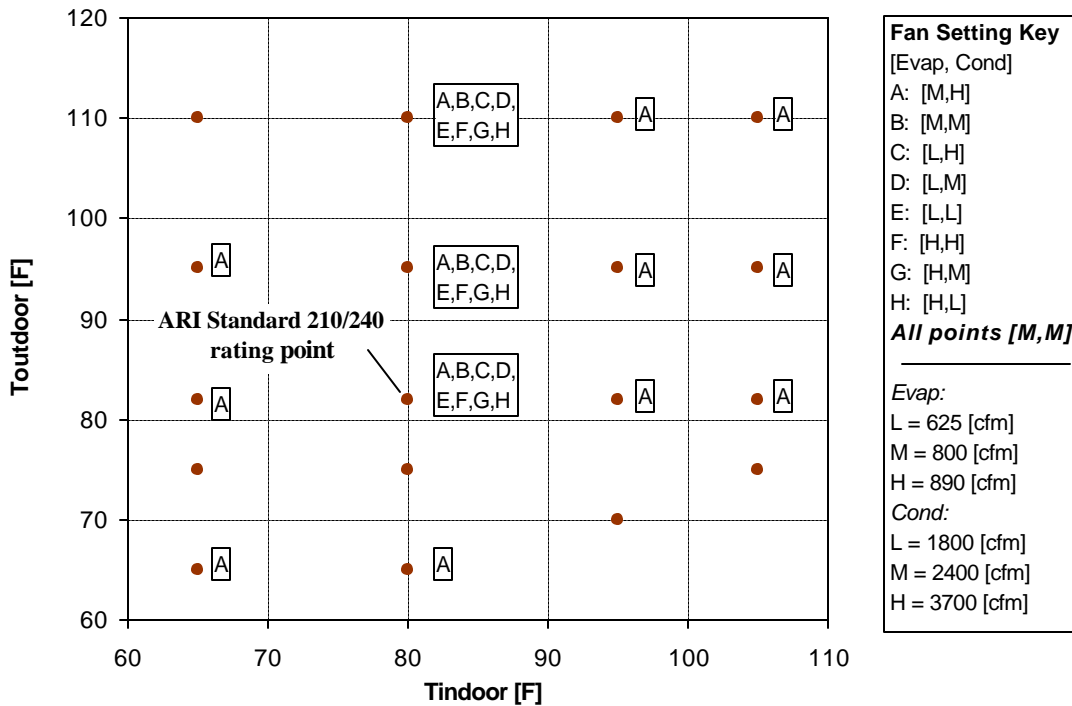
Figure 2.1a Steady-state dry evaporator coil test matrix
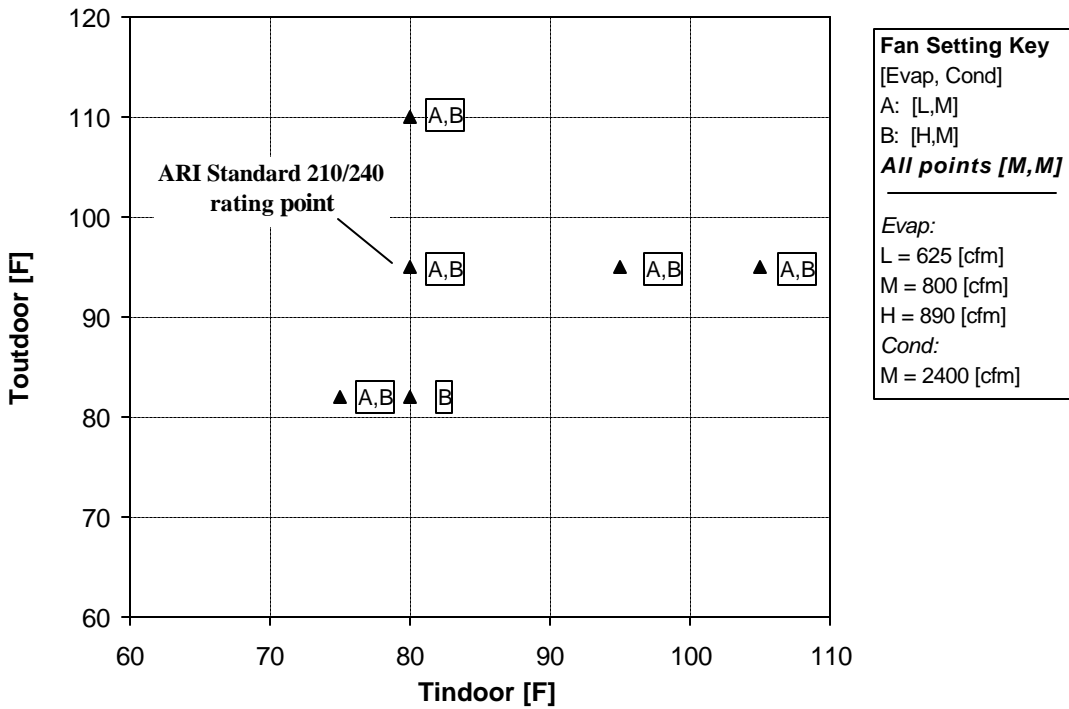
Figure 2.1b Steady-state wet evaporator coil (RH 51.5%) test matrix

2.2.2 Total system performance

        Predicted capacity was calculated by running the microchannel system simulation model for given indoor and outdoor room conditions, fan speeds and total charge. The measured system capacity, Q_{room}, was determined from the room power measurement using the method described in Appendix A. Figure 2.2 shows system capacity performance for all 90 points in the test matrix.

        The model overpredicted system capacity for the dry coil points with a mean error of 13%. The accuracy of the model decreased for the wet coil points, the average error being 18%. The standard deviation on the error for the dry and wet points was 3%.
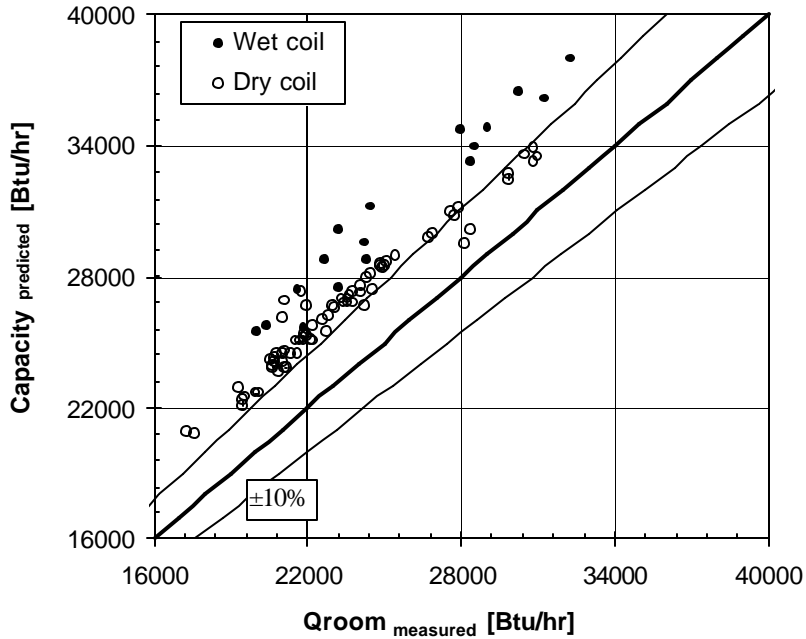
Figure 2.2 Accuracy of system capacity prediction

The most important model output is the prediction of EER (Energy Efficiency Ratio). When running the model in design mode, EER is the variable that is typically optimized to determine the most efficient system design. The accuracy of the model's prediction of EER is presented in Figure 2.3. The mean error for dry coil prediction was 15%, with a standard deviation of 5%. The wet coil mean error is 18% with a standard deviation of 4%.
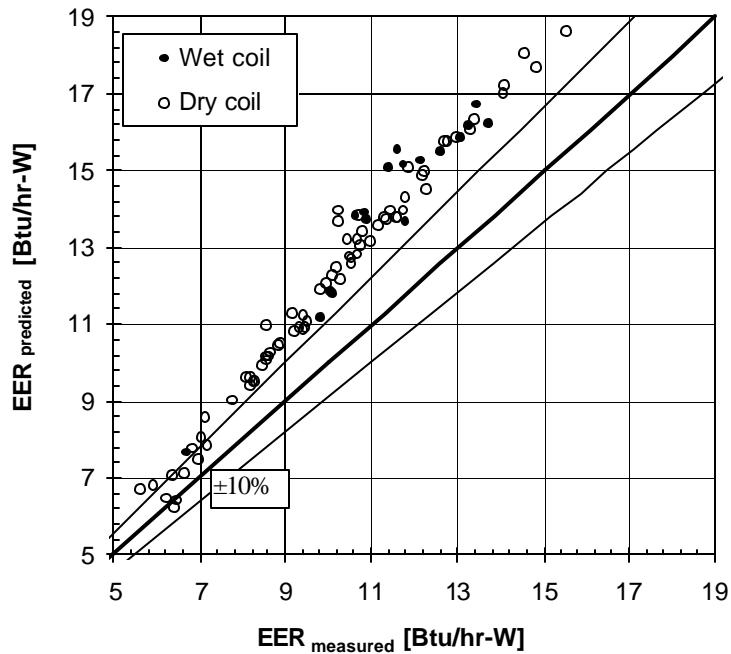
Figure 2.3 Accuracy of EER prediction

5

Two factors could possibly explain the inconsistencies between the model and the experimental data. First, there may be errors in the correlations used in the model for pressure drop and heat transfer. Second, one or more of the components in the system is not operating to design specifications. The latter option was investigated by analyzing the components individually, as described in the following sections and chapters.

2.2.3 Condenser performance

The condenser was the first component analyzed with the intention of validating the Chang and Wang (1997) air-side heat transfer correlation for folded louvered fins. The accuracy of the model's prediction capabilities was judged using two different parameters, condenser capacity and ΔTsubcooling. The model was run in component mode, isolating the condenser submodel from the system. The condenser exit states and other outputs were calculated, given the measured inlet pressures and temperatures and mass flow rates. Figure 2.4 shows that the measured capacity for the condenser fell within 5% of the prediction for all data points, with a mean error of 2.8%. The standard deviation for the error was 1.5%.
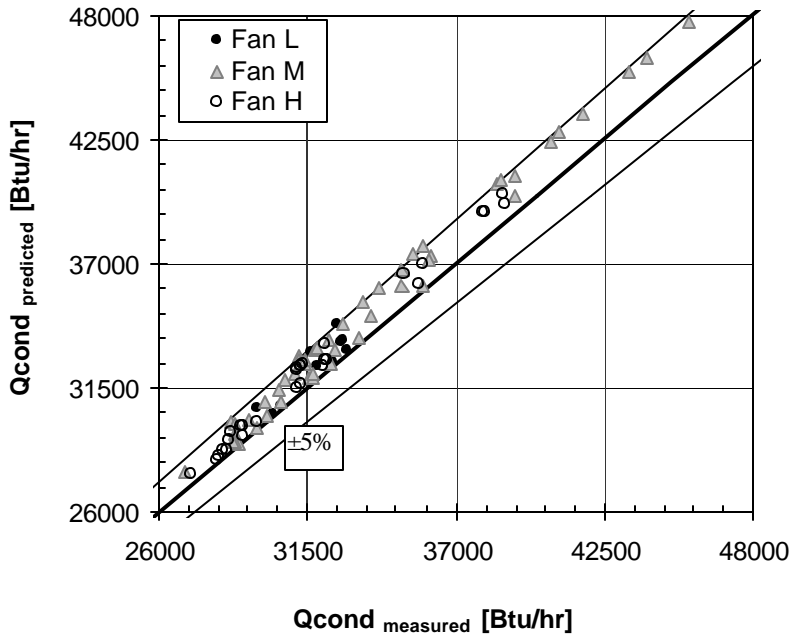
Figure 2.4 Accuracy of condenser capacity prediction

The accuracy of the capacity prediction can be misleading because its magnitude is dominated by the latent enthalpy of vaporization. Subcooling or outlet temperatures are much more difficult variables to predict. By specifying inlet pressure, the simulated condensing temperature is set approximately equal to measured, so the model is essentially being asked to calculate the areas required for desuperheating, condensing and subcooling. Figure 2.5 shows that the model can be have a ΔT$_{error}$ (***DT***$_{predicted}$ - ***DT***$_{measured}$) as large as 29ºF. The average ΔT$_{error}$ was 9ºF.

To investigate if an error in Chang and Wang's air-side heat transfer correlation could result in such poor prediction of ΔTsubcooling, a penalty factor for the correlation was incorporated into the model. To adjust the subcooling predictions so that all lie within ±5ºF of the measured values, the correlation must be multiplied by 0.4 or less. It is unlikely that the error in the correlation could be so large, but it is difficult to quantify what the true error

6

could be. For the moment, it will be assumed that Chang and Wang's (1997) air-side heat transfer correlation is reasonably accurate, while other possible sources of error are investigated. Chapter 3 provides a detailed analysis of refrigerant flow maldistribution in the condenser.
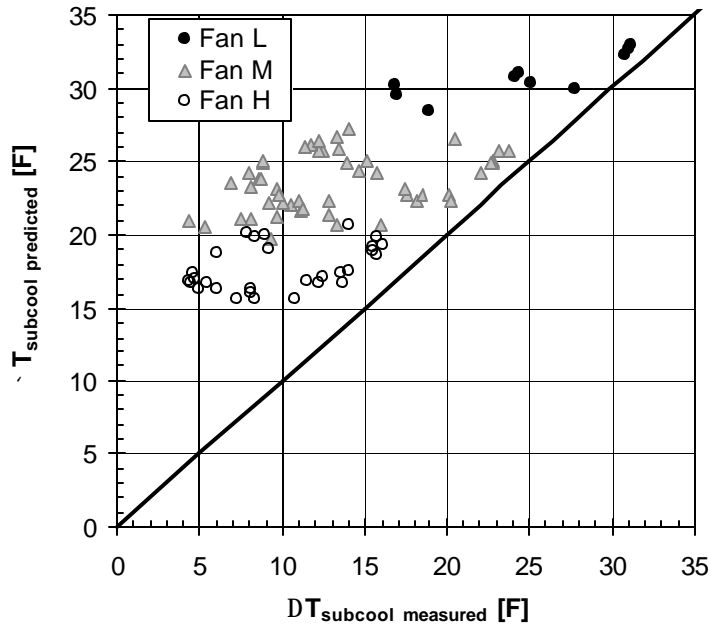
Figure 2.5 Accuracy of ΔTsubcool prediction

2.2.4 Evaporator performance

As in the case of the condenser, the evaporator was also simulated in component-only mode. The measured data for refrigerant mass flow rate, inlet enthalpy and inlet temperature were input to the model that in turn predicted the capacity, evaporating temperature and exit superheat. The results in Figure 2.6 show that for all fan speeds, the dry evaporator capacity was overpredicted about 12% by the evaporator submodel, with a standard deviation of 2%. Figure 2.7 shows that the error increases to 21% for wet coil conditions, with a standard deviation of 12.7%. Details on the measurement of evaporator capacity can be found in Appendix A. Further analysis of flow maldistribution in the evaporator coil can be found in Chapter 4 and the accuracy of the water removal rate prediction is calculated in Appendix C.
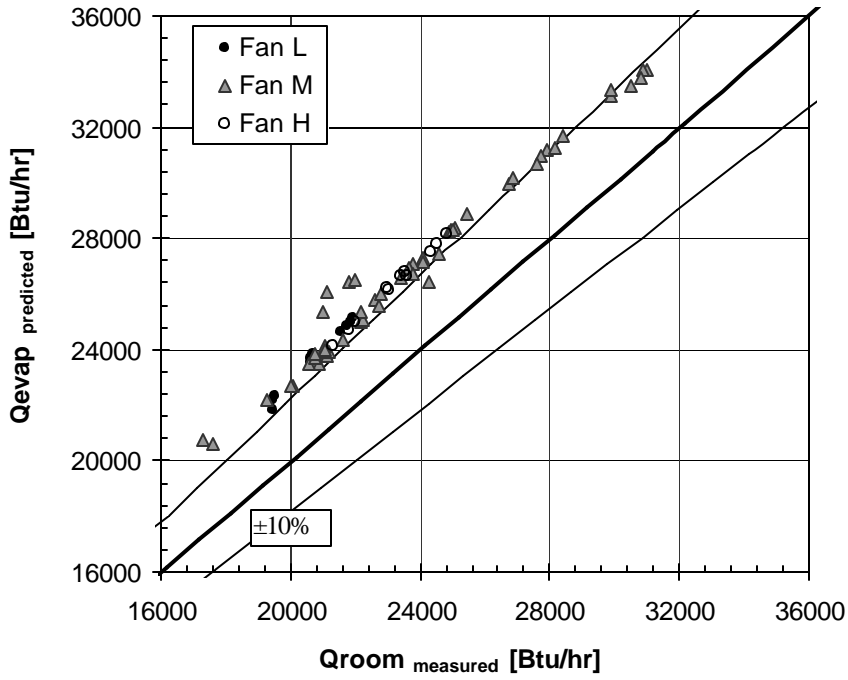
Figure 2.6 Evaporator dry coil capacity performance
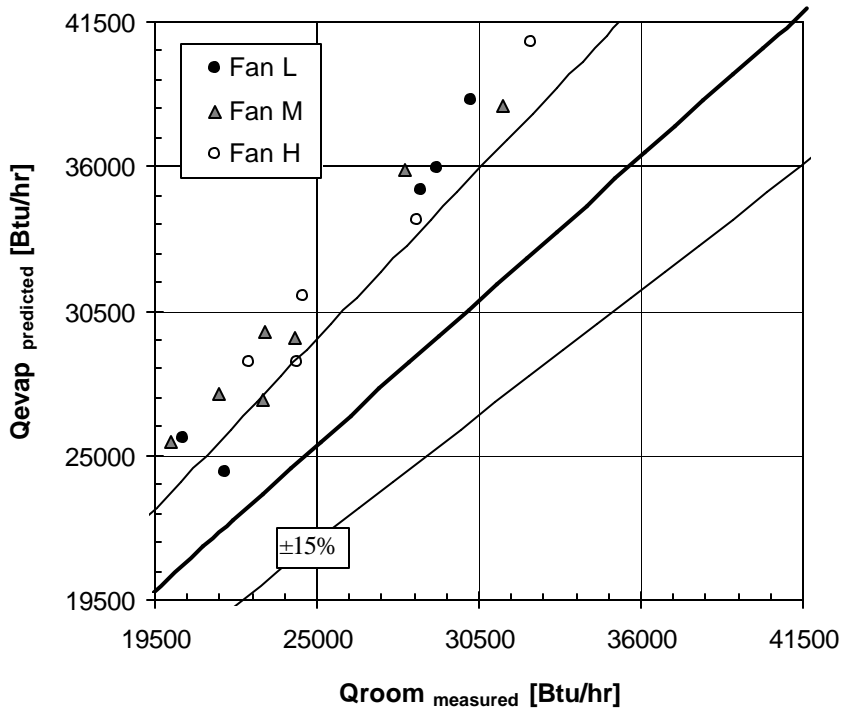
Figure 2.7 Evaporator wet coil capacity performance

2.2.5 Compressor

The compressor map supplied by Copeland Corporation for its ZP23K3E scroll compressor was found to be in excellent agreement with the data (Muir, 1996). Comparisons presented in Appendix B, found that the compressor performed on average within 5% of the map's predictions for mass flow rate and power consumption.

2.2.6 Blower

The Bryant Model 40FK4C003 blower used for the evaporator coil was equipped with a controller that can adjust the torque of the fan to compensate for static pressure drops in ductwork, providing a constant volumetric flow rate for one setting. Modine Mfg. Co. tested the blower in our housing and their calibration is compared with the experimental results in Appendix B. The performance of the blower was excellent for low humidity indoor room conditions, but it appeared to falter at high humidity/wet evaporator coil points. However, this error was compensated for and is not enough to explain the capacity loss, as will be shown in Appendix B.

2.2.7 Refrigerant charge

The total charge was initially estimated by running the system simulation model in design mode, setting ΔTsubcooling to 10ºF for an 80/82/wet point. When charging the system, an additional 0.8 lbm of charge was required to match the model's simulation with the measured subcooling. The extra 12% of refrigerant charge could be interpreted as another signal that something is occurring in one of the components that is inhibiting the capacity. Kirkwood and Bullard (1999) presented a detailed analysis of the charge distribution in the system. The largest amount of charge (45%) was estimated to be in the condenser coil. Further analysis will be conducted with the condenser data in the following chapter in an attempt to explain the discrepancy between measured and calculated charge.

Chapter 3: Condenser Maldistribution

3.1 Introduction

After experimental data fell short of predictions, questions arose concerning the performance of the condenser. Questions remained regarding the model's 12% underestimation of the amount of refrigerant charge needed to match measured with predicted subcooling. Combined with the unexpected large pressure drops measured across the condenser coil, it was evident that something was occurring in the condenser. Maldistribution problems are expected in evaporators where two-phase flow is being distributed through multiple parallel circuits, but seems less likely in condenser because the single-phase vapor is being distributed among the inlets to all circuits. Instrumentation was added to the condenser that provided surprising information about the flow distribution across the condenser coil. This information will be used to provide recommendations for future microchannel condenser designs.

3.2 Charge inventory

Section 2.2.6 discussed the extra 0.8 lbm of refrigerant charge added to the system to match the model's predicted subcooling. To gain some insight as to where the extra charge could be located, the model was used to calculate the amount of refrigerant required for each component at the 80/82/wet test condition. Kirkwood and Bullard (1999) provided a detailed summary for all the components, lines and miscellaneous instrumentation in the system. An overall view of the largest contributors to the total refrigerant charge can be seen in Figure 3.1.

Component	Charge [lbm]
Condenser	2.35
Evaporator	0.38
Liquid line	1.18
Ref. in oil	0.54
Filter dryer	0.8
Other	0.69
Total	**5.94**
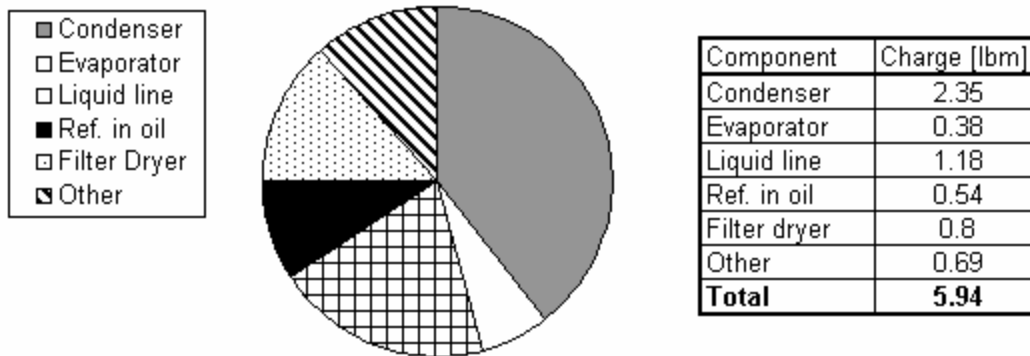
Figure 3.1 Predicted refrigerant charge distribution for 80/82/wet test point

The charge calculation for the liquid line and the filter dryer will have very little error since the geometry is well known and the two components are completely filled with subcooled refrigerant. 'Other' includes the remaining components that individually, are insignificant to the total contribution. The compressor and all of the instrumentation is included in this category and the charge calculation is assumed to be accurate. It seemed unlikely that errors in the void fraction correlations used in the model could account for such inaccurate predictions. However, even if the evaporator charge prediction varied by 10%, the total amount of charge only increases by .04 lbm. Likewise, if the amount of refrigerant in oil was off by 10%, the charge increases by 0.05 lbm. This still leaves 0.71 lbm of charge unaccounted for. Since the condenser is the largest contributor to charge and the measured

subcooling deviated from the model's predictions, it was hypothesized that the extra charge is most likely in the condenser. Further analysis of the experimental data was done to investigate the validity of the hypothesis.

3.3 Experimental setup

The condenser coil pictured in Figure 3.2 consists of 79 microchannel tubes bent in a downward facing 'V' shape at an angle of 45°. Each microchannel tube has 19 trapezoidal ports and a length of 6.28 ft. The inlet and outlet headers are cylindrical and 2.55ft long. The discharge line enters the inlet header dead center. The outlet header has eight tubes that feed into a distributor in reverse-flow configuration that allows for the coil to be used as a heat pump.
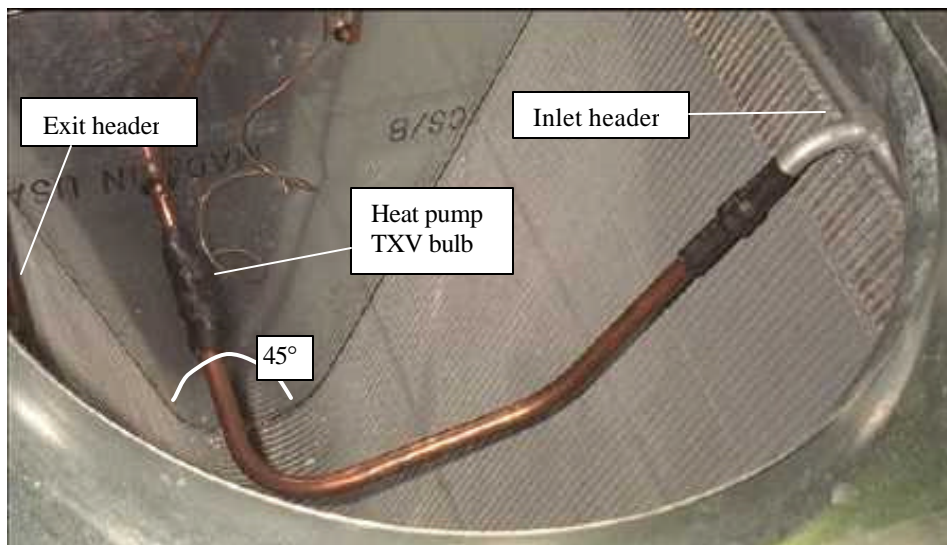
Figure 3.2 Condenser coil: top view

An absolute pressure transducer and an immersion thermocouple were placed in the liquid line four feet downstream from the condenser exit. A differential pressure transducer recorded the pressure drop between the exit of the compressor and the exit of the condenser. The pressure drop reading included the pressure drop through the 4-way heat pump valve located upstream of the inlet header, and the reverse flow through the distributor and TXV located downstream of the exit header. The pressure drop through these devices was accounted for and documented in Appendix A, so the pressure drop through the coil could be determined. According to information provided by the manufactures, pressure drop through the 4-way valve was almost negligible, while that across the distributor and TXV could exceed frictional pressure drop in the tubes by more than a factor of 15. An immersion thermocouple was also placed in the discharge line 12 inches from the compressor exit.

After data acquisition began, 40 surface thermocouples were attached to the center of the condenser tubes 1½" from the exit header. The louvered fins were not removed from the condenser exit, so there is the possibility of heat transfer from the fins to the thermocouple. The tubes were covered with a 4" wide double layer of armaflex insulation tape followed by aluminum tape in an attempt to obtain readings within 1°F of the true refrigerant temperature. The thermocouples can be viewed in Figure 3.3. Two additional surface thermocouples were attached to a center tube at the bottom of the 'V'. These thermocouples were also covered with multiple layers of insulation.

In most cases they indicated the saturation temperature of the condenser, which was usually 3ºF higher than that corresponding to the pressure in the liquid line downstream of the TXV.
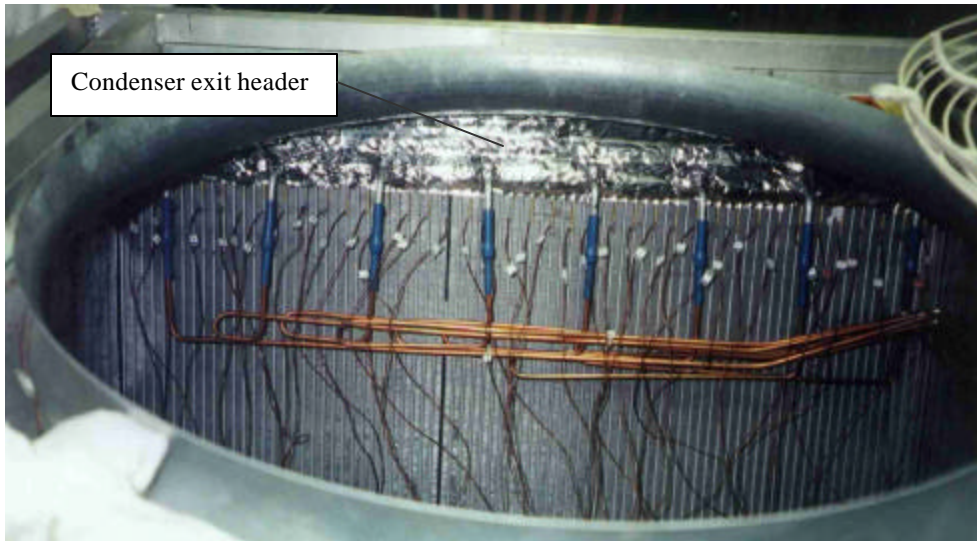
Figure 3.3 Surface thermocouples along condenser exit before insulation

3.4 Maldistribution investigation

The exploration of flow maldistribution had to be based mainly on temperature data because there was no pressure transducer installed across the headers alone. Therefore, the pressure drop across the condenser had to be determined indirectly by subtracting from the measured value, estimates of the (~0.5 psi) pressure drop across the 4-way valve upstream of the condenser and the (~5 psi) pressure drop across the distributor and TXV located downstream of the condenser but upstream of the liquid line pressure tap.

3.4.1 Theory

Experimental measurements showed a much larger pressure drop across the condenser coil than predicted in the model. The model simulations for the condenser did not account for the dynamic pressure drop inside the header or the gravitational effects on the refrigerant. Concerns arose that these values could be much larger than expected and resulted in maldistribution in the coil. Recent work by Lalot *et al.* (1999) found that if the dynamic pressure losses inside the header are large in comparison to the pressure drop across the tubes, severe maldistribution can occur in condensers, resulting in an estimated capacity loss of 7%.

Lalot *et al.* state that flow maldistribution in condensers can occur for two different reasons; reverse flow in the tubes and/or large dynamic pressure variations in the inlet header. Lalot *et al.* define two dimensionless parameters: G1 is the ratio of inlet header length to diameter (46 for prototype) and G2 is the ratio of header diameter to the condenser inlet pipe diameter (1.1 for prototype). Reverse flow will occur if the inlet pipe is small in comparison to the header diameter (G2 > 1) and the header is nearly 'square'. In this situation, strong vortices will develop inside the header, pulling fluid up the condenser tubes located far from the centrally-located inlet tube pipe. On the other hand, if the header length is much greater than the header diameter, (G1 > 5, as in our case) dynamic pressure

variations along the header could still result in maldistribution. If these variations are significant, only the tubes near the inlet of the header will see the flow exiting the discharge line.

Lalot *et al.* defined a variable, η, as the ratio of the maximum/minimum velocity in the tubes (Eq. 3.1). When pressure drop across the heat exchanger ($\boldsymbol{DP_{av}}$) is high, η will be small and the flow distribution will be good. If the dynamic pressure ($\frac{1}{2}\rho V_o^2$) is high compared with the pressure drop, η will be high (>1) and the maldistribution will be severe. In Table 3.1, η is calculated for various data points.

$$h = \sqrt{\frac{\Delta P_{header} + \Delta P_{av}}{\Delta P_{av}}} \tag{3.1}$$

where

$$\Delta P_{header} = r\left(\frac{V_o^2}{2} + h_{lm}\right) \qquad h_{lm} = f \cdot \frac{L_e}{D} \frac{V_o^2}{2} \tag{3.2}$$

$$f = \frac{.3164}{Re^{.25}} \text{ for turbulent flow in smooth tubes} \qquad \frac{L_e}{D} = 60 \text{ (branch assumption)}$$

The dynamic pressure variations in the inlet and outlet header are adjusted with a head loss coefficient, h_{lm}, (Fox and McDonald, 1992) to account for the losses due to the flow splitting in half and turning 90°, where V_o is the average of the velocities entering and leaving the turn. The average pressure drop across the tubes, $\boldsymbol{DP_{av}}$, is the frictional pressure drop through the tubes, which we obtained from simulating uniformly distributed flow through the condenser.

Table 3.1 Pressure drop calculations for the condenser

Re_inlet	$\Delta P_{inlet\ header}$ [psid]	$\Delta P_{outlet\ header}$ [psid]	ΔP_{tubes} [psid]	η
67600	0.006	0.0002	0.17	1.07
77500	0.009	0.0002	0.19	1.08
90260	0.011	0.0002	0.24	1.08
127700	0.019	0.0005	0.37	1.09

Table 3.1 shows the relative magnitudes of these terms for a range of flow conditions. They indicate that the dynamic pressure is much less than the pressure drop across the condenser tubes. Therefore dynamic pressures variations along the header cannot be the cause of severe maldistribution in the condenser.

Originally, the condenser coil was designed by Kirkwood and Bullard (1999) in the 'V' shape to fit inside typical condenser housing and to shed condensate and frost efficiently if it were run in heat pump mode. In retrospect, it is clear that using the coil in the 'V' position for a/c operation promoted flow maldistribution. As the two-phase fluid begins to condense and slow down, its velocity decreases from 3 ft/s to 0.25 ft/s. If it is fully condensed at the bottom of the 'V', it must work against 2.9 ft (1.2 psi) gravitational head associated with the subcooled liquid. System simulations show that with moderate "design target" subcooling (~8°F) 10% of the

condenser area will be subcooled, creating a gravitational head (h ≈ 0.55ft, ΔP_{static} ≈ 0.3 psi) that will be much larger than the combined frictional pressure drop across the tubes and inside the headers. The static pressure head will gradually cause much of the tube to fill with liquid, reaching a maximum of nearly 1.2 psi when the entire upward-flowing section is filled. Therefore, even if the inlet header were designed perfectly, this particular condenser geometry could still experience severe flow maldistribution due to gravitational effects.

3.4.2 Experimental results

To determine whether maldistribution was occurring in the condenser coil, all 40 surface thermocouples across the condenser exit were monitored for various mass flow rates and condensing pressures. The results are presented in Figure 3.4. The y-axis of Figure 3.5 was non-dimensionalized by dividing the subcooling seen in each tube (T_{cond} - T_{tube}) by the maximum subcooling possible (T_{cond} - T_{amb}).
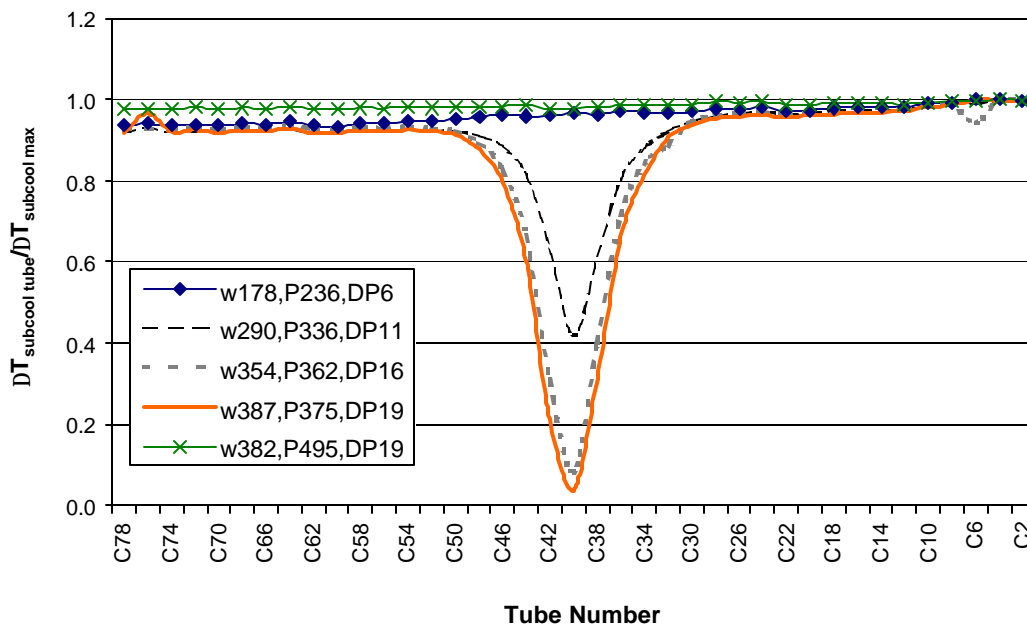
Figure 3.4 Maldistribution along condenser exit tubes

The units for the variables are as follows: w [lbm/hr], P [psia] and DP [psid]. Each thermocouple reading is assumed to represent two microchannel tubes and the discharge line enters the header near tube number 40. Figure 3.4 confirms the hypothesis that gross maldistribution exists and suggests that most of the flow leaving the discharge line travels directly down the center tubes. All other tubes in the coil indicate exit temperatures within 1°F of ambient. Only the tubes seeing the maximum velocity exiting the discharge line have enough dynamic pressure to establish flow patterns that have little or no exit subcooling. For these tubes, virtually all pressure drop is frictional. Most of the other tubes begin to fill with liquid, and gravitational head may quickly dominate the frictional pressure drop, reducing mass flow rate accordingly. The center tubes may have mass flow rates greater than average, sending two-phase flow into the exit header. Additional condensation may then occur downstream, via direct contact with subcooled refrigerant in the exit header and liquid line, upstream of our liquid line pressure and temperature measurements.

14

Figure 3.4 does show some trends for the maldistribution. As mass flow rate and pressure increase, more tubes become "active" in the sense that their subcooled regions are relatively small or nonexistent. When the condenser pressure approaches the critical point for R410A (703 psia), the distribution is even across the exit due to the highly subcooled conditions in each tube. Condenser sub-model simulations show that as the condenser pressure passes 475 psia, the subcooled area of the condenser encompasses more than 50% of the total heat exchanger area. These conditions may result in a plenum effect that forces all tubes to be more than half full of highly subcooled liquid, distributing flow relatively uniformly because of the 1.2 psi gravitational head associated with the 2.9ft liquid column in the downstream half of the tubes. The area of the superheated region also increases while that of the two-phase region decreases.

The number of thermocouples that could be recorded by the data acquisition system was limited to 50. Therefore, it was impossible to record all 40 condenser exit thermocouples during the data acquisition period. However, the seven center tube thermocouples were read for all test conditions to watch for trends. The slight slant in the data presented in Figure 3.4 is due to a small gradient in the temperature of the ambient air entering the condenser when the 40 thermocouple profile points were recorded. Prior to taking data for the entire test matrix, the airflow distribution in the outdoor chamber was modified to produce a uniform air inlet temperature to the condenser.

3.4.3 Model simulations

As mentioned in section 3.3.1, the measured pressure drop across the condenser headers was ten to twenty times greater than that predicted by the model. The dynamic pressure losses due to turns and entrance/exit effects in the headers and frictional losses in the tubes combined cannot explain the large measured pressure drop, since gravitational head loss sets an approximate upper limit (~1.2 psi) on the pressure drop across the headers. Figure 3.4 suggests most of the condensation is occurring in tubes 32 to 47, and that some of these have two-phase exits. Therefore the entire pressure drop in these tubes could be frictional, but no greater than the ~1.2 psid gravitationally dominated pressure drop in the other tubes which are carrying lower mass flows. To generate a 1.2 psid frictional pressure drop, a mass flow rate ~2.5 times the average would be required. This provides a rough estimate of the extent of condenser flow maldistribution and an upper limit on the pressure drop between the headers.

In another attempt to establish rough bounds on the pressure drop and maldistribution, the condenser-only simulation was run again, this time changing the number of tubes from 79 to 15. Figure 3.5 shows that the 15 tube simulation reduces the error for the condenser capacity prediction from a mean of 2.8% to a mean of 1%. The prediction for ΔTsubcooling improves dramatically, from a average ΔT ($T_{predicted}$-$T_{measured}$) of 9°F to an average ΔT of 0.8°F as seen in Figure 3.6. The calculated pressure drop for this hypothetical case is 3 psid, suggesting that 20 might be a better estimate of the number of "actively flowing" tubes that would produce a pressure drop comparable to the 1.2 psid maximum gravitational head in the other "inactive" tubes.

In summary, the chief cause of the maldistribution observed in the condenser appears to be the 'V' configuration. Therefore, it should be easy to avoid in future designs. The pressure drop introduced by maldistribution is apparently quite small, but it could not be confirmed without installing a pressure transducer across the header. It is possible that most of the measured pressure drop is occurring in the reverse flow through the heat pump distributor and valve, which in some cases could cause the pressure to drop below the saturation pressure and

flash. It is also likely that bubbles are often carried into the distributor by one of the eight tubes leaving the exit header, which could then exacerbate pressure drop in the distributor.
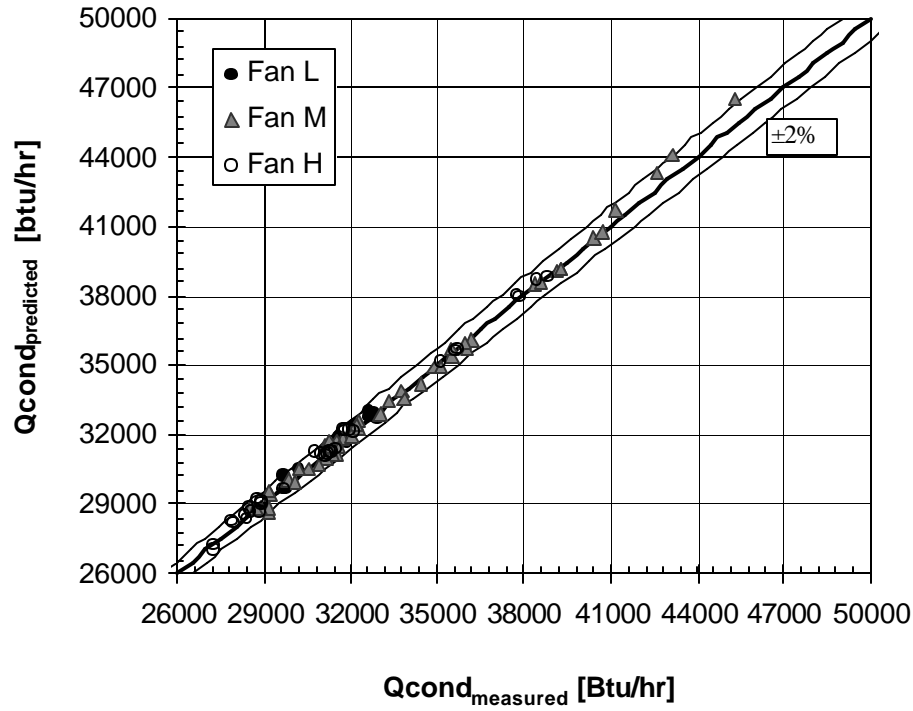
Figure 3.5 Capacity performance for 15 tube simulation
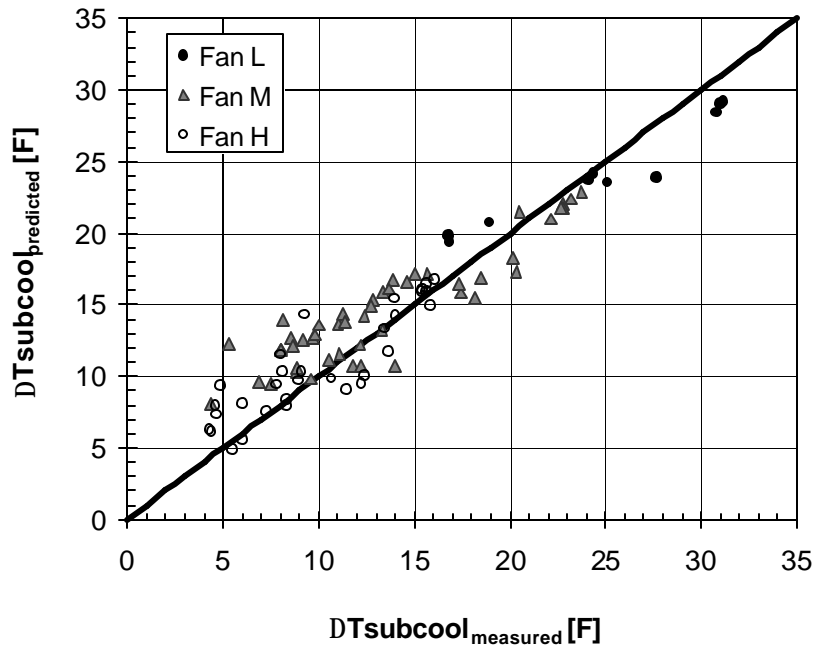
Figure 3.6 ΔTsubcool performance for 15 tube simulation

3.5 Effects of maldistribution on refrigerant charge

      The additional 0.8 lbm of refrigerant charge need to match the measured subcooling with the predicted can now be explained by the flow maldistribution in the condenser coil. For the 80/82/wet point that the system was charged to match, half of the condenser coil could have been filled with liquid. A rough re-calculation of charge was done to determine if the maldistribution could account for all of the ext ra charge added to the system. The charge needed for the 15 active tubes was estimated using the model in design mode, setting subcooling equal to the experimentally observed value, 8.6°F. The remaining 64 tubes were assumed to be 50% liquid, 32% two-phase and 18% superheated. This breakdown was selected by running the model again, this time setting subcooling to the maximum possible value, T_{cond}-T_{amb} = 20, for the 80/82/wet condition. The sum of the 64 tube simulation and the 15 tube simulation brought the total charge in the condenser to 3.2 lbm. The estimated total system charge accounting for maldistribution was 6.78 lbm, much closer to the 6.66 lbm required in the lab.

3.6 Discussion of results

3.6.1 Header design

      Analysis has shown that the driving force for the maldistribution in our condenser coil was the orientation of the coil. To prevent this problem in the future, one uniform flow direction should be used in the condenser, preferably downward flow because horizontal tubes would not shed condensate or frost in heat pump mode.

      Increasing the pressure drop across the tubes would also provide an additional improvement in flow distribution by minimizing the effect of dynamic pressure losses. For the operating range of the condenser (300-600 psi), a sacrifice of 10 psi across the tubes would result in only a 2°F condensing temperature loss, minimally decreasing EER by 0.07%.

      Reverse flow was not a concern for the header in our system. If the inlet header was shorter in length or had a larger diameter, reverse flow due to vortex generation could become a serious problem. Lalot *et al.* suggests the addition of a perforated grid in the inlet header, located midway between the inlet tube and the core of the header to prevent vortex generation. The grid has been shown to homogenize the flow, decreasing the velocity ratio, η and in turn improving flow distribution.

Chapter 4: Evaporator Maldistribution

4.1 Introduction

Experimental data showed that the evaporator was performing about 15% below its predicted capacity. Maldistribution was considered to be a potential cause for the capacity loss due to the difficulty of distributing two-phase flow in headers. To investigate and quantify the effects of maldistribution, experimental data was used in conjunction with the model to analyze various hypothetical situations inside the evaporator inlet header.

4.2 Experimental setup

4.2.1 Evaporator configuration

The final evaporator coil design includes 40 microchannel tubes, each tube having 19 trapezoidal ports. All 40 tubes (760 ports) are connected to 1.29ft long (diameter 0.75") inlet and exit headers. Four distributor tubes feed into the inlet header after exiting the thermal expansion valve (TXV) which adjusts the mass flow rate in response to the exit conditions ensuring 10°F superheat. A front view of the coil is pictured in Fig. 4.1.
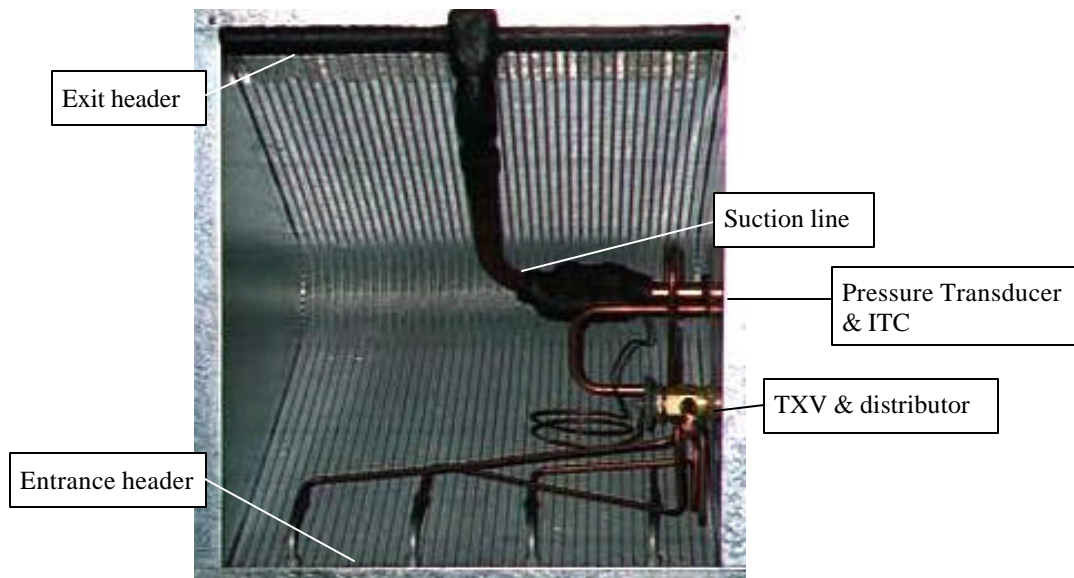
Figure 4.1 Evaporator inlet header and distributor

4.2.2 Experimental instrumentation

Similar to the condenser, the evaporator coil was extensively instrumented. An absolute pressure transducer was attached to a pressure tap at the exit of the evaporator to record the suction line pressure. An immersion thermocouple was placed two feet downstream from the exit header. An additional immersion thermocouple was placed at the exit of the liquid line, before the entrance to the TXV. To investigate maldistribution, 23 surface thermocouples were attached to the middle of the unfinned portion of microchannel tubes that fed into the evaporator exit header (See figure 4.2). After the thermocouples were attached, all air flow was blocked across the thermocouples by filling gaps with foam insulation in an attempt to keep the tube surface within 0.5 °F of the refrigerant temperature.
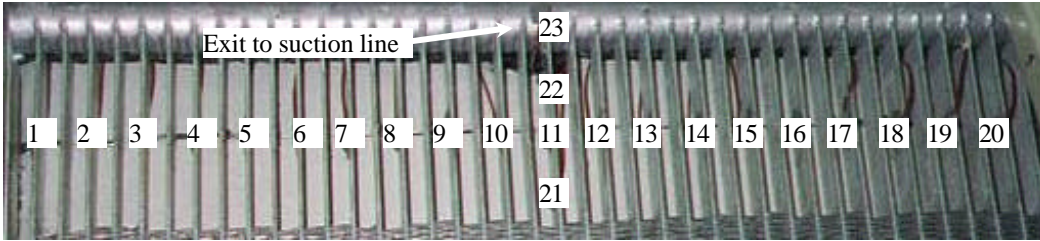
Figure 4.2 Evaporator exit header with 23 type-T surface thermocouples

Data from these thermocouples revealed interesting trends. Figures 4.3a b and c show the temperature profiles across the evaporator tubes for the three blower speeds tested under dry coil conditions.   The y-axis was non-dimensionalized by dividing the superheat seen in each tube (T_{tube}-T_{evap}) by the maximum superheat possible (T_{amb} - T_{evap}) The vertical black lines on each graph represent the locations where the feeder tubes enter the evaporator header. The profiles for the high and low fan speeds (Figures 3.a and 3.c) are almost identical for all test conditions. The medium fan speed results (Figure 3.b) show greater differences between test points, possibly due to the wider range of mass flow rates tested. Graphs for all of the test points, wet and dry coils, can be viewed in Appendix E. The thermocouple data confirms that indeed, a great amount of maldistribution occurs in the evaporator and that the solution was highly repeatable. Further analysis of the graphs will be presented in section 4.2.3.
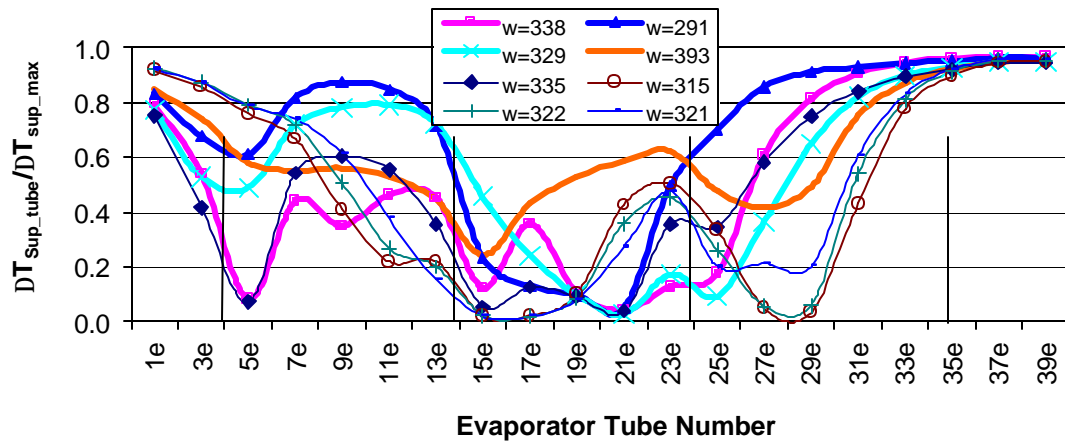
Figure 4.3a Exit temperatures of evaporator tubes for dry, low blower test points
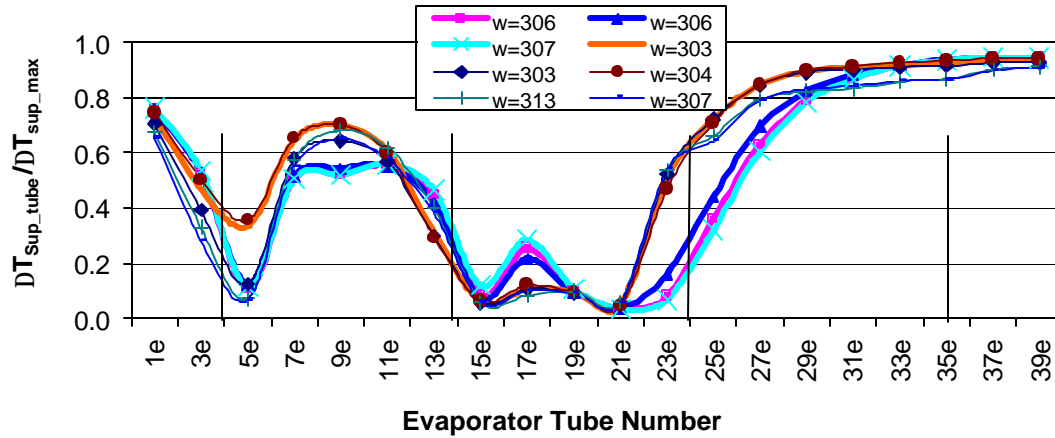
Figure 4.3b Exit temperatures of evaporator tubes for dry, med blower test points
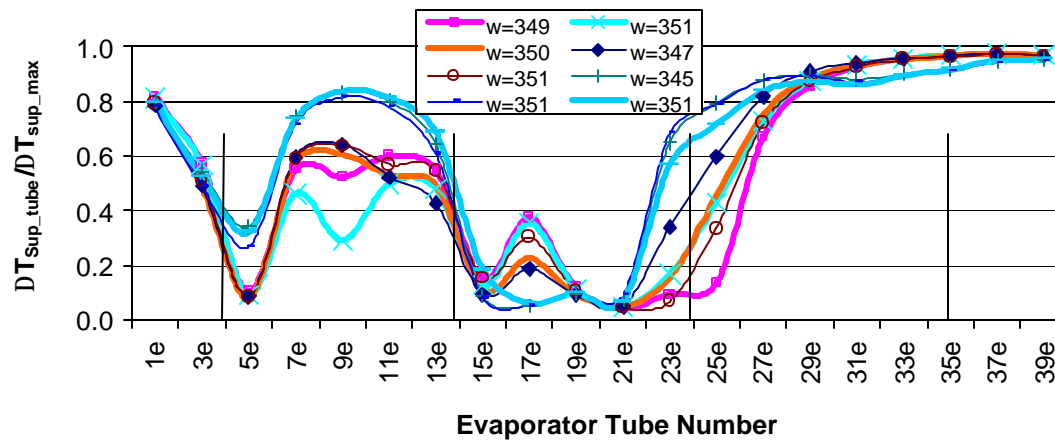
Figure 4.3c Exit temperatures of evaporator tubes for dry, high blower test points

4.2.3 Evaporator header design

Conventional 3/8" copper tube evaporators are fed directly from an adiabatic two-phase flow distributor in which there is a 1:1 relationship between mass flow and pressure drop. If the pressure drop varies slightly across the distributor, the mass flow rate should remain relatively constant as it exits the feeder tubes.

Standard a/c evaporator distributor

Microchannel feeder tubes & header   **Side view**
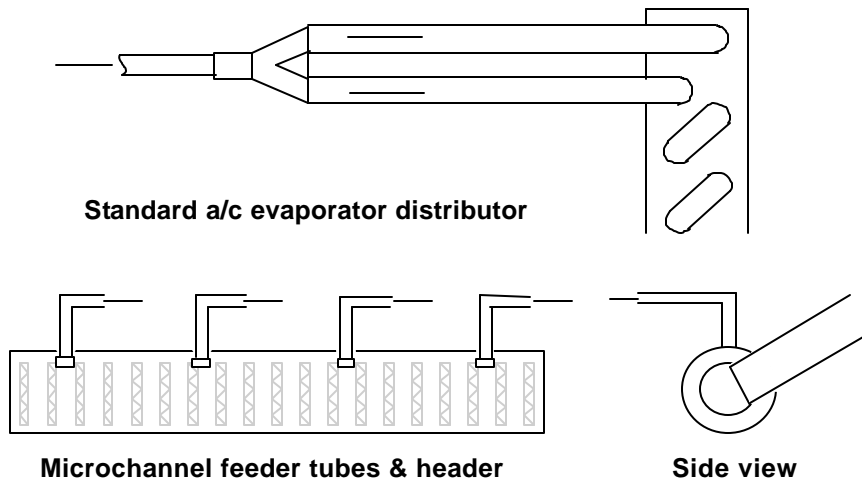
Figure 4.4 Conventional distributor configuration vs. microchannel header

Figure 4.4 shows the standard feeding mechanisms for both a conventional 3/8" copper tube evaporator and a microchannel evaporator. The microchannel evaporator differs from conventional systems because more than 760 ports have to be fed from a single cylindrical header instead of the standard 2-6 tubes used in a conventional system. The header receives the flow exiting the distributor, at four points equally spaced along the header. This design is intended to provide a constant inlet enthalpy to all of the microchannel ports. However, our distributor is mounted horizontally, and the Froude number is on the order of one. Therefore gravitational effects may cause stratification of the two-phase flow entering each feeder tube.

Figure 4.5 shows the distributor orientation and the corresponding feeder tubes. The tubes exiting the top of the distributor will have a higher quality (mostly vapor) than the tubes exiting from the bottom of the distributor (mostly liquid). The dynamic pressure in tubes 2 and 4 will be relatively large due to the high vapor content of the refrigerant exiting into the header. This dynamic pressure is estimated to be ~5 times greater than the dynamic pressure of the lower quality refrigerant. Therefore, when the flow splits in two as it exits the feeder tube, it has to compete with what is exiting the tubes next to it. Most of the vapor exiting tube 4 will immediately feed into the ports to the right, creating a vapor plenum that is impenetrable by the lower dynamic pressure, lower quality refrigerant. The other three feeder tubes will mix accordingly.
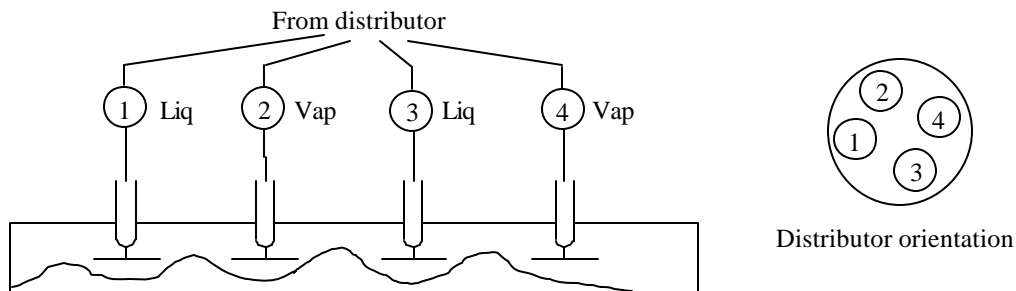
Figure 4.5 Evaporator distributor orientation

Looking back at Figures 4.3a, b and c, this hypothesis is supported by the temperature profiles. All of the tubes located on the right side of the header (35-40) appear to be fed mainly from tube 4 and typically display high superheat, suggesting higher inlet quality. The breadth of the superheated range extends beyond the tubes that number 4 feeds. This could be explained by the blower position inside the housing. The draw-through blower is slightly offset from the center of the coil, with the intake closest to the left side of the evaporator coil. As the blower speed increases, the number of superheated tubes on the right decreases, perhaps because the increased air-flow rate causes the pressure drop across the evaporator to overwhelm the effect of asymmetry.

It was hypothesized that more might be occurring in the evaporator header than could be explained by non-uniform inlet quality at the tubes and ports. The temperature profiles do not always correspond to what would be expected from the distributor tube configuration. Due to experimental constraints, it was impossible to access the inside of the inlet header to see exactly what was occurring. We therefore relied on simulation analysis to gain some insights about what was occurring in each tube.

4.3 Maldistribution investigation

4.3.1 Computer simulations

One hypothesis was that there exists an inherent instability in microchannel evaporators that causes maldistribution. Starting with the assumption that all evaporators must maintain a constant pressure drop across the headers, a computer simulation was developed. Six inputs were required to solve the evaporator sub-model, three air-side inputs and three refrigerant-side inputs. The air-side inputs were fairly straightforward, temperature, mass flow rate and the pressure of the air entering.

Before determining the refrigerant side inputs to the model, some assumptions had to be made to normalize all of the simulations. First, it was assumed that the evaporator feeder tubes were operating as they were designed to, providing each port with the identical inlet enthalpy. The inlet enthalpy was set to the value that corresponds to 10 degrees of subcooling with a 100°F condensing temperature. The second input was selected to be the exit pressure of the evaporator. This value was chosen because all tubes will "see" the same exit pressure. Realistic values for the exit pressure could be obtained from the absolute pressure transducer located at the entrance of the suction line. The final input was the refrigerant mass flow rate, obtained from the coriolis-type meter while also allowing the option of being able to vary the input value. Figure 4.6 shows the sub-model configuration.
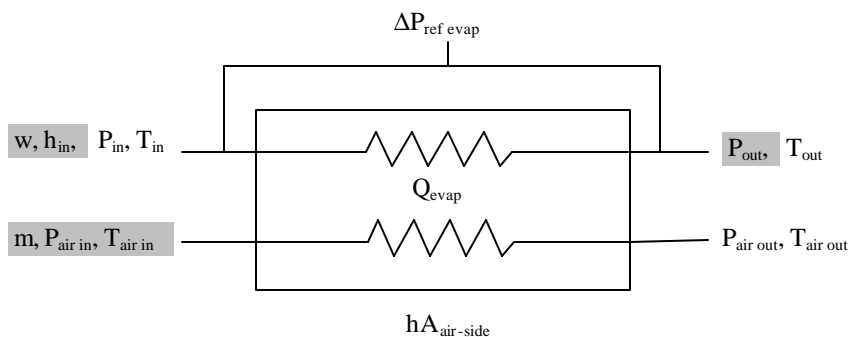
Figure 4.6 Evaporator simulation submodel

22

4.3.2.1 Varying mass flow rate

Using the modeling configuration listed above, the evaporator sub-model was run using R410A as the refrigerant with measured data used for the inputs. To investigate the effect of varying mass flow rates between each tube, the inlet enthalpy was held constant while the mass flow rate varied from 200 lbm/hr to 500 lbm/hr. Remarkably, as seen in Figure 4.7, three different mass flow solutions may exist for a single inlet enthalpy and exit pressure, since pressure drop will be the same for all tubes.
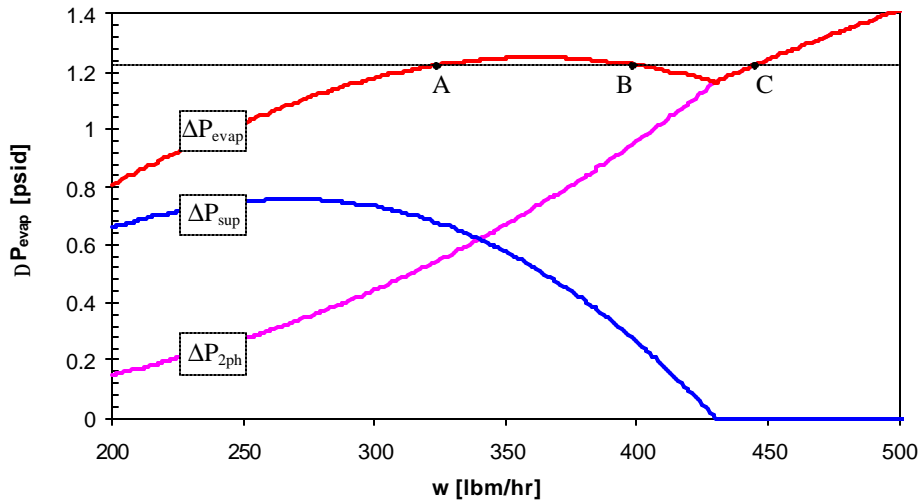
Figure 4.7 Pressure drop across the evaporator due to varying mass flow

Consider the case where the pressure drop across the headers is 1.21 psi and each port sees the same inlet quality. As seen in Figure 4.7, the mass flow rate can vary from port to port. As mass flow rate increases from 300 lbm/hr to 425 lbm/hr the rate of change for the pressure drop in the superheated region is equal and opposite to the rate of change in the two-phase region. This relationship between the two pressure drop regions results in an extremely flat area where the pressure drop is relatively constant while the mass flow rate changes significantly. This flat pressure drop profile can result in three vastly different solutions (A, B & C) for exit superheat and capacity as seen in Figure 4.8.
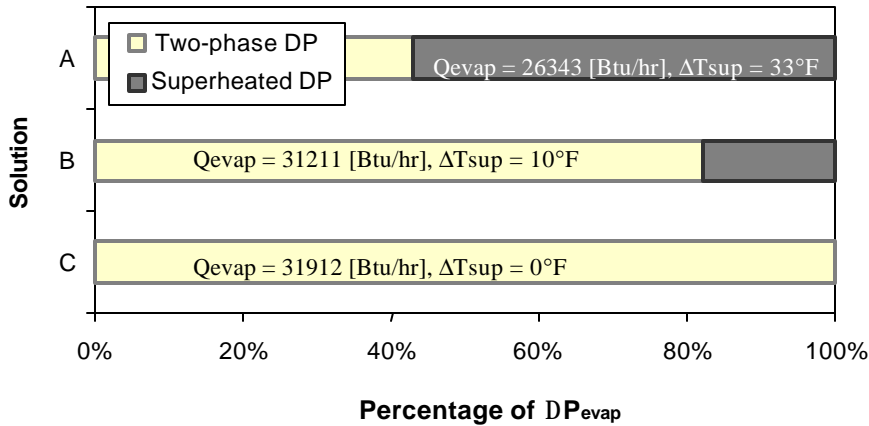
Figure 4.8 Triple solution results for pressure drop

Figure 4.8 shows the first solution, 'A' with the lowest mass flow rate at 320 lbm/hr, the superheated area is 25% of the total area, and the superheated pressure drop accounts for more than half of the total pressure drop in the tube. As the mass flow rate increases, the superheated area decreases at the second solution, 'B' with a mass flow rate of 405 lbm/hr. This solution is considered the 'ideal' because this was the condition the coil was designed for, with 10°F superheat contributing 18% of the pressure drop. Finally, solution 'C' has the highest mass flow rate, 445 lbm/hr, with the entire tube being two-phase with an exit quality of 0.98.

The total mass flow, summed across all tubes and ports, is controlled by the thermostatic expansion valve so that the average superheat at the exit is 10°F. However, there is no unique combination of solutions A,B and C that will provide 10°F of superheat. To quantify the possible magnitudes of evaporator capacity loss due to the triple solution effect, different hypotheses that corresponded to an average superheat of 10°F were investigated. Assuming that 30% of the tubes had solution 'A', 50% solution 'B' and 20% solution 'C', the resulting capacity would be 4% less than the ideal solution, B. If more tubes exited highly superheated; 50% solution 'A', 17% solution 'B' and 33% solution 'C', the resulting capacity shortfall would be 7%.

To investigate whether or not the requirement of equal mass flow rates and inlet enthalpies was unique to microchannel evaporators, the model was used to simulate a 3/8" copper tube evaporator with R410A. The simulations resulted in a profile identical to Figure 4.7. This means that the constant inlet enthalpy and mass flow rate requirement is not unique and is present in all evaporators. This problem has never presented itself before due to the use of distributors in conventional 3/8" tube systems that guarantee a constant flow rate and enthalpy entering each tube.

These simulations show that providing a constant inlet enthalpy to each port is not sufficient to prevent maldistribution. Both a constant mass flow rate and inlet enthalpy must be achieved for the flow to be evenly distributed. However, since the exit temperature profiles in Figures 4.3a, b and c show more than three unique solutions for the exit temperature, it was assumed that the tubes were not being fed with constant inlet enthalpy. Model simulations in the next section investigate the capacity loss if both mass flow and inlet enthalpy vary at the inlet.

4.3.2.2 Varying inlet quality

All simulations up to this point have assumed that each port was seeing a constant inlet quality. When the flow enters the distributor, the inlet enthalpy is constant. However, as discussed in section 4.2.3, the distributor was installed in a horizontal position allowing for the flow to be divided non-uniformly among the four inlet streams. Simulations were run varying inlet quality and mass flow rate and the results can be seen in Figure 4.9.
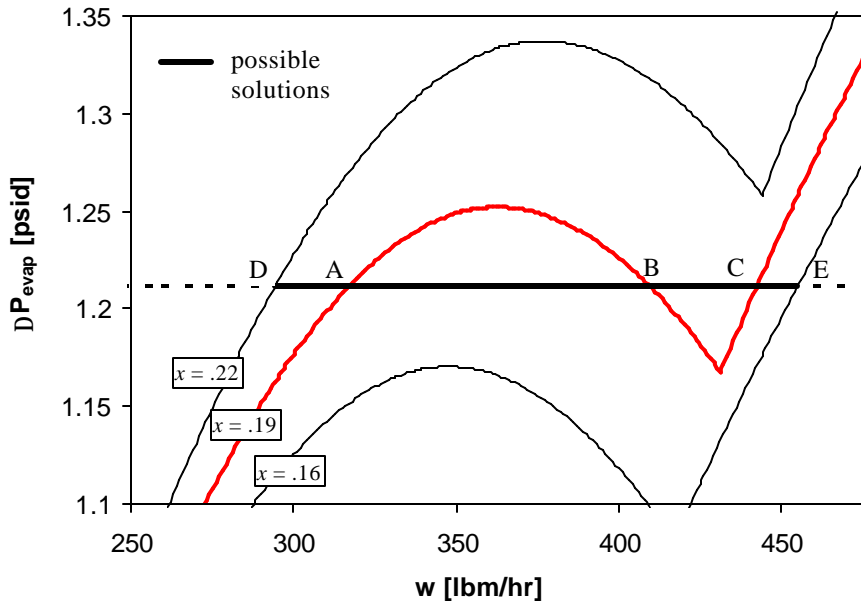
Figure 4.9 Pressure drop solutions with variable inlet quality and mass flow rates

Figure 4.9 has the same model inputs as Figure 4.7. However, for this simulation, the inlet quality was varied until the 'possible solution' range included all of the experimentally measured exit temperatures. Points A, B and C show the mass flow rates corresponding to the triple solution discussed in section 4.3.2.1. The same 1.21 psi pressure differential between the inlet and outlet headers is assumed, assuming that all tubes are being fed at the average quality of $x = 0.19$. Tubes fed with inlet quality $x = 0.16$ would have a two-phase exit at quality, $x = 0.92$ (E), while the tubes seeing inlet quality $x = 0.22$ would have the lowest mass flow rate (D) and a highly superheated exit $\Delta T_{sup} = 38°F$. The possible range of solutions now includes the highest superheated points as well as the two-phase exits seen in the experimental results. Therefore, inlet quality must vary by ± 0.04 for the simulated exit temperatures to match the measured exit temperatures. The maldistribution in this case resulted in a capacity loss of 10%.

4.3.3 Header pressure drop

Maldistribution can also be caused by inertial effects inside the header that expose parallel circuits to different driving pressure differentials. The design of the headers, providing four lines to feed the inlet and only one outlet to the suction line, may create a non-uniform distribution of velocities across the inlets and exits of the tubes. Equation 4.1 was used to calculate the pressure losses in the inlet and outlet headers for various mass flow rates, assuming 10°F exit superheat. Additional losses from the flow having to split and turn 90° is approximated with the

head loss coefficient, h_{lm} and using the average velocity entering and leaving the turn (Fox and McDonald, 1992). The results are listed in Table 4.1.

$$\Delta P_{header} = r\left(\frac{\overline{V}^2}{2} + h_{lm}\right)$$

$$(4.1)$$

$$h_{lm} = \frac{.3164}{Re^{.25}}\frac{L_e}{D}\frac{\overline{V}^2}{2}$$

Table 4.1 Pressure losses in evaporator

w [lbm/hr]	$\Delta P_{inlet\ header}$ [psid]	$\Delta P_{outlet\ header}$ [psid]	ΔP_{tubes} [psid]
270	.023	.073	1.1
350	.028	.090	1.3
450	.035	.113	1.8
535	.041	.138	2.5

The tubes entering the center of the outlet header will see the greatest dynamic pressure effects at their inlets, while at the ends of the header, the dynamic pressure will be zero. This effect is illustrated qualitatively in Figure 4.10. Since Table 4.1 shows that the pressure variations due to velocity changes within the header are small relative to the frictional pressure drop in the tubes, DP_{tubes}, between the headers, these effects can be ignored in the evaporator.
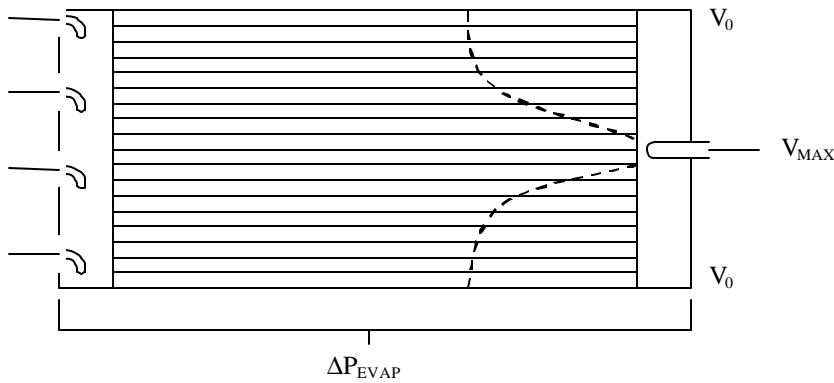
Figure 4.10 Velocity effects in the evaporator exit header

4.4 Minimizing maldistribution

Maldistribution can be minimized in microchannel evaporators by two different design options. First, the geometric parameters of the evaporator coil can be designed to increase the slope of the pressure drop curve by increasing the total pressure drop across the evaporator. Second, a refrigerant can be selected whose thermodynamic properties result in a steeper pressure drop curve.

4.4.1 Variation of geometric parameters

The flat area in the pressure drop solution occurs when the pressure drop across the evaporator tubes is small. If the pressure drop from the inlet to the exit of the tube is increased, the pressure drop versus mass flow rate

curve becomes steeper and the range of possible solutions will decrease. In other words, mass flow rate becomes less sensitive to small perturbations in pressure drop between the headers. It also becomes less sensitive to perturbations in inlet quality. Of course, increased pressure drop degrades performance. For the R410A evaporating pressure range (100-200 psia), a sacrifice of 5 psid across the tubes will result in a 1°F penalty in evaporating temperature.

Simulations were run varying port diameter, tube length, number of tubes and number of ports per tube. All simulations resulted in raising the total pressure drop and increasing the slope of the pressure drop curve. It does not matter which parameter is varied, as long as it is varied in such a manner that the total pressure drop is increased to the desired magnitude. What the designer chooses to vary will ultimately depend on system housing constraints and manufacturing capabilities. For the system described in this paper, a simulation was run increasing the number of ports per tube from 19 to 31 and decreasing the trapezoid height by 33%. These geometric values, keep the refrigerant-side area and the tube width constant, while increasing mass flux. Figure 4.11 shows the total pressure drop curves for the two simulations (assuming constant inlet quality), with error bars indicating the range of possible solutions due to dynamic pressure variations along the headers. For the prototype coil (19 ports/tubes, $D_h = 0.03"$), the flat region spans an area 40% larger than the simulation designed for increased pressure drop (31 ports/tubes, $D_h=0.019"$). The 4 psi increase in pressure drop across the coil results in a 1°F penalty in evaporating temperature.
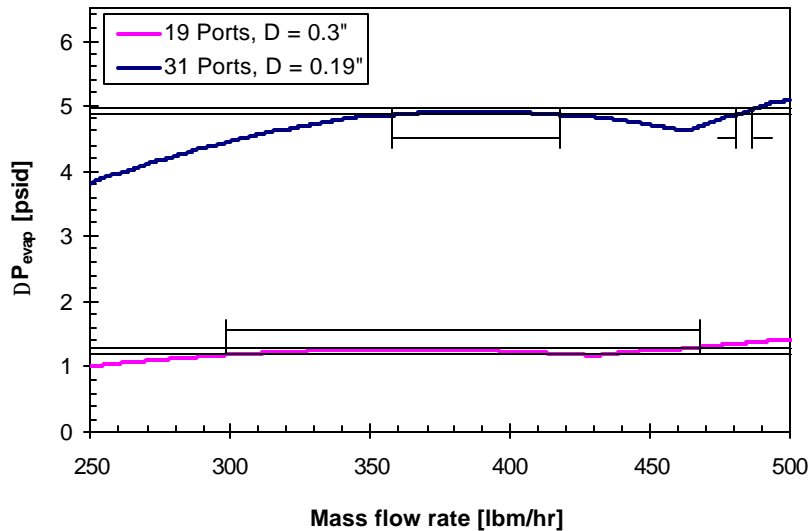
Figure 4.11 Effects of changing tube number and port diameter

4.4.2 Effects of refrigerant choice

The flat region of the pressure drop curve is the result of equal and opposite slopes for the superheated and two-phase pressure drop. It was hypothesized that if a refrigerant were selected where the two-phase pressure drop was much greater than the pressure drop in the superheated region, the two-phase pressure drop would be the dominant contributor to the total. If this were the case, the cancellation effect of the two slopes would be reduced and the possibility of a triple solution would be minimized.

Due to constraints in the current version of the simulation model, only the following refrigerants could be simulated: R410A, R22, R407C, R134a and R12. To include comparisons with alternative refrigerants, a relationship was developed for the ratio of the superheated pressure drop to the two-phase pressure drop, based on the thermodynamic properties of the refrigerant. This relationship is derived in equations 4.2-6. The ratio of pressure drops (Eq. 4.2) was viewed as a function of two factors, the ratio of the length of the superheated region to length of the two-phase region (Eq. 4.3) and a ratio referred to as the "F" factor (Eq. 4.5). To calculate pressure drop in the single-phase region of the evaporator, Colebrook's (1939) correlation was used. De Souza's (1995) correlation was used to calculate two-phase pressure drop.

$$\frac{\Delta P_{sup}}{\Delta P_{2ph}} = \left(\frac{F_{sup}}{F_{2ph}}\right)\left(\frac{L_{sup}}{L_{2ph}}\right) \tag{4.2}$$

The simulations for the various refrigerants listed above led to the conclusion that the length ratio (4.3) varies linearly with superheat over the 0-25°F range. The slope (~ 0.05) and intercept (0) are almost equal for all refrigerants considered. Therefore, F is the only variable distinguishing refrigerants. The factor F is a ratio of friction factors and thermodynamic properties (4.5). The higher the value for F, the greater the propensity for the refrigerant to exhibit maldistribution. Table 4.2 presents the values for the refrigerants evaluated.

$$\frac{L_{sup}}{L_{2ph}} \approx 0.05 \ \text{for all refrigerants} \tag{4.3}$$

$$F_{sup} = \frac{2G^2 f_{Moody}\, v_{avg}}{D_{ht}} \qquad\qquad F_{2ph} = \frac{\dfrac{2G^2 f_{lo}}{D_{ht}\, r}\int_{x_{in}}^{x_{out}} f_{lo}^2}{x_{out} - x_{in}} \tag{4.4}$$

$$\frac{F_{sup}}{F_{2ph}} \approx \frac{f_{Moody}\, v_{sup}}{f_{lo}\, v_{lo}} \approx F \tag{4.5}$$

$$\frac{\Delta P_{sup}}{\Delta P_{2ph}} \approx F \cdot \text{constant}$$

$$\tag{4.6}$$

Table 4.2 *F* values for various refrigerants

Refrigerant	v_{sup}/v_{2ph}	f_{sup}/f_{2ph}	F
R11	516	0.004	2.0
NH$_3$	156	0.017	2.7
R134a	76	0.046	3.4
R12	67	0.052	3.5
R407C	55	0.066	3.6
R22	52	0.072	3.7
Propane	44	0.087	3.9
R410A	33	0.126	4.2
R404A	31	0.147	4.3

CO$_2$	8	0.742	6.0

Figure 4.12 is the simulation result for R134a, a refrigerant that has a lower value of *F* than R410A. The graph shows that mass flow rate is less sensitive to pressure drop variations for a refrigerant with a lower *F* value operating at the same inlet conditions described in section 4.3.1. However, this simulation shows R134a performance in a system that was optimized for R410A. Many other factors are affected with refrigerant selection and for our purposes, R134a and other refrigerants with a lower *F* value are not ideal for a minimum-TEWI system.
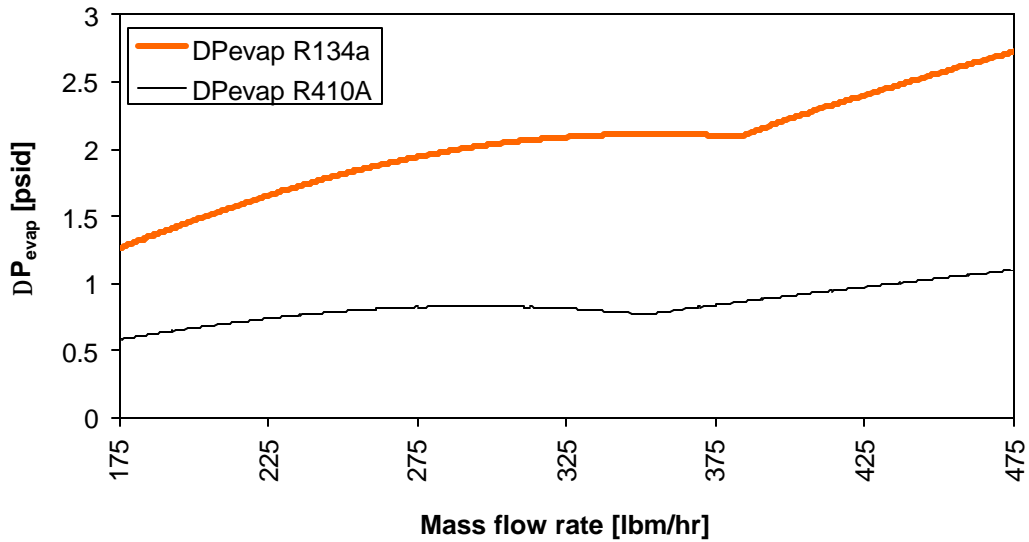
Figure 4.12 Comparison of R134a and R410A pressure drop curves.

Chapter 5: Recommendations for Minimum-TEWI System Design

5.1 Introduction

The overall goal of this project was to design and test a microchannel split system so that the system model could be validated. Once validated, the model could be used to optimize the system design with the objective of minimizing the system's total equivalent global warming impact (TEWI). There are two TEWI factors contributing to the total: the direct effect caused by refrigerant leakage into the atmosphere and the indirect effect, resulting from CO_2 emissions associated with the energy consumption of the system. The indirect effect typically contributes to 90% of the total TEWI.

In stage one of this project, Kirkwood and Bullard (1999) focused on minimizing TEWI per unit capacity, for a prototype system that was to be constructed from readily available components, and subject to packaging constraints typical of conventional systems. This chapter will provide final recommendations for a minimum-TEWI system that uses components that are not currently available commercially. There are many ways to decrease the indirect component of TEWI, perhaps as much as 30%, by making systems more efficient. However, to accomplish this without increasing the direct effect (refrigerant charge) would require use of alternative refrigerants or microchannel heat exchangers.

5.2 Refrigerant selection

Since the United States and other nations signed the Kyoto Protocol, pledging to reduce CO_2 emissions to 7% less than the 1990 baseline for the period of 2008-2012, manufacturers of residential a/c systems have been considering two hydrofluorocarbon (HFC) alternatives to HCFC 22: R407C and R410A. Both are mixtures, and R410A seems to be favored because of its nearly azeotropic behavior, which minimizes problems associated with leakage and maintenance. However its global warming potential is about equal to that or R22. Therefore it is necessary to avoid, if possible, increasing substantially the system charge requirement as heat exchanger size in increased in pursuit of greater energy efficiency. For that reason microchannel heat exchangers, with their relatively large internal surface-to-volume ratio, appear to be an essential element of any minimum-TEWI system design.

For different reasons, charge minimization is also an essential element of any minimum-TEWI system based on natural refrigerants (e.g. hydrocarbons, ammonia or carbon dioxide). For hydrocarbons and ammonia, flammability and toxicity dictate that charge be minimized, while for carbon dioxide its high pressure (150 bar) requires the use of small-diameter refrigerant tubing to control heat exchanger cost and weight. Therefore the results of this project have broader applicability than the minimum-TEWI R410A prototype studied here.

5.3 TEWI system components

For this initial prototype, components were designed solely to minimize TEWI with little concern for cost constraints. Each component recommendation is intended to maximize the component's efficiency (indirect effect) while minimizing the amount of charge required (direct effect).

5.3.1 Heat exchangers

Microchannel tubes are the optimal choice for both the evaporator and condenser coils. The compact nature of microchannel tubes leads to a minimal amount of charge required to achieve a given capacity. The large

refrigerant-side area also increases dehumidification performance, relative to conventional circular tube-flat fin evaporators. The major obstacle in the design of microchannel heat exchanger is flow maldistribution.

5.3.1.1 Evaporator

Perfect distribution in the evaporator can only be obtained if every port in the coil sees the identical mass flow rate and inlet quality. Maximizing the number of distributor tubes that feed into the inlet header will help homogenize the flow. Adding dividers inside the header between each feeder inlet will also aid keeping the quality constant. However, until each port can be fed individually, it is impossible to achieve perfect distribution.

To limit the extent of flow maldistribution, the evaporator coil should be designed to sacrifice a large enough pressure drop so that large changes in mass flow rate result in only small changes in the evaporator exit superheat. For an R410A system, a 5 psi pressure drop could be obtained most easily by changing from a one-pass to a two-pass design. However due to the risk of introducing maldistribution at that point, the same objective could be accomplished by reconfiguring the microchannel ports in a one-pass design to halve their aggregate cross-sectional area without significantly reducing refrigerant-side surface area. Reducing the internal tube volume would also provide the additional benefit of decreasing the amount of charge in the evaporator by 50%. Such a pressure drop induces a 1ºF reduction in evaporating temperature, which would reduce system capacity by 2% from the baseline design. Considering that the serious maldistribution observed in our prototype can result in a 13% capacity loss, it appears to be a small penalty to pay.

Two constraints must be applied to the evaporator coil configuration. First, the evaporator tubes must be positioned in such a manner that promotes water shedding. Second, the design must not exceed a sensible heat ratio of 0.75 at the capacity rating condition, in order to provide adequate comfort over the normal range of operating conditions. This places a practical upper limit on the fin temperature, and hence the evaporating temperature.

5.3.1.2 Condenser

A true minimum TEWI condenser could have wider tube spacing, and therefore lower charge, than the prototype that used fins and tubes that had been optimized for automotive applications. Again to minimize charge as well as heat transfer, the heat transfer surface area would ideally be configured in a single thin slab having large face area to minimize the fan power needed to deliver the air flow necessary for efficient operation..

Maldistribution in microchannel condensers will result from poor inlet header design and from gravitational effects. The latter can be eliminated by orienting the tubes for vertical downflow. To prevent reverse flow in the tubes, the pressure drop across the tubes must substantially exceed the dynamic pressure variations within the header. This may require using long tube lengths, possibly a serpentine design, between the headers.

5.3.2 Compressor and blower

Recent work at the ACRC by Andrade and Bullard (1999) describes in detail the benefits of optimizing system efficiency with the use of a variable speed compressor and evaporator blower. The compressor speed can be set to meet the total capacity requirement, while the blower speed may be reduced to adjust fin surface temperatures to meet the latent load. At high humidity conditions, longer compressor run-times and decreased evaporator fan speeds will lower the evaporator temperature to encourage water shedding, thus controlling indoor humidity. The decrease in system efficiency due to a lower evaporating temperature is offset by the lower power consumption of

the evaporator blower and compressor resulting in a positive increase in EER. Their analysis estimated that improvements in EER could be as high as 59% for R410A split-systems.

5.4 Charge minimization

The pie chart presented in Figure 3.1 shows that nearly 50% of the total system charge is located in the condenser. Originally, the prototype TEWI condenser was designed as a single pass heat exchanger. In this configuration, all of the condenser tubes filled with subcooled liquid exit into the 2.6ft long header. By re-circuiting the condenser to include multiple passes, less than 1/3 of the exit header would be filled with liquid, reducing the total charge in the header by 0.35 lbm. Removing the system instrumentation and redesigning the filter dryer could decrease the total charge by as much as 0.9 lbm. These improvements on the prototype do not effect the efficiency of the system and bring the total system charge to 4.7 lbm.

Chapter 6: Summary and Conclusions

A microchannel split-system air conditioner was tested to validate the system model. This system was the first prototype ever designed to utilize an R410A microchannel evaporator and condenser. Experimental results were compared with simulation runs to quantify performance of this 2.5-ton residential split system. Measured system capacity fell 13% below prediction for dry coil points and 18% below for wet coil points. Due to substantial maldistribution in both the evaporator and condenser coils, it was impossible to verify the applicability of Chang and Wang's air-side heat transfer correlation for either the evaporator or condenser. However, the extensive system instrumentation allowed for the maldistribution to be closely monitored providing insights into the design of microchannel heat exchangers.

For the condenser, better refrigerant flow distribution could be achieved by avoiding the V-coil configuration used for the prototype. Flat slabs would be ideal, with downflow probably preferable to upflow; vertical tubes are needed to facilitate condensate drainage and defrosting in heating mode. Ideally the header design should include multiple feeder tubes and if necessary, a mesh grid inside the condenser header to help control vortex generation that could result in backflow. Both headers should be designed to ensure that variations in dynamic pressures along the header are be much less than the pressure drop across the condenser tubes. Despite the maldistribution, the overall UA of the prototype condenser was so large that a mean capacity loss of only 2.8% was observed.

The evaporator maldistribution can be only prevented if every port has both identical inlet quality and mass flow rate. Since this is impossible to achieve with the current technology, it appears that pressure drop across the evaporator coil must be sacrificed to some extent in order to improve flow distribution. If the pressure drop is high enough, evaporator exit superheat temperature and the mass flow rate entering each port will be relatively insensitive to variations of pressure and inlet quality within the header. Increasing the pressure drop across the coil by 5 psi would theoretically result in a 2% capacity loss, compared to the mean evaporator capacity loss for observed for the maldistributed prototype coil was, which was 13% at dry conditions, and it increased to 19% at wet-coil conditions.

The experimental results reported here provide no reason to alter the initial design recommendations for the system. However, they do impose additional design constraints to ensure optimal performance of the microchannel evaporators and condensers. For a minimum TEWI system, compressor mass flow should be modulated to minimize temperature lift, microchannel heat exchangers should be used to reduce temperature differences across the evaporator and condenser without increasing charge, while relying on a variable-speed blower to control indoor humidity at minimal cost in EER. Charge could be further reduced by reducing port diameters, and by adding multiple passes to the condenser coil, to eliminate the large liquid-filled outlet header. Finally, minimum-TEWI heat exchangers should have the largest face area allowed within packaging constraints.

References

Andrade, M.A. and C.W. Bullard, "Controlling Indoor Humidity Using Variable Speed Compressors and Blowers", *University of Illinois at Urbana-Champaign*, ACRC TR 151, 1999

ASHRAE, "Method of Testing for Rating Room Air Conditioners and Packaged Terminal Air Conditioners." ANSI/ASHRAE Standard 16-1983, 1983.

Bridges, B.D. and C.W. Bullard, "Simulation of Room Air Conditioner Performance." *University of Illinois at Urbana-Champaign*, ACRC TR-79, 1995.

Chang, Y.J. and C.C. Wang, "A Generalized Heat Transfer Correlation for Louver Fin Geometry." *Int. J. Heat Mass Transfer*, vol. 40, no. 3, pp. 533-544, 1997.

Damasceno, G.D et al., "Performance of Heat Pump Reversing Valves and Comparison Through Characterizing Parameters" *ASHRAE Transactions*, vol. 94, no. 1, pp. 304-317, 1988.

Dobson, M.K. and J.C. Chato, "Condensation in Smooth Horizontal Tubes," *Journal of Heat Transfer*, 120:2, pp. 193-213, 1998.

Feller, S.D. and W.E. Dunn, "Design of the Outdoor Environmental Chamber of a Room Air Conditioner Test Facility." *University of Illinois at Urbana-Champaign*, ACRC TR-43, 1993.

Fischer, S.K. and C.K. Rice, "The Oak Ridge Heat Pump Models." *Oak Ridge National Laboratory*, ORNL/CON-90/R1, 1983.

Fleming, J.E. and W.E. Dunn, "Design of the Psychrometric Calorimeter Chamber of a Room Air Conditioner Test Facility." *University of Illinois at Urbana-Champaign*, ACRC TR-44, 1993.

Hahn, G.W. and C.W. Bullard, "Modeling Room Air Conditioner Performance." *University of Illinois at Urbana-Champaign*, ACRC TR-40, 1993.

Heun, M.K. and W.E. Dunn, "Principles of Refrigerant Circuiting with Application to Microchannel Condensers: Part I-Problem Formulation and the Effects of Port Diameter and Port Shape," *ASHRAE Transactions*, 102:2, pp. 373-381,1996.

Heun, M.K. and W.E. Dunn, "Principles of Refrigerant Circuiting with Application to Microchannel Condensers: Part II-The Pressure-Drop Effect and the Cross-Flow Heat Exchanger Effect," *ASHRAE Transactions*, 102:2, pp. 382-393, 1996.

Jensen, A.C. and W.E. Dunn, "Refrigerant-Side Instrumentation in Room Air Conditioners." *University of Illinois at Urbana-Champaign*, ACRC TR-101, 1996.

Kirkwood, A.C. and C.W. Bullard, "Modeling, Design, and Testing of a Microchannel Split-System Air Conditioner," *University of Illinois at Urbana-Champaign*, ACRC TR-149, 1999

Lalot, S. et al., "Flow Maldistribution in Heat Exchangers", *Applied Thermal Engineering,* 19, pp. 847-863, 1999.

Mullen, C.E. and C.W. Bullard, "Room Air Conditioner System Modeling." *University of Illinois at Urbana-Champaign*, ACRC TR-61, 1994.

O'Neal, D.L. and S.B. Penson, "An Analysis of Efficiency Improvements In Room Air Conditioners." *Texas A&M University*, ESL/88-04, 1988.

Peixoto, R. and C.W. Bullard, "A Design Model for Capillary Tube-Suction Line Heat Exchangers." *Proceedings of 1994 International Refrigeration Conference-Purdue University*, July, 1994.

Rugg, S.M. and W.E. Dunn, "Design, Testing, and Validation of a Room Air Conditioner Test Facility." *University of Illinois at Urbana-Champaign*, ACRC TR-59, 1994.

Sand, J.R., S.K. *et al.* "Energy and global warming impact of HFC refrigerants and emerging technologies." A report sponsored by the Alternative Fluorocarbons Environmental Acceptability Study (AFEAS) and the U.S. Department of Energy 1997.

de Souza, A.L. and M.M. Pimenta, "Prediction of Pressure Drop During Horizontal Two-Phase Flow of Pure and Mixed Refrigerants," *ASME Conf. Cavitation and Multiphase Flow*, S. Carolina, FED Vol. 210, pp. 161-71, 1995.

Sporlan Valve Company, *Refrigerant Distributors*, June Bulletin 20-10, 1975.

Wattelet, J.P., J.C. Chato, A.L. de Souza, and B.R. Christoffersen, "Evaporative Characteristics of R-12, R-134a, and MP-39 at Low Mass Fluxes," *ASHRAE Transactions*, 100:1, pp. 603-615, 1994.

Appendix A: Experimental Capacity Calculations

A.1 Measuring evaporator steady-state capacity

Three methods were available for measuring the steady-state capacity of the evaporator; the refrigerant-side energy balance, the air-side energy balance and the room power measurement. The evaporator capacity was calculated using all three methods and the most reliable method was chosen as the '$Q_{room\ measured}$' to be compared with the model results.

A.1.1 Evaporator capacity from room power measurements

The DSP power measurement system, discussed in Appendix D, was designed to measure up to 20 kW of power with an accuracy of 0.01%. The Room DSP system measures the total power, P_{room}, supplied to the furnace, furnace fan, humidifier tank heaters and the indoor room mixing fans. A separate watt transducer is also used to record the power supplied to the evaporator blower, P_{blower}. Both power measurement values are converted to work values (Btu/hr) by multiplying the reading by 3.414 Btu/W-hr. The resulting values are referred to as W_{room} and W_{blower}.

From the room energy balance, the total capacity of the room is calculated using equation A.1. The heat transfer due to condensate removal from the indoor room, $Q_{condensate}$, is calculated with equation A.2. Rugg and Dunn (1994) measured the heat leakage from the indoor room, determining the overall UA for the walls to be 7.8 Btu/hr-ºF. Using this value, the heat lost through the walls, Q_{walls}, can be calculated using equation A.3.

$$\dot{Q}_{room\_power} = \dot{W}_{room} + \dot{W}_{blower} - \dot{Q}_{condensate} - \dot{Q}_{walls} \tag{A.1}$$

with

$$\dot{Q}_{condensate} = \dot{m}_{condensate} \cdot Cp_{water}\left(212°F - T_{dewpoint}\right) \tag{A.2}$$

$$\dot{Q}_{walls} = UA_{walls}\left(T_{indoor} - T_{amb}\right) \tag{A.3}$$

A.1.2 Evaporator capacity from the air-side energy balance

An air-side energy balance requires accurate measurements of the inlet and exit air temperatures. The inlet to the blower housing was instrumented with a 4x4 square grid of Type-T air-side thermocouples and the exit with a 3x3 square grid of thermocouples. Numerous data points were taken at various fan speeds with all 25 thermocouples being recorded. From this data, four thermocouples at the inlet were selected that consistently matched the average inlet temperature within ±0.1ºF. Five thermocouples were selected for the exit, with the average of the five thermocouples also being within ±0.1ºF of the total average.

The Bryant fan discussed in section Appendix B, is a self-adjusting blower that supplies a constant volumetric flow rate within a range of static pressure in the air duct. Although the volumetric air flow rate was not measured for each point, the calibration data can be taken with confidence for dry coil points and used in an air-side energy balance.

The evaporator air-side energy balance was calculated using equation A.4. The inlet, T_{air_in}, and outlet, T_{air_out}, air temperatures are the averaged thermocouple readings. The property calls for the density, ρ_{air}, and specific

heat, Cp_{air}, use the outlet air temperature. The volumetric flow, V_{air}, is a constant value for each setting, obtained from the lower calibration data. The latent heat transfer, Q_{latent}, is calculated using equation A.5.

$$\dot{Q}_{air} = r_{air} \cdot 60 \cdot \dot{V}_{air} \cdot Cp_{air} \left(T_{air\_in} - T_{air\_out} \right) - \dot{W}_{blower} + \dot{Q}_{latent} + \dot{Q}_{condensate} \qquad \text{(A.4)}$$

$$\dot{Q}_{latent} = \dot{m}_{condensate} \cdot h_{fg} \qquad \text{(A.5)}$$

A.1.3 Evaporator capacity from the refrigerant-side energy balance

Five independent measurements are required to calculate the evaporator capacity from a refrigerant-side energy balance; two pressure measurements, two temperature measurements and the refrigerant mass flow rate, w. The calculation for the refrigerant side capacity, Q_{ref}, is presented as equation A.6.

The evaporator inlet enthalpy, $h_{ref\_evap\_in}$, is a function of the liquid line temperature and pressure. The liquid line pressure is measured with a 1000 psia (±1 psi accuracy) pressure transducer located downstream from the heat pump TXV valve. The temperature of the liquid line is recorded with an immersion thermocouple located 1 ft upstream of the evaporator TXV. The evaporator outlet enthalpy, $h_{ref\_evap\_out}$, is a function of the evaporator exit pressure and suction line temperature. The exit pressure is recorded with a 500 psia (±1 psi accuracy) and the suction line temperature is measured with an immersion thermocouple, 1.5ft downstream of the evaporator exit header. The low-noise immersion thermocouples have a ±0.5°F accuracy. A corliolis meter was installed on the liquid line to measure the mass flow rate within ±0.05 lbm/hr.

$$\dot{Q}_{ref} = \dot{w} \cdot \left(h_{ref\_evap\_out} - h_{ref\_evap\_in} \right) \qquad \text{(A.6)}$$

A.1.4 Comparison of evaporator capacity measurements

The evaporator capacity was calculated using all three methods described above. Due to the high accuracy of the room power measurements, the room power capacity was selected as the baseline for comparison. Figure A.1 shows the accuracy of the air-side energy balance. The two energy balances have excellent agreement with a mean error of 0.9% with a standard deviation of 2% for dry-coil operating conditions. The high fan speed capacity points have the worst agreement for the dry coil points. The new value selected for the high speed calibration volumetric flow rate (888 cfm) was about 1% higher than what we observed in the lab. For wet coil points, only measurements calculated from Q_{room} were available for the volumetric flow rate due to the calibration failing at high static pressures in the duct. Appendix B provides full details on the evaporator blower as well as the calculation for volumetric flow rate from the room power measurement.
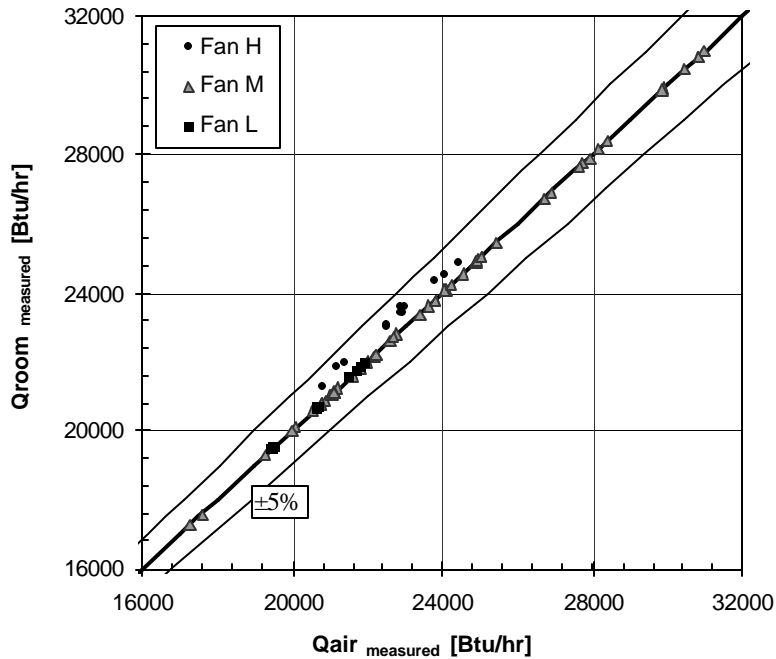
Figure A.1 Accuracy of the air-side energy balance for dry coil conditions

The agreement between the capacity calculated from the room power and the refrigerant-side energy balance was not as good. Figure A.2 shows that the mean error for the dry coil points was 7.5%, with a standard deviation of 2%. The wet coil points had a mean error of 20% and a standard deviation of 2.3%.

One possible source of in the refrigerant-side capacity calculation could be a result of an inaccurate suction line immersion thermocouple measurement. If the refrigerant is not fully superheated, liquid droplets could be hitting the immersion thermocouple, resulting in a reading that is lower than the true refrigerant temperature. This theory is supported by the large fluctuations (±8°F/min) in the thermocouple reading for most data points. The large amount of maldistribution observed in the evaporator provides further evidence of the existence of droplets of liquid refrigerant in the suction line.
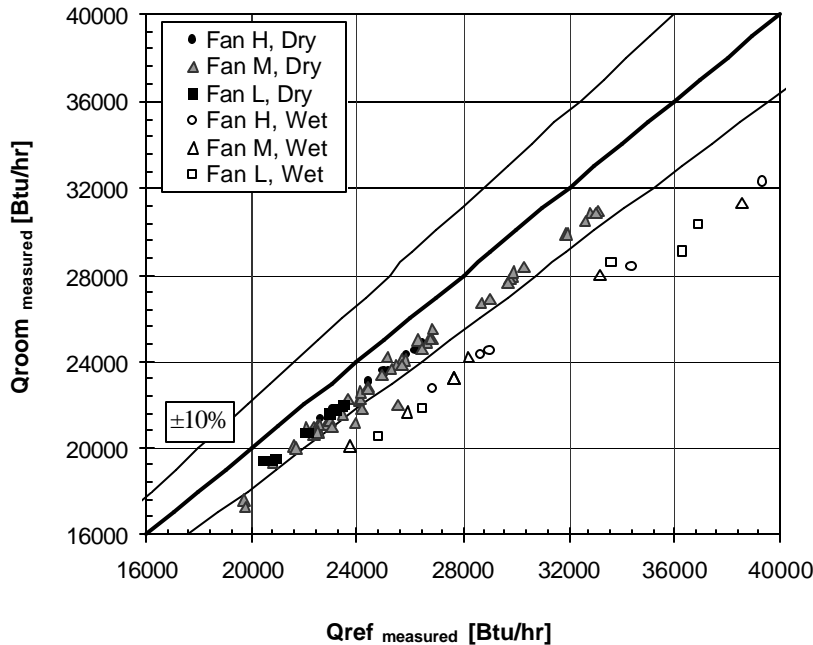
Figure A.2 Accuracy of refrigerant-side energy balance for dry and wet coil conditions

The suction line location is another possible cause for an inaccurate superheat measurement. After exiting the outlet header, the suction line is positioned directly in the center of evaporator exit air-flow path (see Figure 4.1). The heat transfer caused by the cool air blowing over the suction line could cause the refrigerant to de-superheat. However, calculations have shown that the heat transfer would not change the refrigerant temperature by more than 0.2°F

A.2 Measuring condenser steady-state capacity

Unlike the evaporator, only one method is available to calculate the condenser capacity, the refrigerant-side energy balance. The difficulty in determining the condenser capacity lies in the need to account for the additional heat transfer and pressure drops that occur between the instrumentation and the desired state points. When instrumenting the system, it was impossible to incorporate pressure taps directly across the condenser coil. The only plausible solution was for the reading to include both the pressure drop across the heat pump valve at the inlet and the pressure drop caused by the reverse flow through the TXV which was installed at the condenser exit (evaporator inlet duing heat pump operation). Fortunately, the pressure drop and heat transfer can be accounted for and the true refrigerant inlet and exit temperatures and pressures can be estimated.

A.2.1 Heat transfer and pressure drop through 4-way reversing valve

An Alco RV4F46 4-way brass reversing valve was incorporated into the system so that the unit can be run in both a/c and heat pump modes. The valve is located on the discharge line/suction line in the system and is slightly over-sized for our applications. The valve was designed for a 4 ton capacity R22 system which translates to 5 tons for R410A. Correlations from Damasceno *et al.* (1988) were used to account for the pressure drop and heat transfer through brass 4-way reversing valves. Damasceno *et al.* only provided loss coefficients for 2 ton and 6 ton

brass valves. Both coefficients were calculated and interpolation was used to obtain the correct values for a 4 ton valve.

The pressure loss through the valve can be accounted for using the characteristic parameters, $C_{p\_suction}$ and $C_{p\_discharge}$ defined in equations A.7a and b. The equations are used to calculate the condenser inlet pressure, P_{disc_out}. The experimental values used in the calculation are the mass flow rate, w, the absolute pressure transducer reading, $P_{evap\_out\_measured}$, the differential pressure transducer reading, $DP_{cond\_measured}$, and two immersion thermocouple readings, T_{disc_in}, and T_{suct_in}.

$$C_{P_{suction}} = r_{suction} \cdot \frac{\left(P_{suct\_in} - P_{suct\_out}\right)}{\dot{w}^2} \tag{A.7a}$$

$$C_{P_{discharge}} = r_{discharge} \cdot \frac{\left(P_{disc\_in} - P_{disc\_out}\right)}{\dot{w}^2} \tag{A.7b}$$

with:

$$r_{suct\_in} = f(T_{suct\_in}, P_{suct\_in}) \qquad\qquad r_{disc\_in} = f(T_{disc\_in}, P_{disc\_in})$$

$$P_{suct\_in} = P_{evap\_out\_measured} \qquad\qquad P_{disc\_in} = P_{cond\_out\_measured} + \Delta P_{cond\_measured}$$

$$C_{P_{suction}} = 0.000018 \; (2ton) \qquad\qquad C_{P_{discharge}} = 0.000041 \; (2ton)$$

$$C_{P_{suction}} = 0.000005 \; (6ton) \qquad\qquad C_{P_{discharge}} = 0.000005 \; (6ton)$$

The heat loss through the valve is accounted for using the heat transfer characteristic parameters defined in equations A.8a and b. The variables obtained from the data are mass flow rate, w, the average outdoor temperature, T_{amb}, the two immersion thermocouple readings for T_{suct_in} and T_{disc_in} and the pressures, P_{suct_in} and P_{disc_in}. The enthalpy function calls depend on the temperatures that are being solved for (T_{disc_out}, T_{suct_out}), so the set of equations must be solved simultaneously. The result for T_{disc_out} is used as the true condenser inlet temperature.

$$C_{H\_discharge} = \dot{w} \cdot \left[\frac{h_{disc\_in} - h_{disc\_out}}{\left(T_{disc\_in} - T_{amb}\right) - \left(T_{suct\_in} - T_{amb}\right)} \right] \tag{A.8a}$$

$$C_{H\_suction} = \dot{w} \cdot \left[\frac{h_{suct\_out} - h_{suct\_in}}{\left(T_{disc\_in} - T_{amb}\right) - \left(T_{suct\_in} - T_{amb}\right)} \right] \tag{A.8b}$$

with:

$$h_{disc\_in} = f(T_{disc\_in}, P_{disc\_in}) \qquad\qquad h_{disc\_out} = f(T_{disc\_out}, P_{disc\_out})$$

$$h_{suct\_in} = f(T_{suct\_in}, P_{suct\_in}) \qquad\qquad h_{suct\_out} = f(T_{suct\_out}, P_{suct\_out})$$

$$C_{H\_suction} = 0.0063 \cdot \dot{w} + 0.42 \; (2ton) \qquad C_{H\_discharge} = 0.0063 \cdot \dot{w} + 1.24 \; (2ton)$$

$$C_{H\_suction} = 0.0076 \cdot \dot{w} + 0.11 \; (6ton) \qquad C_{H\_discharge} = 0.0076 \cdot \dot{w} + 1.53 \; (6ton)$$

A.2.2 Pressure drop due to reverse flow through the heat pump TXV

Modine provided pressure drop information for reverse flow through the TXV for the standard test condition (45°F evaporating temperature and a capacity of 2.5 tons). This information, combined with mass flow rate data from the compressor map was used to develop equation A.9, an estimation for the pressure drop as a function of mass flow rate, w. The absolute pressure transducer reading is used for the measured pressure, $P_{cond\_out\_measured,}$ and the true exit pressure of the condenser is P_{cond_out}.

$$\Delta P_{distributor} = 4.2 \cdot \left(\frac{\dot{w}}{360} \right)^2 \tag{A.9}$$

with:

$$\Delta P_{distributor} = P_{cond\_out} - P_{cond\_out\_measured}$$

A.2.3 Condenser capacity calculation

The condenser capacity is a straightforward calculation once the correct inlet and exit state points have been defined. Equation A.10 calculates the condenser capacity using a refrigerant side energy balance. The mass flow rate, w, and condenser exit temperature, T_{cond_out}, are taken directly from experimental data. P_{cond_out}, P_{disc_out}, and T_{disc_out} are all calculated values using the equations listed in the previous two sections. The results of the condenser capacity prediction can be seen in Chapter 2, Fig. 2.4.

$$\dot{Q}_{condenser} = \dot{w} \cdot \left(h_{cond\_in} - h_{cond\_out} \right) \tag{A.10}$$

with:

$$h_{cond\_in} = f\left(T_{disc\_out}, P_{disc\_out} \right)$$

$$h_{cond\_out} = f\left(T_{cond\_out}, P_{cond\_out} \right)$$

Appendix B: Evaporator Blower and Compressor Analysis

B.1 Introduction

The accuracy of both the compressor map and the blower volumetric flow rate calibration is very important for the system analysis. The model relies on the compressor map to calculate mass flow rate and power consumption. The calibration values for the volumetric flow rates are considered constant for each respective setting and are set as parameters for all model runs. If either calibration is incorrect, it could have a dramatic effect on the model's predictions.

B.2 Validation of evaporator blower calibration

A Bryant FK4CNF003 fan was selected for the evaporator blower. Modine Mfg. Co. calibrated the blower inside the housing with the prototype evaporator coil in place. Three evaporator settings were selected from the calibration for our test matrix and they are listed in Table B.1.

Table B.1 Evaporator blower calibration data

Speed	Fan Setting	Volumetric Flow Rate [cfm]
L	Y1-24-NOM	626
M	Y1-36-NOM	796
H	Y1-42-HIGH	1015

To validate the calibration, the volumetric flow rate was calculated using equation B.1. Two independent measurements were used in the calculation, the measured room capacity, Q_{room}, and the air-side thermocouple readings from the inlet and exit of the evaporator blower. The measurement for Q_{room} has an accuracy of $\pm 0.05\%$ and the thermocouple averages have an accuracy of $\pm 1°F$

$$\dot{V} = \frac{\dot{Q}_{room\_measured} - \dot{Q}_{lat}}{r_{air} \cdot 60 \cdot Cp_{air}\left(T_{air\_in} - T_{air\_out}\right)} \tag{B.1}$$

Figure B.1 shows the accuracy of the calibration for dry coil points for the three selected fan speeds. The low fan setting (Y1-24-NOM) had the best agreement, with a standard deviation of 4 cfm and a mean error of 0.2%. The medium fan speed (Y1-36-NOM) had a standard deviation of 19 cfm with a mean error of 0.8%. Most of the outliers for the medium fan speed occurred when the evaporator temperature was below 32°F, or a slightly frosted coil condition.

The high fan speed (Y1-42-HI) had major discrepancies between the calibrated value and the average experimental value, with a standard deviation of 2.8 cfm and a mean error of 12%. Two possible explanations exist; either the Easy Select Board settings were misinterpreted during calibration or wires were connected incorrectly when installing the system in the lab. The calibration result for the Y1-42-NOM setting was 888 cfm, a value almost identical to the experimental average. Thus, 888 cfm was assumed to be the correct output for the high fan setting and was used for all high fan speed simulations.
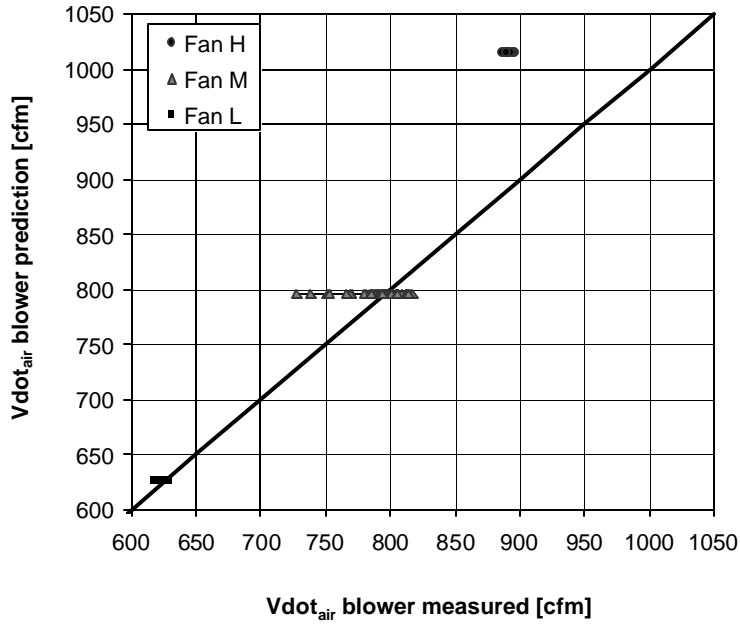
Figure B.1 Accuracy of evaporator blower calibration for dry coil conditions

High humidity conditions in the indoor room appear to have a negative effect on the pressure drop control mechanism in the blower. For all of the wet evaporator coil points, the measured volumetric flow rate differed significantly from the calibration data. The results are presented in Figure B.2. The low fan setting had a standard deviation of 54 cfm, with a mean error of 30%. The standard deviation for the medium fan speed was 110 cfm, with a mean error of 14%. The high fan setting had a standard deviation of 174 cfm and a mean error of 16%.
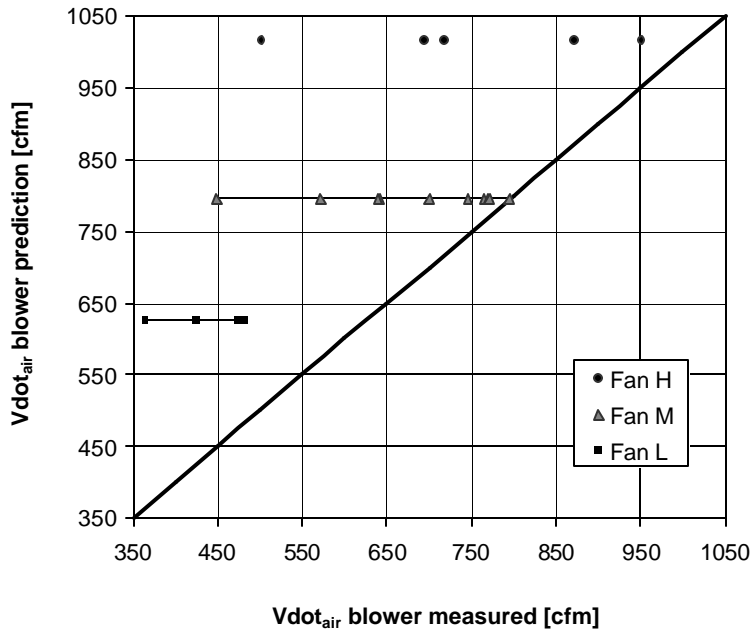
Figure B.2 Accuracy of blower calibration for high humidity conditions

Discussions with Carrier Corp. revealed that each fan speed/torque controller was calibrated for a specific Bryant evaporator coil (FK4CF003, 1999). The motor is also limited to operating in a specified range of static pressures in the duct. If the static pressure becomes too large, the fan motor cannot supply enough torque to maintain a constant air-flow rate. This could explain the large deviations from Modine Mfg. Co. calibration data for our wet coil points. While pressure drop across the duct was not measured, it can be assumed that it was high for the high capacity/wet coil points. Therefore, Modine's dry coil calibration still holds for the dry coil points, but an alternative measurement of volumetric flow rate is required for the high static-pressure/wet-coil points.

The volumetric flow rates were therefore calculated by matching the room capacity with the air-side energy balance for the wet-coil operating conditions. For dry-coil conditions, the volumetric flow rate input into the model is taken from the calibration data.

B.3 Compressor map validation

B.3.1 Power prediction

A biquadratic curve fit of the compressor map data resulted in a function that calculates the compressor power as a function of the evaporating and condensing temperatures. This function is used in the model to calculate the compressor power. In the lab, the RAC DSP measurement system described in Appendix D, measures the total power drawn by the compressor and the evaporator blower with an accuracy of 0.01%. A separate measurement of the evaporator blower power is obtained with a watt transducer. The measured compressor power is calculated by subtracting the watt transducer reading from the DSP measurement. Figure B.3 shows good agreement between the curve fit predictions and the measured power. The system consistently drew more power than the map predicted having a mean error of 1.9% for dry coil conditions and 4.2% for wet coil conditions. However, as shown in Figure B.3, the relationship with wet/dry is merely a coincidence. The magnitude of error varies monotonically with power.

B.3.2 Mass flow rate prediction

A biquadratic curve fit was also generated from the mass flow data in the compressor map. The resulting function calculated the mass flow rate for the system as a function of the evaporating and condensing temperatures. The agreement between the function predictions and the data was excellent for both the wet and dry points. Figure B.4 shows that all the results fell within 5% of the prediction with a mean error of 0.3% for dry coil points and 2.2% for wet coil points.
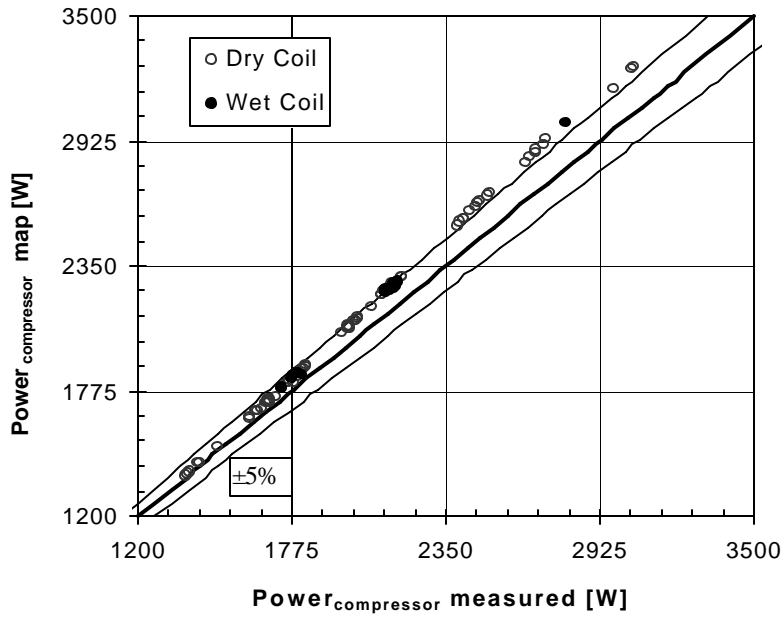
Figure B.3 Accuracy of the compressor map power curve fit
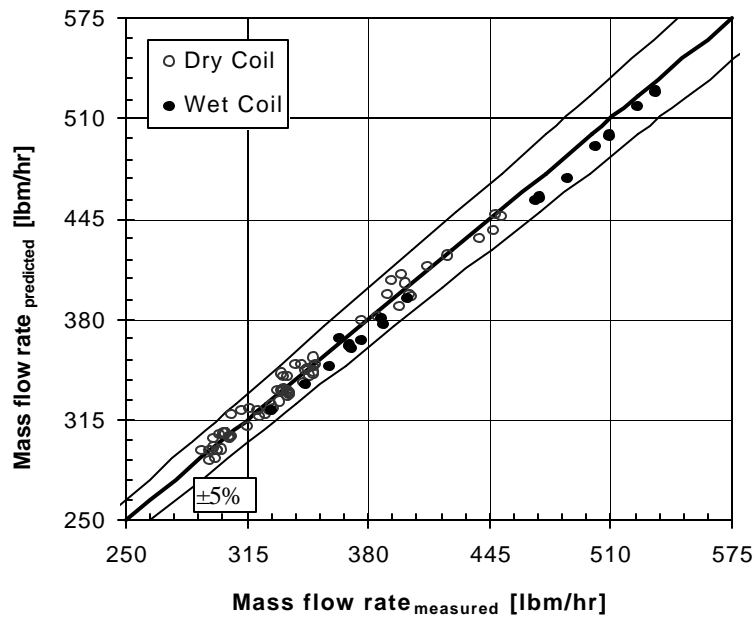
Figure B.4 Accuracy of the compressor map predictions for mass flow rate

Appendix C: Water Removal Rate Analysis

C.1 Introduction

The error in the evaporator capacity prediction increased by 7% for wet coil data. At the ARI standard rating condition, the latent capacity only accounts for 25% of the total evaporator capacity. Over our range of test conditions, simulation runs suggest that the latent capacity could account for as much as 40% of the total capacity. Therefore, the accuracy of the prediction for water removal rate becomes critical to the accuracy total capacity predictions.

Two sources of error are investigated in this appendix: the capacity limitations of the humidity control in the test chamber; and the modeling assumption that no water shedding occurs in the superheated area of the evaporator.

C.2 Accuracy of the model

The evaporator submodel was run with the inlet temperature, enthalpy and mass flow rate set. The indoor room conditions (relative humidity, T_{air}) and the volumetric air flow rate were also input in the model. The air flow rate was calculated from the air-side energy balance (Appendix A), using the measured value for the water removal rate. The model calculates total capacity through a refrigerant-side energy balance, rate equation and an air-side energy balance. Using the calculated volumetric flow rate may skew the simulation results in favor of the measured values for water removal rate, but the magnitude of this effect cannot be estimated in the absence of additional data. Figure C.1 shows the mean error in the water removal rate prediction was 6%, with a standard deviation of 14%.
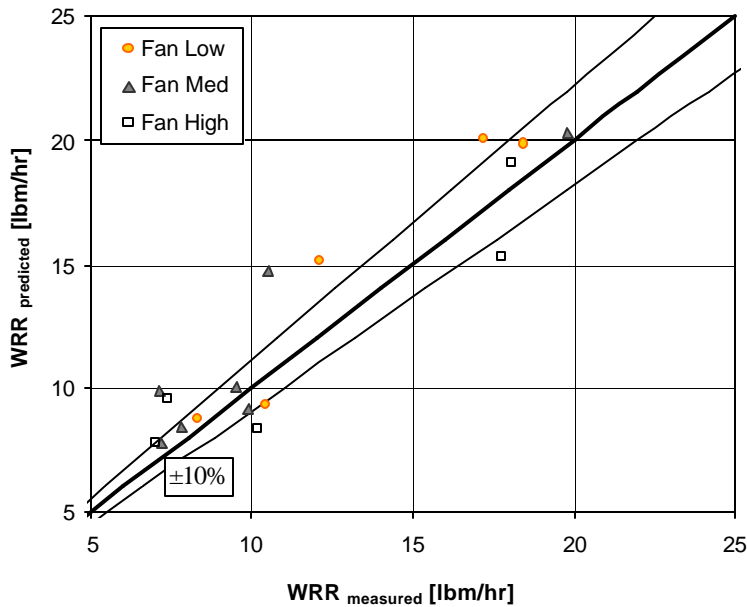
Figure C.1 Accuracy of the water removal rate prediction

C.3 Humidity control limitations

The humidity control system was originally designed by Rugg and Dunn (1994) to handle water removal rates from 0 to 27 lbm/hr, or a maximum system capacity of 8.8 kW. It consists of a large 50 gallon tank with four 2 kW heaters inside to heat the water to the boiling point. Pipes extend out from the tank to uniformly feed steam to each side of the room. Tape heaters were installed along the exit 'arms' of the humidifier to prevent re-condensation of saturated steam after leaving the humidifier. These tape heaters are set to maintain a constant 250 °F superheated exit.

Before the installation of the split system, the highest water removal rates tested were 6 lbm/hr and the humidifier worked well. The high capacity points for our test matrix have much high water removal rates, typically on the order of 20 lbm/hr. When water is leaving the humidifier this quickly, it may re-condense in the arms of the humidifier if the tape heaters cannot sufficiently heat the large quantities of water or, droplets may enter the exit pipes due to vigorous boiling in the tank. If any water leaves the humidifier in a liquid state, it may accumulate on the floor. Since the evaporator's water removal rate is calculated from the load cell reading of the tank's weight, any the water leaves as liquid and accumulates in the environmental chamber will be incorrectly attributed to the water removal rate of the evaporator.

Since the indoor chamber was sealed during the tests, and the problem was not anticipated, it was impossible to confirm the hypothesis by direct observation. However, the experimental data tends to support this hypothesis. First, for high water removal rates, the tape heater temperatures fluctuated between 215-250°F, while for low water removal rates (<10 lbm/hr) the heaters maintained a constant reading of 250 °F. Second, the water removal rate prediction improved markedly for high water removal rates (> 15 lbm/hr). Typically, the model overpredicted the water removal rate by 15%, but at the high water removal rates, the prediction fell within 5%. If the water removal measurement was too high because liquid accumulation in the chamber, it would explain the better agreement at high water removal rate points.

C.4 Modeling water shedding from the superheated area

The next step was to investigate the accuracy of the predicted water removal rate. Currently, the model does not account for water shedding from the superheated area of the condenser. In conventional R22 systems, this assumption introduces minimal error because the fin temperature in the superheated area is higher than the dew point temperature. Since superheated R410A has better heat transfer properties, the surface temperatures of the superheated region calculated in the model were checked to see if water shedding could occur.

The model's predictions for the surface temperatures provided some qualitative insights. While it is not possible to provide any conclusive information about the water shedding in the superheated region, trends can be commented on. Evaporator simulations using experimental data as inputs, show that up to 45% of the superheated area could be shedding water, albeit at far lower rates than the two-phase region because the driving potential is smaller. The most likely cause of error in the prediction of water removal rate is maldistribution, which alters substantially the relative sizes of the wet and dry zones, and the temperatures of the fin surface. More detailed investigations should be deferred until flow distribution is improved.

Appendix D: Power Measurement System Documentation

D.1 Introduction

Accurate system capacity measurements require two independent power measurements. The first measurement is of the power supplied to operate the system, which includes the compressor motor and the evaporator blower. The measurement range for the system power is ~1-5 kW / 0-20 A. The second measurement is of the total power supplied to the indoor room to match the evaporator's capacity. The room power measurement includes the furnace, furnace fan, humidifier heaters and the mixing fans. The room power ranges between 3-20 kW / 5-40 A. ASHRAE standards require that power measurement for split systems be accurate within ±0.05% full scale (FS).

The strict accuracy requirements led to the purchase of two digital signal processor (DSP), boards custom designed and built by Innovative Devices, Inc. The boards were selected over commonly used power measurement systems such as watt transducers for their high accuracy, ±0.01% FS and logic capabilities that allowed for transient power measurements. The latter feature is very important because the room power measurement includes devices such as the furnace and humidifier that cycle on and off during steady-state operation. If a watt transducer were used to measure transient data, over 200 samples would be required every second to obtain the same accuracy.

The power measurement systems discussed here are strictly single-phase; therefore the three-phase power supplied to the condenser fan could not be measured. For model simulations, the condenser fan power was estimated using data from a comparable fan.

D.2 Power measurement system components

Each component in the power measurement system is described briefly below. The intent of this appendix is to provide a reference to aid in the troubleshooting of the DSP systems. Figure D.1 shows an overview of the DSP setup as it exists in the lab.
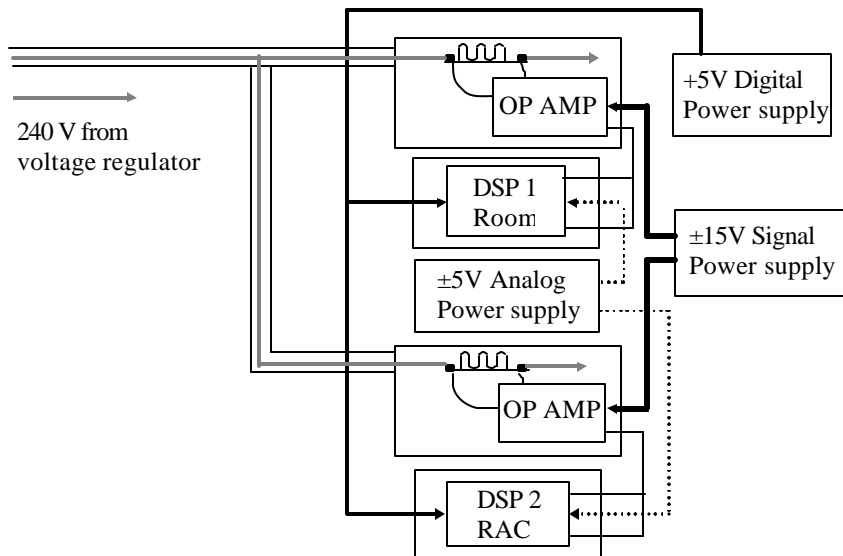
Figure D.1 Power measurement device flow schematic

48

D.2.1 Electronic line voltage regulator

       The voltage supplied to the building where the laboratory is located is know to vary ±10% or more. This variable voltage supply could lead to inaccurate measurements. To ensure that the rooms were receiving a constant 240V, a Series 900 Line Voltage Regulator (single-phase, 60 Hz) was purchased from Controlled Power Company (S/N 9/2-6-8659-93, M/N 5CGX-10X-9/2-I).

D.2.2 Operational amplifiers

       A separate op-amp circuit board was built for each DSP board that houses a voltage and current op-amp. The op-amp boards are positioned inside small metal boxes and placed inside the live 240V line box above each DSP board. The op-amps are used to condition the voltage and current signals that are supplied as inputs to the DSP boards. The voltage op-amp has a gain (Vout/Vin) of 5. The current op-amp gain is -0.006. Both op-amp units are powered by the same ±15 VDC power supply. The op-amp units for DSP1 and DSP2 are identical to one another. Figure D.2 presents the schematic for the op-amp units.
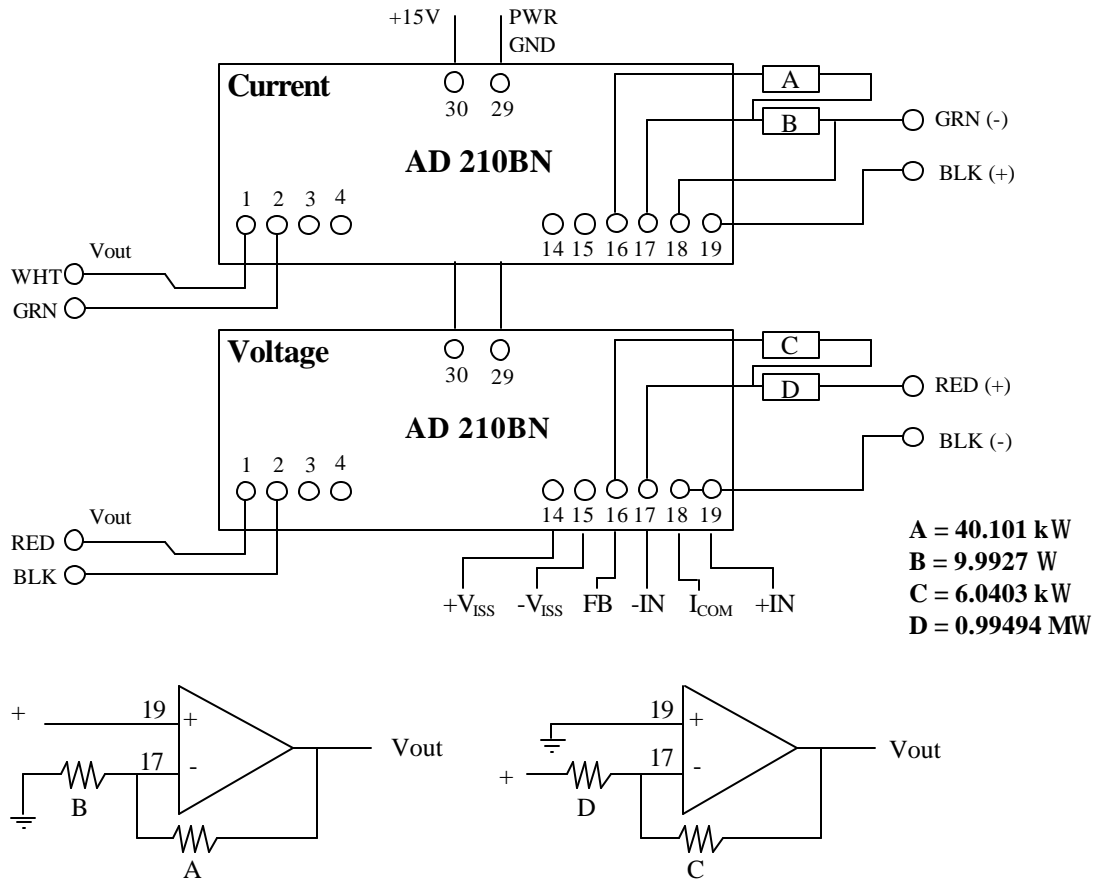
Figure D.2 Current and voltage operational amplifiers

D.2.3 Resistance shunts

       Empro resistance shunts are incorporated into the system to create a minimal resistance over which the current and voltage op-amp inputs could be connected so that the signal could be divided across the appropriate op-amp. The shunts were carefully selected to ensure that they were properly sized to cover the wide range of voltages

and current drawn by both systems. The shunt is connected directly after the 240V input coming from the voltage regulator for each DSP configuration. For DSP 1, the shunt resistance is 0.00344O. For DSP 2, The shunt resistance is 0.01018 Ω. The connections between the op-amps and the shunt are listed in Table D.1.

240V from
voltage regulator

240 V to room

Figure D.3 Resistance shunt

Table D.1 Shunt connections

Op-Amp Pin Connection	Shunt Location
Current 18: Green (-)	Right side of shunt (-IN)
Current 19: Black (+)	Left side of shunt (+IN)
Voltage 17: Red (+)	240V line (-IN)
Voltage 19: Black (-)	Right side of shunt (I_{COM})

D.2.4 DC power supplies

Three power supplies are necessary to operate the power measurement system. As mentioned previously, a ±15V DC power supply is necessary to excite the op-amps. To provide power to both the analog and digital inputs on the DSP boards, two different +5V power supplies are necessary. An attempt was made to power both the digital and analog inputs from the same ±5V DC power supply, but that resulted in damage to the DSP board. Therefore, separate +5V DC power supplies are connected to the analog and digital inputs of the DSP board. The positive lead to the digital input connector should be located in pin D20, the negative lead in pin D19 (see Figure D.4a). The analog side of both DSP boards is powered using the 3-pin connection, centrally located on the right-most side of the board (see figure D.4b).
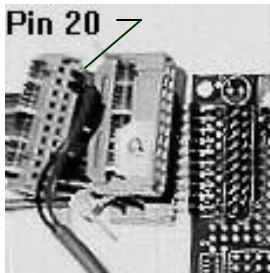
Figure D.4a Digital power connection
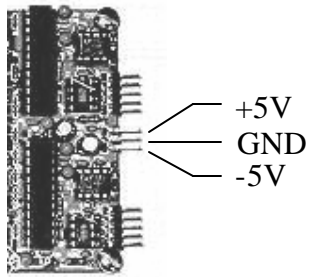
Figure D.4b Analog power connection
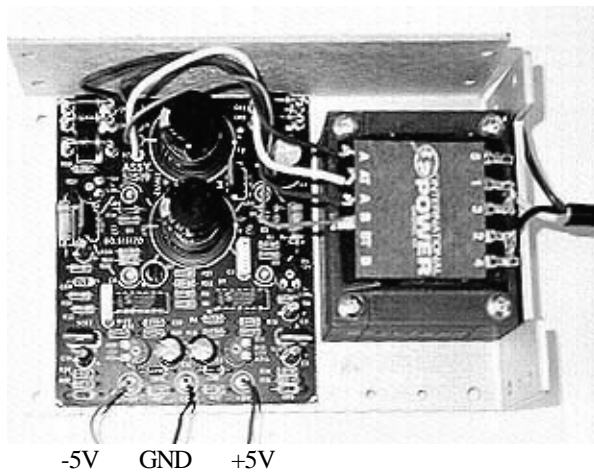
Figure D.5 International Power +/-5V, 3AMP power supply

D.2.5 DSP boards

The two DSP boards, designed by Innovative Devices, Inc. are identical in configuration. DSP1 continuously measures the room power signal and outputs the integrated signal every 60 seconds. The second board, DSP2, measures the compressor power and evaporator blower power continuously, outputting the integrated averages in 5 and 60 second intervals. The board configuration is shown in Figure D.6.

A	Digital power input
B	ADSP-2101, A/D converter
C	AD7869JN, 14Bit analog I/O chip
D	LTC1063 low pass filter
E	Analog I/O: 5sec
F	Analog power input
G	Analog I/O: 60sec
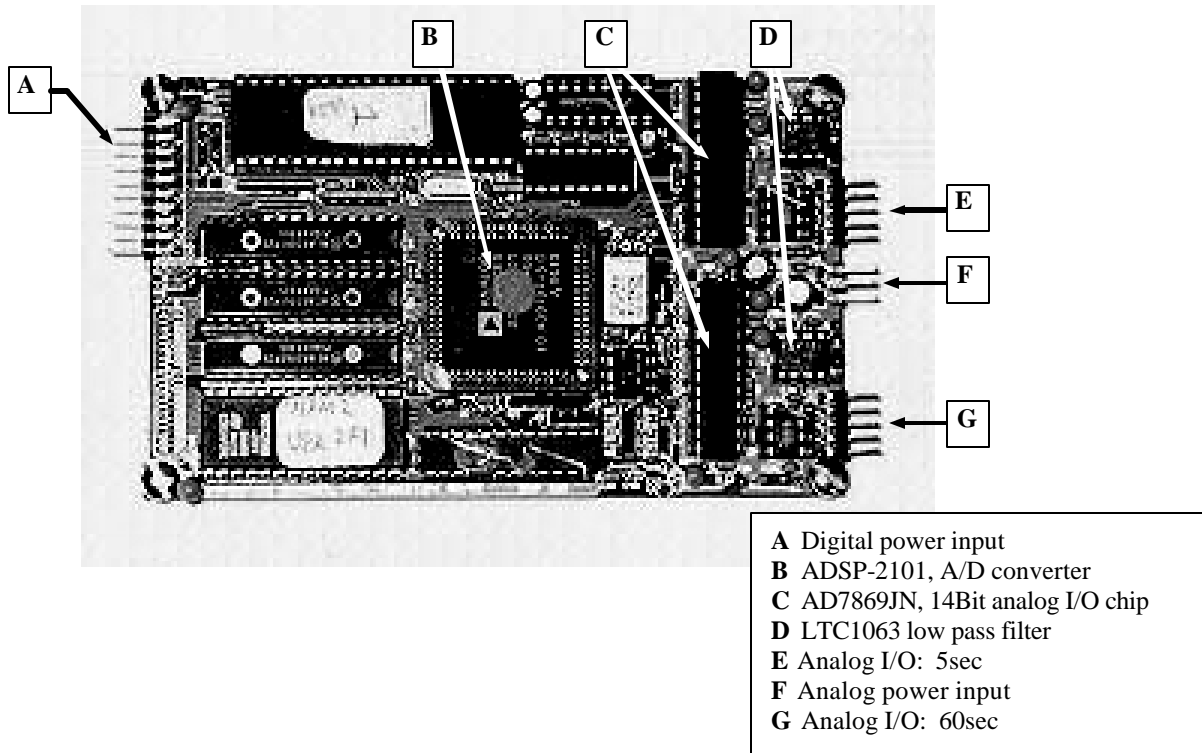
Figure D.6 DSP board layout
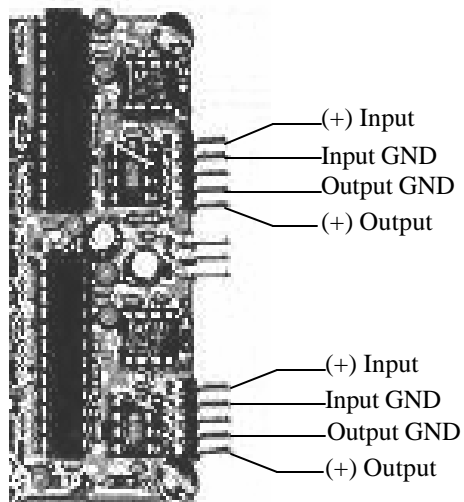
Figure D.7 DSP signal input connections

D.2.6 DSP daughter boards

Each DSP board has a corresponding daughter board that was originally located directly behind each DSP board. It was determined that the daughter board is not necessary for the DSP boards to work. However, if the boards were to be reconnected, the connection to the daughter board is rather simple. The digital power input connection is bridged across the daughter board.
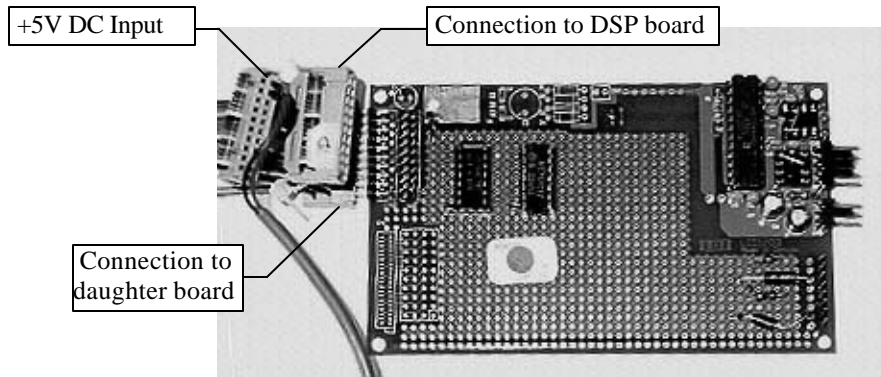
Figure D.8 Daughter board

D.3 Calibration of system components

D.3.1 Op-amp calibration

To test the op-amp signal output, the op-amps were powered using a +15V portable power supply. Referencing the schematic in Figure D.1, input voltages (AC) were placed across pins 17 and 19. A Fluke 5100B Calibrator was used to supply input voltages ranging from -400V to +400V,with increments of 10 V to each voltage op-amp. The voltage output across pins 1 and 2 was read using a HP multimeter with six-digit accuracy. After allowing some time for the op-amps to warm-up, over 80 readings were recorded for each op-amp. Data was recorded in a similar manner for the current op-amps, however, the voltage input ranged from -400 mV to +400 mV.

From the calibration data, the linear relationship between V_{out} and V_{in} can be determined. The slope of the linear solution is the gain of the op-amp. The calibration results are presented in Table D.2.

Table D.2 Calibration results for all op-amps

Op-amp	Calibration equation	RMS error
DSP1 Voltage	$V_{out} [V]= 7.694946e\text{-}3 - 6.148812e\text{-}3*V_{in}$	$3x10^{-3}$ V
DSP2 Voltage	$V_{out} [V]= 3.268392e\text{-}3 - 6.048149e\text{-}3*V_{in}$	$3x10^{-3}$ V
DSP1 Current	$V_{out} [V]= -3.852359e\text{-}3 + 5.041255*V_{in}$	$1x10^{-4}$ V
DSP2 Current	$V_{out} [V]= -5.406154e\text{-}3 + 5.023881*V_{in}$	$3x10^{-4}$ V

D.3.2 DSP board calibration

The DSP boards were calibrated using a HP waveform generator as the input signal, and bench power supplies for the analog and digital inputs. The waveform generator supplied high-Z impedance sine waves that ranged from 1 VPP to 5 VPP to both the 5 sec and 60 sec signal input locations on the DSP board. The output values were read with a HP 6-digit multimeter every two minutes to ensure the true integrated average was recorded. The input signal was supplied in 0.2 VPP increments. The resulting calibration equations are presented in Table D.3.

Table D.3 Calibration results for all DSP outputs

DSP output	Calibration equation
DSP1 5 sec output	$V_5 = -1.576577e\text{-}3 + 1.001867*V_{current}*V_{voltage}$
DSP1 60 sec output	$V_{60}= -1.348322e\text{-}5 + 1.001889*V_{current}*V_{voltage}$

DSP2 5 sec output	$V_5 = -5.056315e\text{-}4 + 1.001396*V_{current}*V_{voltage}$
DSP2 60 sec output	$V_{60} = -4.715298e\text{-}5 + 1.000790*V_{current}*V_{voltage}$

D.3.3 Shunt calibration

      To calibrate the resistance shunts, a power source that could supply both a large voltage and current was required. A Tenma power supply was used that could supply up to 40V and 10 A. Four-wire resistance readings were taken with a HP multimeter (6 digit) for load and no-load conditions. The load was generated by connecting a series of resistors across the shunt. The resistances of the shunts were determined to be 0.0034O for DSP1, and 0.0102O for DSP2.

D.4 Calibration equations and coefficients

D.4.1 Electrical power

$$E = \frac{1}{T}\int_0^T V(t)i(t)dt$$

where   E = electrical power [W],
                                              T = integration period [s],
                                            V(t) = instantaneous voltage [V],
and   i(t) = instantaneous current [A].

D.4.2 Ohm's law for the shunt

$$V_{shunt}(t) = i(t) \cdot R_{shunt}$$

where $V_{shunt}(t)$ = voltage across the shunt [V],

and R_{shunt} = shunt resistance [Ω].

D.4.3 Isolation amplifiers

$$V_{voltage}(t) = A_V . V(t)$$

and

$$V_{current}(t) = A_i . V_{shunt}(t)$$

where $V_{voltage}(t)$=output of voltage isolation amplifier [V],

                      $V_{current}(t)$=output of current isolation amplifier [V],

                      A_V = gain of voltage amplifier [–],

and A_i = gain of current amplifier [–].

D.4.4 DSP multipliers

$$\overline{V}_T = \frac{A_T}{T} \int_0^T V_{voltage}(t)\, V_{current}(t)\, dt + B_T = \quad A_T \cdot \overline{V_{voltage} \cdot V_{current}} + B_T$$

where $\overline{V}_T$ = multiplier output [V],

                      T = integration time [s] (5 s or 60 s),

                      A_T = multiplier gain for integration time T,

and B_T = multiplier offset for integration time T.

D.4.5 Composite form

$$E = a_T \overline{V}_T + b_T$$

where $a_T = \dfrac{1}{A_T A_V A_i R_{shunt}}$

and $b_T = \dfrac{-B_T}{A_T A_V A_i R_{shunt}}$.

D.4.6 Calibration coefficients

Table D.4 Calibration coefficients

Location	R_{shunt}	A_V	A_i	A_5	B_5	A_{60}	B_{60}
ROOM	0.00344	6.14881E-03	5.041255	1.001867	-1.56577E-03	1.001889	-1.34832E-05
RAC	0.01018	6.04815E-03	5.023881	1.001396	-5.05632E-04	1.000790	-4.71523E-05

Location	a_5	b_5	a_{60}	b_{60}
ROOM	1.001867	-1.56577E-03	1.001889	-1.34832E-05
RAC	1.001396	-5.05632E-04	1.000790	-4.71523E-05

Appendix E: Summary of Evaporator Maldistribution Data

E.1 Evaporator maldistribution data

Table E.1 presents all of the thermocouple readings along the exit tubes of the evaporator coil. The units are as follows: mass flow rate, w [lbm/hr], indoor room temperature, *Tair in* [F], and relative humidity, *RH* [-]. A complete list of the test conditions that correspond to the test number is presented in Appendix F. Following the tables are the graphs for all of the data points, referenced by point number.

Table E.1 Maldistribution data for evaporator coil

Test	1	2	3	4	5	6	7	8	9	10	11	12
Fan	M	M	M	M	M	M	M	M	M	M	M	M
RH	0.25	0.25	0.27	0.27	0.27	0.29	0.29	0.33	0.33	0.21	0.21	0.23
Tair in	70	70	70	70	70	70	70	69	70	82	83	82
w	298	296	302	299	299	295	298	297	301	329	327	336
1e	62	63	62	62	62	62	61	61	61	74	75	74
3e	54	54	52	51	51	48	47	46	47	65	66	64
5e	38	37	37	37	37	38	38	40	40	43	43	44
7e	44	41	50	51	51	53	52	52	51	49	49	58
9e	48	48	50	52	52	55	55	50	48	55	57	53
11e	46	47	51	53	54	55	55	43	42	59	61	61
13e	40	40	45	46	48	49	49	41	42	59	61	62
15e	36	35	37	37	37	38	38	40	40	45	46	52
17e	39	38	41	40	40	40	40	46	46	53	52	58
19e	38	37	38	38	38	40	39	43	44	45	44	46
21e	37	36	36	37	36	38	38	44	45	41	41	43
23e	48	48	46	48	46	52	51	58	58	48	46	46
25e	51	51	48	50	48	54	54	54	53	60	59	46
27e	48	49	45	53	51	62	60	59	60	68	68	65
29e	55	56	55	58	58	64	64	55	58	75	76	74
31e	62	62	62	64	64	66	66	59	61	79	79	78
33e	65	66	66	66	66	67	67	64	65	80	80	80
35e	67	67	68	67	67	68	68	66	67	81	81	81
37e	68	68	68	68	68	69	68	67	68	81	81	81
39e	68	68	68	68	68	69	68	68	68	81	81	81

Table E.1 Maldistribution data for evaporator coil (continued)

Test	13	14	15	16	17	18	19	20	21	22	23	24
Fan	M	L	L	L	M	M	H	H	H	M	L	L
RH	0.25	0.19	0.19	0.19	0.24	0.23	0.26	0.26	0.25	0.24	0.20	0.21
Tair in	83	83	83	82	83	83	82	83	83	83	83	83
w	345	306	306	307	337	337	349	350	351	334	303	303
1e	71	72	72	72	74	74	75	76	75	73	71	70
3e	56	61	61	61	64	64	66	65	66	62	59	56
5e	45	42	43	42	45	45	47	48	47	47	53	44
7e	61	60	61	60	61	57	65	65	62	67	67	64
9e	55	61	62	60	58	49	64	64	55	69	69	67
11e	58	62	62	62	61	59	67	67	63	64	65	64
13e	61	57	56	58	60	59	65	64	62	57	52	52
15e	56	41	41	42	46	46	49	49	48	46	41	41
17e	63	49	47	50	56	56	58	56	57	49	43	44
19e	49	41	42	41	46	46	48	48	48	46	43	43
21e	44	39	39	38	44	43	45	46	45	44	40	41
23e	54	41	45	40	47	51	47	49	50	58	61	62
25e	48	53	57	51	48	59	49	56	60	68	70	70
27e	56	66	69	64	67	69	69	71	72	76	76	76
29e	60	73	75	72	75	76	77	77	78	79	78	78
31e	72	77	77	76	79	79	79	80	80	80	78	78
33e	77	79	79	79	80	80	81	81	81	81	79	79
35e	79	80	80	79	81	81	81	82	82	81	79	79
37e	80	80	80	80	81	81	81	82	82	81	80	79
39e	80	80	80	80	81	81	81	82	82	81	80	79

Table E.1 Maldistribution data for evaporator coil (continued)

Test	25	26	27	28	29	30	31	32	33	34	35	36
Fan	L	M	M	H	H	H	M	L	L	L	M	M
RH	0.20	0.25	0.24	0.28	0.28	0.27	0.28	0.23	0.24	0.23	0.29	0.27
Tair in	83	83	83	83	83	83	83	83	82	83	83	83
w	304	332	335	350	347	351	335	312	307	316	334	337
1e	71	73	73	75	75	75	73	69	69	70	73	74
3e	60	62	61	63	64	64	62	55	54	56	61	63
5e	54	47	47	48	49	48	53	45	45	45	51	53
7e	67	67	67	67	68	67	71	65	64	66	70	71
9e	69	68	69	68	69	69	74	70	68	70	74	75
11e	65	63	64	65	65	66	73	67	65	68	73	74
13e	51	57	57	64	61	65	67	58	58	60	67	68
15e	41	46	46	49	49	50	48	44	45	44	49	48
17e	43	50	49	54	52	56	47	45	47	45	48	47
19e	42	47	46	49	49	49	49	46	46	46	50	49
21e	40	45	44	47	47	46	49	45	45	44	50	48
23e	59	60	57	51	58	47	70	64	64	63	70	68
25e	70	70	68	62	68	57	73	69	68	69	72	74
27e	76	77	76	73	76	72	77	74	74	74	76	77
29e	78	79	79	78	79	78	78	75	76	75	76	78
31e	79	80	80	80	80	80	77	76	76	76	76	78
33e	79	81	80	81	81	81	78	77	77	77	77	79
35e	80	81	81	81	81	81	79	77	77	78	78	80
37e	80	81	81	82	82	81	80	79	78	79	80	81
39e	80	81	81	81	81	81	80	79	79	80	80	81

Table E.1 Maldistribution data for evaporator coil (continued)

Test	37	38	39	40	41	42	43	44	45	46	47	48
Fan	H	H	H	M	M	M	M	M	M	M	M	M
RH	0.30	0.31	0.30	0.20	0.21	0.20	0.23	0.23	0.23	0.23	0.18	0.19
Tair in	83	82	83	95	95	95	95	95	97	98	105	105
w	345	341	350	386	397	376	403	403	391	400	412	423
1e	75	75	75	84	83	84	80	80	87	88	95	94
3e	66	65	66	74	67	74	61	60	77	79	88	84
5e	59	57	58	62	55	64	55	54	71	74	76	70
7e	73	72	73	62	58	65	64	62	84	86	74	67
9e	77	76	77	53	52	55	57	55	88	89	71	61
11e	76	75	76	52	53	57	66	66	88	89	71	60
13e	70	69	71	54	61	60	76	76	82	83	66	63
15e	50	50	53	52	54	55	63	63	60	60	61	60
17e	49	49	49	55	59	58	68	68	56	56	68	64
19e	50	51	50	59	59	62	60	60	58	59	72	68
21e	50	51	49	66	65	68	64	64	55	56	77	75
23e	70	71	67	81	77	82	72	72	70	72	82	86
25e	75	75	72	84	77	85	56	56	67	69	69	80
27e	78	78	77	84	77	84	56	56	85	86	71	85
29e	79	79	78	82	74	82	55	54	89	91	73	85
31e	78	78	78	84	82	85	79	78	90	92	90	92
33e	79	79	79	89	88	89	87	87	92	93	97	98
35e	80	79	80	91	90	91	89	89	93	94	100	100
37e	81	80	81	92	92	92	91	91	94	95	102	102
39e	81	80	81	92	92	92	92	92	94	95	102	102

Table E.1 Maldistribution data for evaporator coil (continued)

Test	49	50	51	52	53	55	56	57	58	59	60	61
Fan	M	M	M	M	M	H	L	M	H	M	M	M
RH	0.17	0.21	0.20	0.22	0.22	0.28	0.19	0.21	0.28	0.23	0.27	0.23
Tair in	105	105	105	105	105	83	83	82	83	83	72	80
w	398	448	440	448	451	352	306	325	348	338	291	328
1e	96	94	93	92	93	75	72	74	75	74	66	71
3e	90	82	81	76	78	64	61	65	64	64	61	61
5e	82	71	69	64	64	48	41	43	49	45	58	59
7e	80	72	68	69	69	66	58	49	68	60	66	69
9e	78	64	62	64	65	67	58	57	69	56	68	71
11e	76	62	61	63	63	65	61	60	65	61	67	71
13e	68	67	63	70	74	65	57	60	62	60	62	69
15e	62	63	61	65	65	51	43	46	49	47	44	58
17e	70	66	66	66	67	56	50	51	53	56	41	50
19e	77	66	68	69	67	49	41	44	49	46	40	44
21e	81	69	74	76	71	47	38	40	48	43	38	41
23e	88	79	85	88	83	48	39	46	58	47	54	47
25e	83	65	76	86	70	59	50	59	68	49	61	44
27e	83	67	79	85	80	72	64	67	76	67	67	55
29e	85	69	78	82	83	78	72	75	79	75	69	66
31e	93	88	90	90	92	80	76	78	80	79	70	73
33e	98	96	97	96	97	81	79	80	81	80	70	76
35e	101	99	100	98	99	81	80	80	82	81	71	77
37e	102	101	101	100	101	82	80	81	82	81	71	78
39e	102	101	101	101	101	81	80	81	82	81	71	78

Table E.1 Maldistribution data for evaporator coil (continued)

Test	62	65	66	67	68	69	70	71	75	76	77	78
Fan	M	M	M	M	M	M	M	M	M	M	L	H
RH	0.17	0.26	0.22	0.22	0.22	0.25	0.25	0.23	0.51	0.52	0.52	0.52
Tair in	105	80	81	83	83	80	80	80	80	80	80	80
w	392	335	315	322	321	338	338	332	376	388	370	402
1e	97	71	77	79	80	70	70	71	59	52	54	53
3e	91	58	74	77	77	58	57	61	49	53	51	54
5e	83	45	70	74	74	52	49	50	49	52	49	54
7e	81	63	66	71	72	61	59	58	62	58	55	62
9e	82	65	55	61	66	51	47	53	61	59	54	64
11e	80	63	47	51	57	52	50	55	71	65	61	69
13e	76	56	47	48	47	59	59	58	75	70	67	73
15e	65	45	39	40	41	50	52	44	75	65	62	68
17e	75	47	39	40	41	57	58	54	75	67	63	71
19e	80	46	42	43	44	47	47	45	61	59	56	63
21e	83	44	56	55	52	43	42	41	70	65	60	70
23e	85	56	59	59	61	51	52	48	67	65	60	71
25e	77	55	52	51	49	44	45	45	55	55	53	59
27e	74	64	40	42	50	45	46	45	53	56	55	59
29e	78	71	39	42	49	50	51	57	48	53	51	56
31e	92	74	56	63	66	66	67	68	48	68	66	70
33e	98	76	71	75	76	73	73	74	71	76	75	77
35e	101	77	76	79	79	75	75	76	76	78	77	78
37e	102	78	78	81	81	77	77	77	78	79	78	79
39e	102	78	78	81	81	77	77	77	78	79	78	79

Table E.1 Maldistribution data for evaporator coil (continued)

Test	80	82	83	84	85	86	87	88	89	90	91	100
Fan	M	H	M	H	L	M	H	M	H	L	L	L
RH	0.52	0.51	0.52	0.52	0.52	0.51	0.52	0.51	0.51	0.51	0.52	0.51
Tair in	106	105	80	75	75	75	80	96	96	105	106	96
w	524	534	365	359	328	347	388	470	487	502	509	472
1e	102	102	75	71	70	71	78	91	93	101	102	69
3e	97	99	65	68	62	65	76	85	90	97	99	65
5e	89	91	51	60	53	55	72	73	82	93	94	65
7e	85	81	54	53	54	54	63	69	71	88	90	70
9e	79	75	51	45	45	44	50	63	64	80	82	68
11e	85	79	56	46	53	48	51	68	66	85	87	77
13e	91	87	59	50	53	54	60	73	71	87	88	83
15e	92	90	51	46	41	44	54	68	69	79	80	80
17e	94	95	53	48	44	46	57	71	69	82	83	81
19e	88	90	58	50	43	46	55	69	71	78	80	73
21e	95	98	72	63	45	52	64	75	82	82	84	79
23e	92	97	74	66	49	54	62	77	84	81	82	81
25e	78	89	70	63	48	51	52	66	71	70	71	69
27e	76	79	66	55	43	46	51	66	68	70	72	68
29e	70	71	51	46	41	44	50	62	64	66	68	68
31e	77	82	57	60	52	56	68	79	83	71	73	82
33e	94	97	72	70	66	69	76	89	92	90	92	89
35e	98	101	75	73	70	72	79	92	94	95	97	91
37e	102	103	78	74	73	74	79	93	95	100	102	92
39e	104	103	78	73	73	74	79	94	95	102	103	93

Table E.1 Maldistribution data for evaporator coil (continued)

Tair in	80	67	67	74	73
w	371	272	273	292	289
1e	75	62	62	68	67
3e	66	58	59	63	62
5e	51	56	56	61	60
7e	52	60	61	67	66
9e	47	62	63	69	68
11e	49	62	62	68	67
13e	59	59	60	65	65
15e	51	52	54	54	56
17e	55	41	42	46	46
19e	55	34	34	39	38
21e	67	31	31	37	36
23e	66	37	35	47	44
25e	59	51	50	58	56
27e	51	55	53	64	62
29e	47	60	60	67	66
31e	57	62	63	70	69
33e	73	64	65	71	70
35e	77	65	66	72	71
37e	78	66	66	72	71
39e	79	66	66	72	71
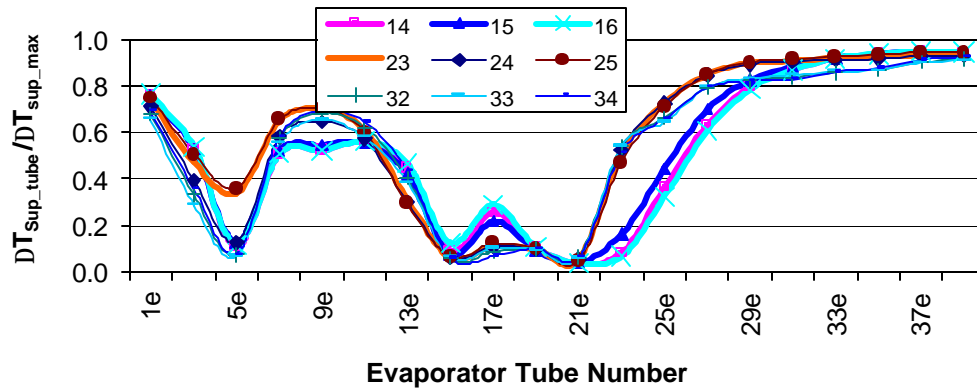
Figure E.1 Evaporator exit temperature profile: dry coil, low blower speed
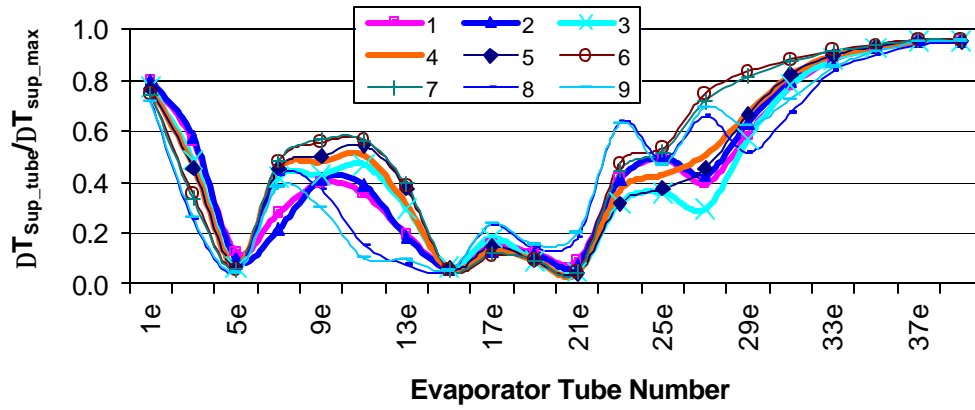
Figure E.2 Evaporator exit temperature profile: dry coil, medium blower speed
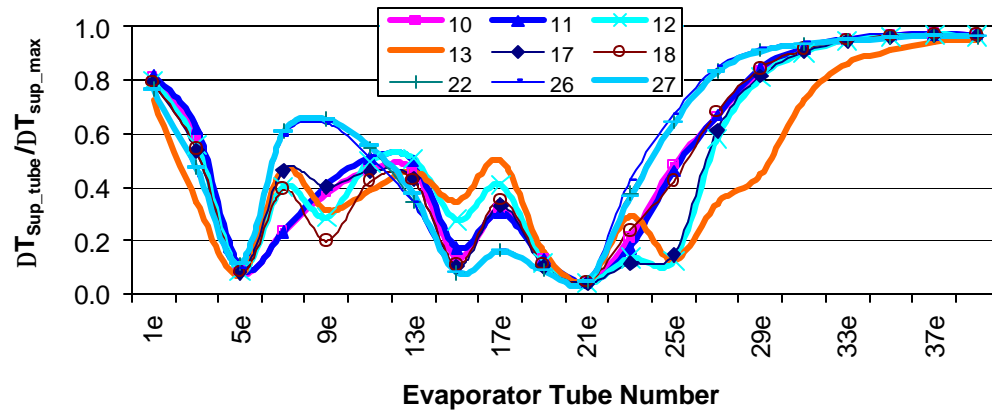
Figure E.3 Evaporator exit temperature profile: dry coil, medium blower speed
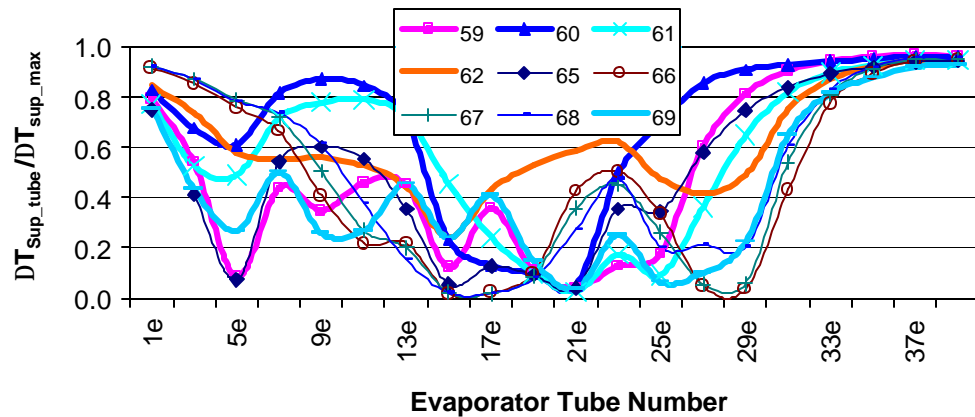
Figure E.4 Evaporator exit temperature profile: dry coil, medium blower speed
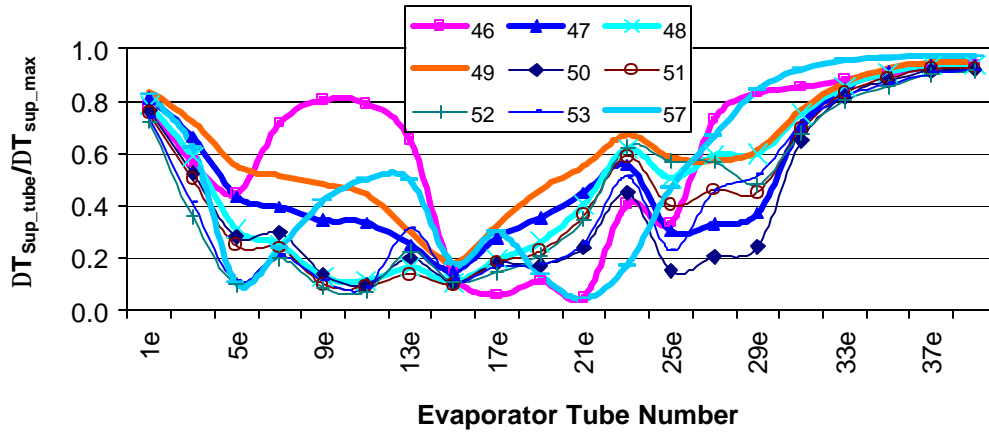
Figure E.5 Evaporator exit temperature profile: dry coil, medium blower speed
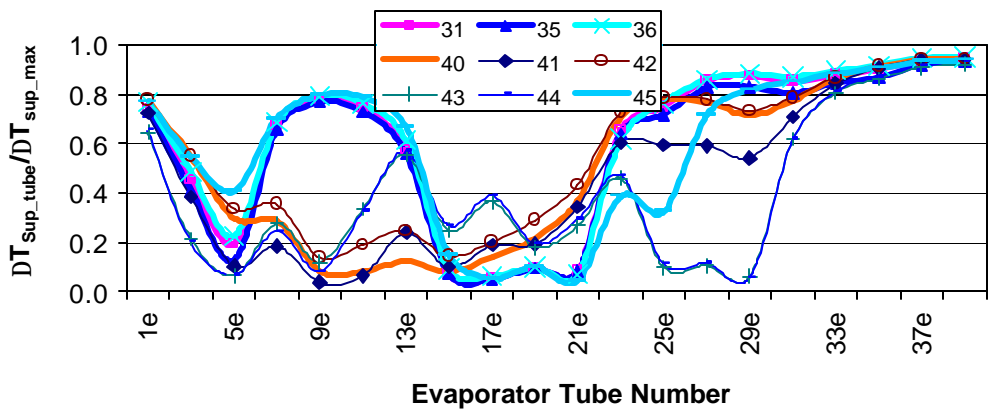
Figure E.6 Evaporator exit temperature profile: dry coil, medium blower speed
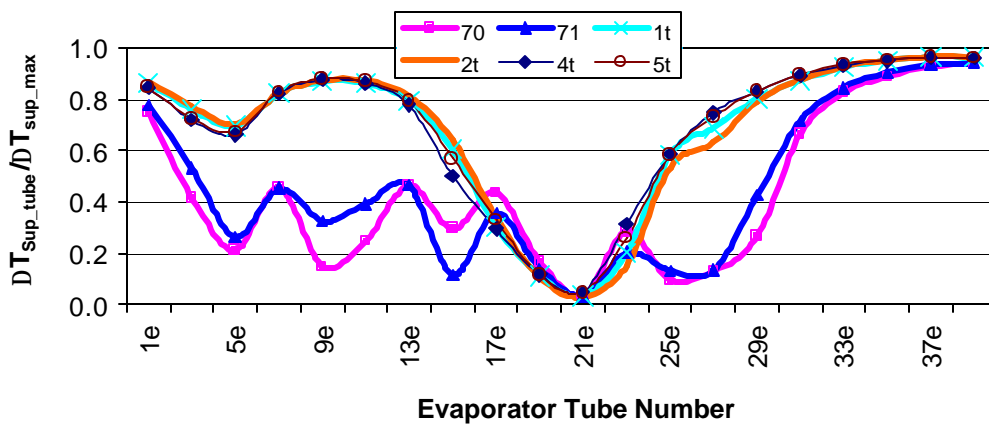
Figure E.7 Evaporator exit temperature profile: dry coil, medium blower speed
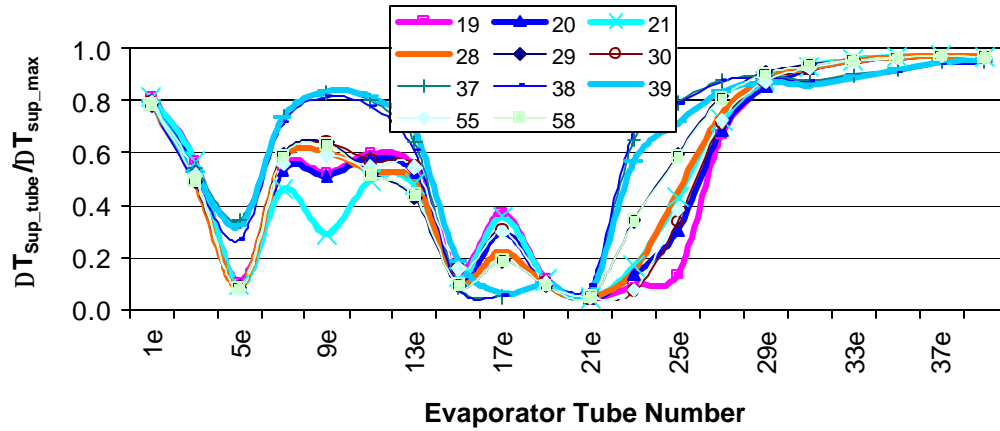
Figure E.8 Evaporator exit temperature profile: dry coil, high blower speed
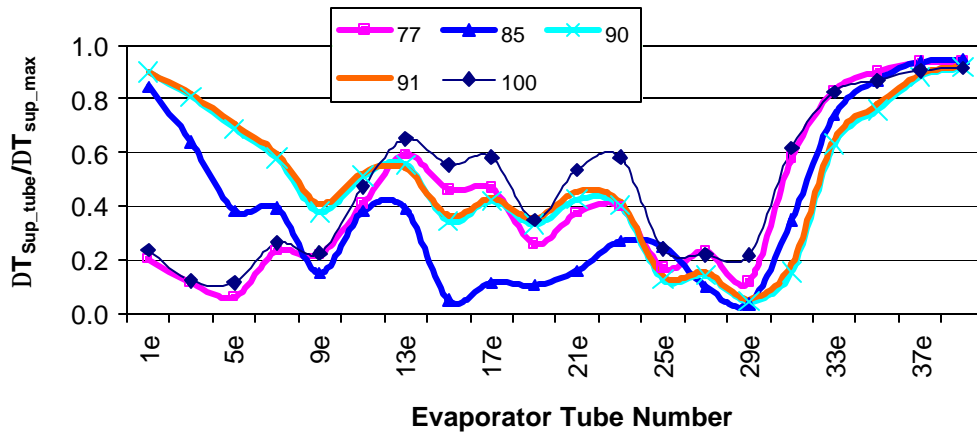
Figure E.9 Evaporator exit temperature profile: wet coil, low blower speed
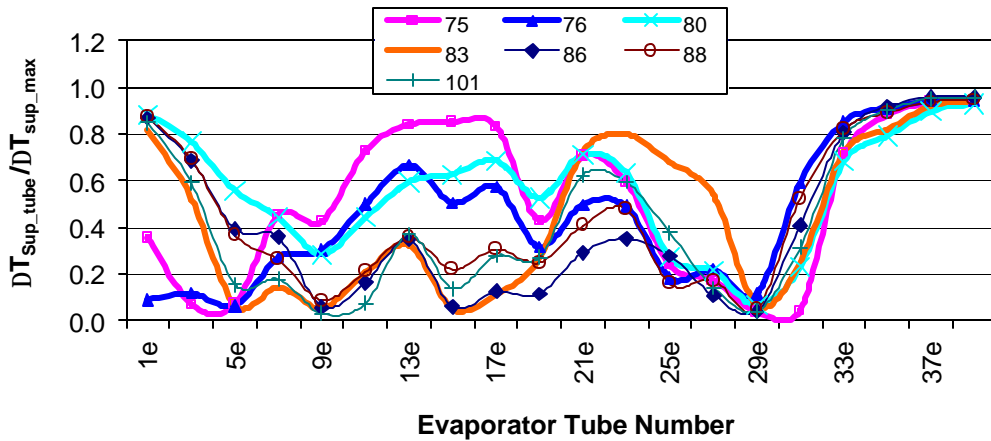
Figure E.10 Evaporator exit temperature profile: wet coil, medium blower speed
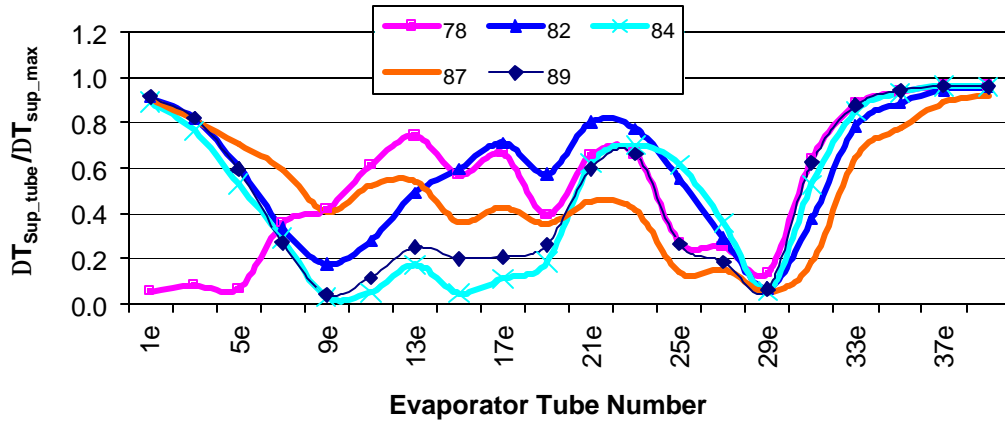
Figure E.11 Evaporator exit temperature profile: wet coil, high blower speed

Appendix F: Data Summary

F.1 Data summary for all test points

Table F.1 System performance summary

Test	1	2	3	4	5	6	7	8
Date	7/10/99	7/11/99	7/11/99	7/11/99	7/11/99	7/11/99	7/11/99	7/10/99
Tindoor [F]	70	70	70	70	70	70	70	69
Toutdoor [F]	66	68	76	82	82	96	96	111
RHair_E	0.251	0.247	0.267	0.275	0.273	0.289	0.290	0.333
Cond Fan [cfm]	2603	3704	2603	2603	3704	2603	3704	2603
Evap Fan [cfm]	796	796	796	796	796	796	796	796
EER [Btu/hr-W]	13.0	11.3	11.4	10.3	9.4	8.3	7.8	5.9
EER M [Btu/hr-W]	15.8	13.8	13.7	12.1	11.2	9.5	9.0	6.8
Qroom [Btu/hr]	21824	21881	21268	20757	20876	19759	19664	17248
Qroom M [Btu/hr]	25109	25050	24452	23817	23853	22648	22680	20797
Qcond [Btu/hr]	28681	28661	28813	28844	28596	28943	28539	28856
Qcond M	29065	28869	29127	29095	28777	29304	28897	29529
Mass flow [lbm/hr]	298	296	302	299	299	295	298	297
Mass flow M[lbm/hr]	299	299	302	304	303	308	309	309
Pevap [psia]	118.5	117.8	121.5	122.1	121.3	124.4	124.2	130.3
Pevap M [psia]	122.7	122.6	124.9	126.3	125.8	130.1	129.6	133.8
Tevap [F]	33.4	33.1	34.9	35.2	34.8	36.2	36.1	38.9
Tevap M [F]	35.3	35.3	36.4	37.0	36.8	38.7	38.5	40.4
Pcond [psia]	275.8	266.0	317.6	350.2	326.6	423.8	395.7	527.0
Pcond M [psia]	249.1	243.8	290.3	324.3	307.2	400.2	379.1	514.9
ΔPcond [psid]	11.1	10.7	11.3	11.1	11.2	11.1	11.3	9.0
ΔPcond M [psid]	0.2	0.2	0.2	0.2	0.2	0.2	0.2	0.2
Tcond [F]	86.6	84.0	96.6	103.8	98.7	118.3	113.0	135.6
Tcond M [F]	79.7	78.2	90.3	98.3	94.4	113.9	109.8	133.8
WRR [lbm/hr]	0.0	0.0	0.0	0.0	0.0	0.0	0.0	0.0
WRR M [lbm/hr]	0.0	0.0	0.0	0.0	0.0	0.0	0.0	0.0
RAC_power [W]	1523	1483	1714	1866	1759	2218	2082	2749
RAC_power M [W]	1417	1392	1614	1789	1699	2198	2082	2859
ΔTsubcool [F]	5.3	4.9	8.1	12.8	8.1	20.1	13.5	22.8
ΔTsubcool M [F]	11.7	9.5	13.8	15.3	11.8	18.2	14.1	23.2
ΔTsuperheat [F]	9.9	10.9	9.5	9.7	9.7	10.0	9.9	8.7
ΔTsuperheat M [F]	10	10	10	10	10	10	10	10

'M' = Model predictions from system simulation runs
EER for the system is calculated from experimental power measurements

Table F.1 System performance summary (continued)

Test	9	10	11	12	13	14	15	16
Date	7/10/99	6/29/99	6/30/99	6/30/99	6/29/99	7/1/99	7/1/99	7/1/99
Tindoor [F]	70	82	83	82	83	83	83	82
Toutdoor [F]	111	66	68	79	84	85	84	84
RHair_E	0.329	0.212	0.208	0.227	0.248	0.191	0.193	0.189
Cond Fan [cfm]	3704	2603	3704	2603	2603	2603	1799	3704
Evap Fan [cfm]	796	796	796	796	796	626	626	626
EER [Btu/hr-W]	5.6	14.6	12.7	12.3	11.6	10.6	10.2	9.8
EER M [Btu/hr-W]	6.7	18.0	15.7	15.0	13.8	12.7	12.5	11.9
Qroom [Btu/hr]	16937	24539	24712	23755	23735	21519	21341	21659
Qroom M [Btu/hr]	20944	28529	28625	27647	27250	25092	25055	25207
Qcond [Btu/hr]	28361	31198	31275	31216	31801	29360	29636	29125
Qcond M	29084	32594	32548	32710	32783	30685	31129	30344
Mass flow [lbm/hr]	301	329	327	336	345	306	306	307
Mass flow M[lbm/hr]	312	344	345	349	351	324	324	323
Pevap [psia]	130.1	130.4	129.6	134.7	138.6	125.8	126.9	125.0
Pevap M [psia]	133.8	139.6	139.7	142.6	144.1	134.2	134.8	133.4
Tevap [F]	38.8	39.0	38.6	40.9	42.5	36.9	37.4	36.5
Tevap M [F]	40.4	42.8	42.9	44.1	44.7	40.5	40.8	40.2
Pcond [psia]	493.1	277.9	268.9	334.2	359.5	360.9	395.7	333.4
Pcond M [psia]	485.3	250.2	244.5	306.5	332.1	338.9	362.4	316.4
ΔPcond [psid]	8.7	6.5	6.3	6.5	6.2	5.4	5.4	5.5
ΔPcond M [psid]	0.2	0.3	0.3	0.2	0.2	0.2	0.2	0.2
Tcond [F]	130.2	87.1	84.8	100.3	105.7	106.0	113.0	100.2
Tcond M [F]	129.0	80.0	78.4	94.2	100.0	101.5	106.5	96.5
WRR [lbm/hr]	0.0	0.0	0.0	0.0	0.0	0.0	0.0	0.0
WRR M [lbm/hr]	0.0	0.0	0.0	0.0	0.0	0.0	0.0	0.0
RAC_power [W]	2563	1525	1492	1782	1895	1880	2046	1748
RAC_power M [W]	2685	1415	1392	1679	1810	1816	1943	1699
ΔTsubcool [F]	16.1	4.3	4.3	7.5	9.6	13.3	19.0	8.4
ΔTsubcool M [F]	18.1	7.1	5.8	11.7	13.3	15.2	20.1	11.5
ΔTsuperheat [F]	8.8	13.0	14.0	11.2	10.6	11.7	11.3	12.2
ΔTsuperheat M [F]	10	10	10	10	10	10	10	10

'M' = Model predictions from system simulation runs
EER for the system is calculated from experimental power measurements

Table F.1 System performance summary (continued)

Test	17	18	19	20	21	22	23	24
Date	6/30/99	6/30/99	7/1/99	7/1/99	7/1/99	7/2/99	7/3/99	7/3/99
Tindoor [F]	83	83	82	83	83	83	83	83
Toutdoor [F]	85	84	84	85	84	98	98	98
RHair_E	0.237	0.229	0.256	0.262	0.250	0.243	0.202	0.206
Cond Fan [cfm]	1799	3704	2603	1799	3704	2603	2603	1799
Evap Fan [cfm]	796	796	888	888	888	796	626	626
EER [Btu/hr-W]	10.7	10.5	11.5	10.8	10.8	9.2	8.5	8.2
EER M [Btu/hr-W]	13.2	12.7	13.9	13.4	13.1	10.8	9.9	9.4
Qroom [Btu/hr]	23050	23458	24042	23882	24367	22248	20423	20441
Qroom M [Btu/hr]	27030	27378	28106	27978	28443	26034	23918	23783
Qcond [Btu/hr]	31615	31153	32323	32644	32185	31553	29620	30235
Qcond M	33175	32541	33665	34155	33597	33006	30976	31553
Mass flow [lbm/hr]	337	337	349	350	351	334	303	303
Mass flow M[lbm/hr]	351	351	363	365	365	357	330	328
Pevap [psia]	137.7	135.3	140.4	142.7	140.2	138.8	128.9	130.2
Pevap M [psia]	145.0	143.6	148.6	150.2	148.8	148.4	138.5	139.0
Tevap [F]	42.2	41.1	43.3	44.3	43.2	42.6	38.3	38.9
Tevap M [F]	45.1	44.6	46.6	47.2	46.7	46.5	42.4	42.6
Pcond [psia]	402.7	335.9	363.1	407.4	336.3	433.0	436.8	477.8
Pcond M [psia]	362.3	314.7	332.4	362.5	313.0	409.4	418.8	454.2
ΔPcond [psid]	6.5	6.7	7.1	6.9	7.3	7.7	7.2	7.5
ΔPcond M [psid]	0.2	0.2	0.2	0.2	0.3	0.2	0.2	0.2
Tcond [F]	114.3	100.7	106.5	115.2	100.8	119.9	120.6	127.7
Tcond M [F]	106.4	96.1	100.1	106.5	95.7	115.7	117.4	123.8
WRR [lbm/hr]	0.0	0.0	0.0	0.0	0.0	0.0	0.0	0.0
WRR M [lbm/hr]	0.0	0.0	0.0	0.0	0.0	0.0	0.0	0.0
RAC_power [W]	2107	1786	1944	2156	1815	2256	2245	2450
RAC_power M [W]	1971	1721	1839	1999	1741	2229	2255	2459
ΔTsubcool [F]	16.9	6.0	10.5	16.8	5.5	18.1	20.3	27.7
ΔTsubcool M [F]	18.1	10.2	12.4	16.8	9.2	17.2	18.8	25.2
ΔTsuperheat [F]	10.2	11.3	11.3	10.8	11.3	11.1	12.6	12.1
ΔTsuperheat M [F]	10	10	10	10	10	10	10	10

'M' = Model predictions from system simulation runs
EER for the system is calculated from experimental power measurements

Table F.1 System performance summary (continued)

Test	25	26	27	28	29	30	31	32
Date	7/2/00	7/2/99	7/2/99	7/2/99	7/2/99	7/2/99	7/4/99	7/3/99
Tindoor [F]	83	83	83	83	83	83	83	83
Toutdoor [F]	98	98	97	98	98	98	113	113
RHair_E	0.199	0.251	0.240	0.277	0.282	0.274	0.278	0.233
Cond Fan [cfm]	3704	1799	3704	2603	1799	3704	2603	2603
Evap Fan [cfm]	626	796	796	888	888	888	796	626
EER [Btu/hr-W]	8.1	8.6	8.8	9.3	8.7	8.9	7.0	6.6
EER M [Btu/hr-W]	9.6	10.1	10.5	10.9	10.3	10.5	7.5	7.1
Qroom [Btu/hr]	20492	21867	22457	23117	22596	23111	20675	19247
Qroom M [Btu/hr]	24110	25781	26192	26840	26591	26981	24129	22349
Qcond [Btu/hr]	29153	31877	31279	32574	32766	32173	31698	30029
Qcond M	30589	33610	32571	33895	34440	33472	33678	31694
Mass flow [lbm/hr]	304	332	335	350	347	351	335	313
Mass flow M[lbm/hr]	331	356	357	370	368	369	362	335
Pevap [psia]	127.9	140.3	138.0	144.9	145.5	143.7	145.5	137.3
Pevap M [psia]	138.0	149.2	147.4	153.1	153.6	152.2	154.4	144.4
Tevap [F]	37.8	43.3	42.3	45.2	45.4	44.7	45.4	42.0
Tevap M [F]	42.2	46.8	46.1	48.4	48.6	48.0	48.9	44.9
Pcond [psia]	402.7	481.9	398.7	439.8	486.1	404.8	542.3	534.5
Pcond M [psia]	390.0	452.2	380.6	412.1	451.2	385.2	549.1	543.5
ΔPcond [psid]	7.3	6.9	8.4	7.6	7.6	7.7	11.2	9.1
ΔPcond M [psid]	0.2	0.2	0.2	0.2	0.2	0.2	0.2	0.2
Tcond [F]	114.3	128.4	113.6	121.1	129.1	114.7	137.9	136.7
Tcond M [F]	112.0	123.4	110.1	116.2	123.2	111.0	139.0	138.2
WRR [lbm/hr]	0.0	0.0	0.0	0.0	0.0	0.0	0.0	0.0
WRR M [lbm/hr]	0.0	0.0	0.0	0.0	0.0	0.0	0.0	0.0
RAC_power [W]	2077	2502	2088	2318	2548	2145	2812	2743
RAC_power M [W]	2093	2476	2068	2272	2498	2121	3048	2982
ΔTsubcool [F]	13.6	25.1	12.2	17.5	24.1	11.4	22.8	22.1
ΔTsubcool M [F]	14.2	24.0	12.8	16.6	23.1	12.5	25.8	25.5
ΔTsuperheat [F]	12.8	10.3	11.7	10.4	10.1	10.9	12.4	12.1
ΔTsuperheat M [F]	10	10	10	10	10	10	10	10

'M' = Model predictions from system simulation runs
EER for the system is calculated from experimental power measurements

Table F.1 System performance summary (continued)

Test	33	34	35	36	37	38	39	40
Date	7/3/99	7/3/99	7/4/99	7/3/99	7/4/99	7/4/99	7/4/99	7/9/99
Tindoor [F]	82	83	83	83	83	82	83	95
Toutdoor [F]	112	113	113	112	112	113	112	78
RHair_E	0.238	0.230	0.290	0.271	0.297	0.307	0.297	0.203
Cond Fan [cfm]	1799	3704	1799	3704	2603	1799	3704	2603
Evap Fan [cfm]	626	626	796	796	888	888	888	796
EER [Btu/hr-W]	6.2	6.4	6.4	6.8	7.2	6.5	7.0	14.1
EER M [Btu/hr-W]	6.5	7.1	6.2	7.8	7.8	6.4	8.0	17.2
Qroom [Btu/hr]	19242	19297	20553	20716	21381	20847	21522	27562
Qroom M [Btu/hr]	22103	22525	23619	24473	25082	24400	25331	31122
Qcond [Btu/hr]	30558	29626	32447	31121	32376	32968	32078	35402
Qcond M	32594	31138	35134	32950	34437	35877	33701	36170
Mass flow [lbm/hr]	307	316	334	337	345	341	351	386
Mass flow M[lbm/hr]	332	338	358	364	374	368	376	400
Pevap [psia]	138.3	136.9	148.3	144.3	148.7	150.6	148.7	153.6
Pevap M [psia]	144.9	144.2	156.1	153.5	158.5	159.9	157.5	161.5
Tevap [F]	42.4	41.8	46.6	44.9	46.8	47.5	46.8	48.7
Tevap M [F]	45.1	44.8	49.6	48.6	50.5	51.0	50.1	51.6
Pcond [psia]	585.2	501.5	601.1	498.5	538.7	600.6	498.1	340.6
Pcond M [psia]	603.3	506.6	654.5	493.5	535.4	649.4	485.1	302.5
∆Pcond [psid]	8.5	9.5	11.2	10.9	11.6	11.3	12.2	11.9
∆Pcond M [psid]	0.2	0.2	0.2	0.2	0.2	0.2	0.2	0.3
Tcond [F]	144.2	131.6	146.5	131.1	137.4	146.4	131.0	101.7
Tcond M [F]	146.8	132.5	153.7	130.3	136.9	153.1	129.0	93.2
WRR [lbm/hr]	0.0	0.0	0.0	0.0	0.0	0.0	0.0	0.0
WRR M [lbm/hr]	0.0	0.0	0.0	0.0	0.0	0.0	0.0	0.0
RAC_power [W]	3033	2562	3151	2577	2819	3175	2602	1793
RAC_power M [W]	3341	2761	3692	2714	2994	3692	2692	1644
∆Tsubcool [F]	30.8	15.6	31.0	15.4	22.7	31.2	15.4	6.9
∆Tsubcool M [F]	34.7	19.6	39.7	18.1	24.2	39.2	16.9	5.5
∆Tsuperheat [F]	11.5	12.4	11.7	12.8	12.4	11.8	12.5	14.7
∆Tsuperheat M [F]	10	10	10	10	10	10	10	10

'M' = Model predictions from system simulation runs
EER for the system is calculated from experimental power measurements

Table F.1 System performance summary (continued)

Test	41	42	43	44	45	46	47	48
Date	7/9/99	7/8/99	7/8/99	7/8/99	7/4/99	7/4/99	7/10/99	7/9/99
Tindoor [F]	95	95	95	95	97	98	105	105
Toutdoor [F]	83	82	95	95	113	113	78	82
RHair_E	0.214	0.203	0.233	0.229	0.230	0.226	0.179	0.186
Cond Fan [cfm]	2603	3704	2603	3704	2603	3704	2603	2603
Evap Fan [cfm]	796	796	796	796	796	796	796	796
EER [Btu/hr-W]	13.3	12.2	11.0	10.6	8.3	8.2	15.6	14.8
EER M [Btu/hr-W]	16.1	14.9	13.1	12.5	9.5	9.6	18.6	17.7
Qroom [Btu/hr]	27406	27284	26382	26536	24612	25111	30641	30501
Qroom M [Btu/hr]	30776	30974	29816	29985	28383	28953	33527	33206
Qcond [Btu/hr]	35703	35091	36033	35717	35700	35596	38515	38642
Qcond M	36217	36015	36521	36147	37542	37338	38645	38623
Mass flow [lbm/hr]	397	376	403	403	391	400	412	423
Mass flow M[lbm/hr]	402	400	408	406	425	432	447	451
Pevap [psia]	157.1	152.7	162.0	160.6	165.6	167.0	166.3	169.1
Pevap M [psia]	162.5	161.5	166.7	165.3	176.6	178.0	178.9	181.0
Tevap [F]	50.1	48.4	52.0	51.4	53.3	53.8	53.6	54.6
Tevap M [F]	52.0	51.6	53.6	53.1	57.2	57.7	58.0	58.8
Pcond [psia]	365.8	337.8	436.2	399.8	550.5	511.0	348.3	366.4
Pcond M [psia]	323.8	304.9	390.2	364.9	514.7	477.9	305.6	321.7
ΔPcond [psid]	12.5	11.2	11.7	11.9	13.7	14.9	14.5	14.2
ΔPcond M [psid]	0.3	0.3	0.3	0.3	0.2	0.3	0.3	0.3
Tcond [F]	107.0	101.1	120.5	113.7	139.1	133.1	103.3	107.1
Tcond M [F]	98.2	93.8	112.0	107.0	133.7	127.8	94.0	97.7
WRR [lbm/hr]	0.0	0.0	0.0	0.0	0.0	0.0	0.0	0.0
WRR M [lbm/hr]	0.0	0.0	0.0	0.0	0.0	0.0	0.0	0.0
RAC_power [W]	1903	1781	2240	2062	2823	2612	1812	1898
RAC_power M [W]	1749	1656	2097	1961	2808	2582	1637	1714
ΔTsubcool [F]	8.0	6.0	15.1	9.1	23.2	15.7	8.8	8.8
ΔTsubcool M [F]	7.6	5.2	12.6	9.3	19.1	13.5	0.0	0.0
ΔTsuperheat [F]	11.5	20.7	9.3	9.9	12.8	13.5	22.8	18.4
ΔTsuperheat M [F]	10	10	10	10	10	10	10	10

'M' = Model predictions from system simulation runs
EER for the system is calculated from experimental power measurements

Table F.1 System performance summary (continued)

Test	49	50	51	52	53	55	56	57
Date	7/10/99	7/10/99	7/10/99	7/10/99	7/10/99	7/2/99	6/30/99	6/30/99
Tindoor [F]	105	105	105	105	105	83	83	82
Toutdoor [F]	82	95	95	111	110	100	83	67
RHair_E	0.173	0.206	0.200	0.224	0.221	0.277	0.187	0.209
Cond Fan [cfm]	3704	2603	3704	2603	3704	3704	3704	3704
Evap Fan [cfm]	796	796	796	796	796	888	626	796
EER [Btu/hr-W]	13.4	12.3	11.6	9.5	9.4	8.6	10.1	12.8
EER M [Btu/hr-W]	16.3	14.5	13.7	11.0	10.9	10.2	12.3	15.8
Qroom [Btu/hr]	30136	29556	29521	27809	28036	22951	21742	24700
Qroom M [Btu/hr]	33569	32455	32695	29541	30161	26782	25389	28498
Qcond [Btu/hr]	37952	39158	38683	39120	38769	32241	29045	31157
Qcond M	38626	39188	38949	37911	37894	33511	30359	32379
Mass flow [lbm/hr]	398	448	440	448	451	352	306	325
Mass flow M[lbm/hr]	447	454	453	479	473	370	323	343
Pevap [psia]	163.8	177.4	174.8	183.9	182.4	144.6	124.5	128.8
Pevap M [psia]	179.0	183.7	182.7	194.8	192.0	153.1	133.0	138.8
Tevap [F]	52.7	57.6	56.7	59.9	59.4	45.1	36.3	38.2
Tevap M [F]	58.1	59.7	59.4	63.5	62.5	48.4	40.0	42.5
Pcond [psia]	342.4	442.3	408.8	542.8	496.9	417.2	324.5	266.3
Pcond M [psia]	304.9	390.4	368.8	468.8	441.5	397.8	307.2	242.2
ΔPcond [psid]	13.8	17.2	16.9	18.0	18.4	7.7	5.5	6.3
ΔPcond M [psid]	0.3	0.3	0.3	0.3	0.3	0.2	0.2	0.3
Tcond [F]	102.1	121.5	115.4	138.0	130.8	117.0	98.2	84.1
Tcond M [F]	93.8	112.0	107.7	126.2	121.5	113.5	94.3	77.8
WRR [lbm/hr]	0.0	0.0	0.0	0.0	0.0	0.0	0.0	0.0
WRR M [lbm/hr]	0.0	0.0	0.0	0.0	0.0	0.0	0.0	0.0
RAC_power [W]	1791	2248	2087	2762	2519	2205	1705	1478
RAC_power M [W]	1635	2071	1951	2499	2344	2191	1652	1382
ΔTsubcool [F]	7.8	13.4	9.0	20.5	14.0	12.4	7.3	4.4
ΔTsubcool M [F]	0.0	7.8	5.1	0.0	0.0	12.9	11.2	5.8
ΔTsuperheat [F]	29.0	10.1	12.3	10.4	10.3	10.7	12.2	14.2
ΔTsuperheat M [F]	10	10	10	10	10	10	10	10

'M' = Model predictions from system simulation runs
EER for the system is calculated from experimental power measurements

Table F.1 System performance summary (continued)

Test	58	59	60	61	62	65	66	67
Date	7/2/99	6/30/99	7/6/99	7/7/99	7/9/99	7/12/99	7/13/99	7/13/99
Tindoor [F]	83	83	72	80	105	80	81	83
Toutdoor [F]	99	85	100	82	79	95	82	85
RHair_E	0.283	0.232	0.267	0.234	0.168	0.258	0.224	0.215
Cond Fan [cfm]	1799	2603	3704	2603	3704	2603	2603	2603
Evap Fan [cfm]	888	796	796	796	796	796	796	796
EER [Btu/hr-W]	8.6	11.2	7.1	11.8	14.1	9.5	10.2	10.2
EER M [Btu/hr-W]	10.1	13.6	8.6	13.9	17.0	10.9	13.9	13.6
Qroom [Btu/hr]	22542	23306	18970	23919	30502	22379	20743	21431
Qroom M [Btu/hr]	26601	27195	22911	26650	33939	25496	26924	27299
Qcond [Btu/hr]	32850	31426	28128	31026	38065	31703	29911	30476
Qcond M	34557	32815	29680	31917	38742	32186	32206	32862
Mass flow [lbm/hr]	348	338	291	329	393	335	315	322
Mass flow M[lbm/hr]	369	352	319	339	445	346	343	352
Pevap [psia]	146.3	136.5	124.0	133.2	162.0	138.5	127.9	130.9
Pevap M [psia]	154.3	144.5	134.3	139.2	177.6	143.8	140.7	144.6
Tevap [F]	45.8	41.6	36.0	40.2	52.0	42.5	37.8	39.2
Tevap M [F]	48.9	44.9	40.6	42.7	57.6	44.6	43.3	44.9
Pcond [psia]	491.4	365.0	421.4	350.8	326.1	424.7	349.3	365.6
Pcond M [psia]	456.7	336.8	408.1	318.7	290.8	395.9	319.1	333.7
ΔPcond [psid]	7.6	6.6	10.2	10.3	12.8	13.9	9.1	9.4
ΔPcond M [psid]	0.2	0.2	0.2	0.2	0.3	0.2	0.2	0.2
Tcond [F]	129.9	106.9	117.8	103.9	98.5	118.4	103.6	107.0
Tcond M [F]	124.2	101.0	115.4	97.0	90.4	113.1	97.1	100.3
WRR [lbm/hr]	0.0	0.0	0.1	0.0	0.0	0.0	0.1	0.0
WRR M [lbm/hr]	0.0	0.0	0.0	0.0	0.0	0.0	0.0	0.0
RAC_power [W]	2576	1927	2203	1875	1718	2208	1870	1939
RAC_power M [W]	2529	1835	2235	1743	1571	2159	1759	1827
ΔTsubcool [F]	24.4	11.1	14.1	11.0	8.4	17.4	11.3	12.7
ΔTsubcool M [F]	23.4	13.5	15.1	13.3	0.0	17.1	13.0	13.3
ΔTsuperheat [F]	9.8	10.8	13.0	11.8	30.7	10.1	9.6	9.8
ΔTsuperheat M [F]	10	10	10	10	10	10	10	10

'M' = Model predictions from system simulation runs
EER for the system is calculated from experimental power measurements

Table F.1 System performance summary (continued)

Test	68	69	70	71	1F*	2F	4F	5F
Date	7/13/99	7/16/99	7/16/99	7/16/99	7/4/99	7/5/99	7/5/99	7/5/99
Tindoor [F]	83	80	80	80	67	67	74	73
Toutdoor [F]	97	82	82	74	67	69	86	84
RHair_E	0.225	0.254	0.250	0.233	0.234	0.231	0.237	0.236
Cond Fan [cfm]	2603	2603	3704	3704	2603	3704	2603	3704
Evap Fan [cfm]	796	796	796	796	796	796	796	796
EER [Btu/hr-W]	8.6	10.7	10.7	11.8	11.9	10.4	10.0	9.1
EER M [Btu/hr-W]	10.9	13.8	12.8	14.3	15.0	13.2	12.0	11.3
Qroom [Btu/hr]	20653	21658	23462	24218	20229	20437	20767	20443
Qroom M [Btu/hr]	26131	26622	26770	27450	24169	24251	24599	24476
Qcond [Btu/hr]	30564	31420	31260	31378	27000	27197	28777	28217
Qcond M	33016	31925	31697	31741	28190	28124	30225	29592
Mass flow [lbm/hr]	321	338	338	332	272	273	292	289
Mass flow M[lbm/hr]	357	339	339	336	289	291	318	314
Pevap [psia]	134.1	135.7	134.9	132.1	110.3	110.7	121.3	119.0
Pevap M [psia]	148.3	139.4	138.9	137.0	119.1	119.7	132.2	129.9
Tevap [F]	40.6	41.3	41.0	39.7	29.4	29.6	34.8	33.7
Tevap M [F]	46.5	42.7	42.6	41.7	33.6	33.9	39.6	38.6
Pcond [psia]	431.5	352.4	327.1	293.3	278.1	269.2	363.0	332.4
Pcond M [psia]	404.6	320.7	302.8	266.9	254.4	248.2	341.5	316.5
ΔPcond [psid]	9.5	11.6	11.7	11.3	7.7	8.2	9.1	9.3
ΔPcond M [psid]	0.2	0.2	0.2	0.2	0.2	0.2	0.2	0.2
Tcond [F]	119.7	104.2	98.8	90.9	87.2	84.9	106.5	100.0
Tcond M [F]	114.8	97.5	93.3	84.4	81.1	79.4	102.1	96.5
WRR [lbm/hr]	0.0	0.0	0.0	0.0	0.0	0.0	0.0	0.0
WRR M [lbm/hr]	0.0	0.0	0.0	0.0	0.0	0.0	0.0	0.0
RAC_power [W]	2250	1860	1742	1597	1542	1506	1927	1784
RAC_power M [W]	2208	1756	1664	1492	1438	1410	1870	1740
ΔTsubcool [F]	18.5	9.2	4.7	4.6	9.3	8.0	15.9	10.7
ΔTsubcool M [F]	16.9	13.4	10.3	8.5	12.5	10.0	15.6	11.8
ΔTsuperheat [F]	8.9	9.7	10.7	11.8	14.0	13.9	13.6	14.0
ΔTsuperheat M [F]	10	10	10	10	10	10	10	10

'M' = Model predictions from system simulation runs

EER for the system is calculated from experimental power measurements

*F = Slightly frosted coil

Table F.1 System performance summary (continued)

Test	75	76	77	78	80	82	83	84
Date	7/7/99	7/12/99	7/12/99	7/12/99	7/12/99	7/12/99	7/13/99	7/13/99
Tindoor [F]	80	80	80	80	106	105	80	75
Toutdoor [F]	82	95	95	95	96	96	115	83
RHair_E	0.515	0.515	0.515	0.515	0.515	0.514	0.516	0.517
Cond Fan [cfm]	2603	2603	2603	2603	2603	2603	2603	2603
Evap Fan [cfm]	641.4	571.3	425.4	717.8	448.2	694.6	699.7	871.9
EER [Btu/hr-W]	12.1	10.1	9.8	10.1	13.7	13.3	6.7	10.7
EER M [Btu/hr-W]	15.3	11.8	11.2	11.8	16.2	16.1	7.7	13.8
Qroom [Btu/hr]	25278	24298	23188	25135	33424	33815	20601	23043
Qroom M [Btu/hr]	29498	27487	25649	28715	36151	37943	25508	28778
Qcond [Btu/hr]	34204	34964	33864	35952	45612	46514	33434	32852
Qcond M	34869	34196	32345	35395	42923	44737	35342	34182
Mass flow [lbm/hr]	376	388	370	402	524	534	365	359
Mass flow M[lbm/hr]	380	373	348	390	538	570	386	370
Pevap [psia]	149.0	156.2	149.9	161.0	207.6	211.1	155.5	142.6
Pevap M [psia]	154.4	153.9	144.5	160.2	215.5	227.1	163.5	150.8
Tevap [F]	46.9	49.7	47.2	51.6	67.7	68.8	49.5	44.2
Tevap M [F]	49.0	48.7	44.9	51.2	70.1	73.6	52.4	47.5
Pcond [psia]	361.0	432.9	431.1	434.0	452.5	455.6	560.1	359.9
Pcond M [psia]	321.2	393.3	396.0	390.2	395.2	398.6	558.9	323.5
ΔPcond [psid]	14.0	17.7	16.2	19.2	22.1	22.4	12.2	12.1
ΔPcond M [psid]	0.3	0.2	0.2	0.2	0.4	0.4	0.2	0.2
Tcond [F]	106.0	119.9	119.6	120.1	123.3	123.8	140.6	105.8
Tcond M [F]	97.6	112.6	113.1	112.0	113.0	113.6	140.5	98.1
WRR [lbm/hr]	9.5	9.9	10.4	10.2	19.8	18.1	6.3	7.0
WRR M [lbm/hr]	9.8	9.4	9.8	8.5	18.9	16.5	7.0	6.8
RAC_power [W]	1926	2246	2198	2339	2281	2394	2919	2007
RAC_power M [W]	1759	2150	2131	2218	2058	2156	3123	1882
ΔTsubcool [F]	8.6	14.6	15.7	13.9	13.3	14.0	23.8	9.7
ΔTsubcool M [F]	10.1	15.5	17.1	14.2	0.0	0.0	25.4	11.3
ΔTsuperheat [F]	9.4	8.4	8.5	8.8	17.6	17.9	7.9	8.1
ΔTsuperheat M [F]	10	10	10	10	10	10	10	10

'M' = Model predictions from system simulation runs
EER for the system is calculated from experimental power measurements

Table F.1 System performance summary (continued)

Test	85	86	87	88	89	90	91	100	101
Date	7/14/99	7/14/99	7/14/99	7/14/99	7/14/99	7/14/99	7/14/99	7/12/99	7/13/99
Tindoor [F]	75	75	80	96	96	105	106	96	80
Toutdoor [F]	81	83	83	97	96	95	96	95	82
RHair_E	0.515	0.515	0.515	0.514	0.515	0.515	0.516	0.514	0.515
Cond Fan [cfm]	2603	2603	2603	2603	2603	2603	2603	2603	2603
Evap Fan [cfm]	474	639.4	951.2	795.1	502.4	364.7	481.3	625.8	745.8
EER [Btu/hr-W]	10.9	10.8	11.4	11.8	11.8	13.1	13.5	12.6	11.6
EER M [Btu/hr-W]	13.7	13.9	15.1	15.2	13.7	15.9	16.7	15.5	15.5
Qroom [Btu/hr]	21483	22429	24851	28957	30040	31175	32170	29905	23874
Qroom M [Btu/hr]	25797	27462	31215	34715	33227	34795	36457	33958	30174
Qcond [Btu/hr]	30659	31901	34961	40507	41681	43356	44046	40804	33563
Qcond M	30983	32849	36667	41590	40079	41552	43235	40659	35550
Mass flow [lbm/hr]	329	347	388	470	487	502	509	472	371
Mass flow M[lbm/hr]	327	352	408	501	469	500	544	481	390
Pevap [psia]	131.6	138.1	152.6	184.9	190.2	197.8	200.6	185.5	146.8
Pevap M [psia]	134.6	144.0	165.0	201.6	189.6	201.0	217.4	193.9	158.2
Tevap [F]	39.5	42.3	48.3	60.2	62.0	64.6	65.5	60.4	46.0
Tevap M [F]	40.7	44.7	53.0	65.7	61.8	65.5	70.7	63.2	50.4
Pcond [psia]	347.2	358.2	364.2	449.8	449.2	446.9	449.6	441.7	357.9
Pcond M [psia]	315.8	324.2	324.2	398.4	396.6	392.5	395.9	389.0	320.9
ΔPcond [psid]	10.6	11.5	14.9	21.1	22.3	23.8	24.1	23.7	12.0
ΔPcond M [psid]	0.2	0.2	0.3	0.3	0.3	0.3	0.4	0.3	0.3
Tcond [F]	103.1	105.5	106.7	122.8	122.7	122.3	122.8	121.4	105.4
Tcond M [F]	96.4	98.2	98.2	113.6	113.2	112.4	113.1	111.8	97.5
WRR [lbm/hr]	8.3	7.8	7.4	10.5	17.8	18.5	17.2	12.1	7.1
WRR M [lbm/hr]	8.9	8.3	7.8	12.6	14.8	19.1	18.8	14.2	9.2
RAC_power [W]	1815	1912	2023	2306	2392	2221	2235	2212	1901
RAC_power M [W]	1716	1799	1873	2113	2225	2028	2018	2025	1766
ΔTsubcool [F]	10.0	9.8	8.7	12.4	12.2	11.8	12.2	11.3	8.0
ΔTsubcool M [F]	14.0	12.9	7.1	2.9	6.9	2.6	0.0	4.6	8.9
ΔTsuperheat [F]	8.2	7.8	8.6	10.1	10.1	14.0	14.9	11.0	8.5
ΔTsuperheat M [F]	10	10	10	10	10	10	10	10	10

'M' = Model predictions from system simulation runs
EER for the system is calculated from experimental power measurements